OPTIMISATION OF FREE SPACE OPTICAL COMMUNICATION FOR SATELLITE AND TERRESTRIAL APPLICATIONS

By

INIABASI E. ITUEN

Submitted for the Degree of

Doctor of Philosophy

ENGINEERING AND DESIGN

SCHOOL OF ENGINEERING AND INFORMATICS

UNIVERSITY OF SUSSEX

BRIGHTON

UNITED KINGDOM

September, 2016

DECLARATION AND STATEMENT OF ORIGINALITY

DEPARTMENT OF ENGINEERING AND DESIGN

SCHOOL OF ENGINEERING AND INFORMATICS

UNIVERSITY OF SUSSEX

BRIGHTON

September, 2016

I hereby declare that this thesis has not been and will not be, submitted in whole or in part to another University for the award of any other degree.

It is the original work of Iniabasi Ituen with results from simulations performed here in the University of Sussex.

Signature: ……..

DEDICATION

To the Author of infinite knowledge and wisdom, my Source of illumination.

ABSTRACT

The future of global telecommunications looks even more promising with the advent of Free Space Optics (FSO) to complement Fibre Optics technology. With the main impairments to Free Space Optics known to be diffraction and atmospheric turbulence, it is critical to adequately characterise the atmospheric medium for effective FSO system design. Most laser sources can be designed to produce Gaussian-like beam profiles, which suffer from diffraction issues. To address this, a non-diffracting beam called the Bessel beam is introduced; its central core has been proven to be resistant to diffractive spreading whilst propagating. However, both Gaussian and Bessel beams will experience distortion when propagating through atmospheric turbulence. The strength of atmospheric turbulence C_n^2 is considered constant for ground-to-ground (terrestrial) applications, but proven variable and gradually-weakening for ground-to-space (satellite) applications. In this research, we investigate the propagation of the two beams both in the ground-to-ground scenario and in the ground-to-space scenario. For the ground-to-space scenario, we define a maximum height of 22 km above which the effect of atmospheric turbulence is considered negligible. We also investigate the propagation of the beams from the ground, beyond the 22 km limit, into deep space. We analyse and compare the performance of the beams for all the scenarios based on predefined performance measures. The Bessel beam offers enhanced performance and is shown to outperform the Gaussian on a number of the performance measures.

ACKNOWLEDGEMENT

I deeply appreciate my lovely wife, Sussan for standing by me and with me through it all. You are and will always be an inspiration. We are blessed to have our son, Lucas during this study period. To you dear Lucas, thanks for affording me the privilege of fatherhood and the joys of nappy changing.

I am grateful to my Dad and Mum for bringing me up and for the love, support and guidance. I have been blessed to have other father-figures whom I have learnt a lot from: Biodun Fatoyinbo and Alan Preston; thanks for the nurturing and counsels.

I will not forget to express my gratitude to my supervisors Professor Chris Chatwin, Dr. Phil Birch and Dr. Rupert Young. I think I had the best set of supervisors ever. Thank you all for being immensely supportive and understanding. I would like to appreciate all other members of the Department of Engineering for your support.

I appreciate my sponsor, the Niger Delta Development Commission (NDDC) Nigeria, for covering my tuition fee cost. I thank my employer, the National Space Research and Development Agency (NASRDA) Nigeria, for your support, especially my Director, Dr. Olufemi Agboola and Mr. Ogubo, who have been really supportive.

To my colleagues: Babatunde Olawale, Alaa Hussein, Mohammed Al-Darkazali, Sola Ajiboye, Tabassum Qureshi and Auday Al-Mayyahi. You all have inspired me a lot. It has been fun working with you.

TABLE OF CONTENTS

LIST OF FIGURES

LIST OF TABLES

LIST OF ACRONYMS

FSO	Free Space Optics
RMS	Root Mean Square
DFT	Digital Fourier Transform
FFT	Fast Fourier Transform
FT	Fourier Transform
TF	Transfer Function
IR	Impulse Response
HAP	Hufnagel-Andrews-Philips
HOE	Holographic Optical Element
SLM	Spatial Light Modulator
CGH	Computer-generated Hologram
FWHM	Full Width Half Maximum
LEO	Low Earth Orbit
ISS	International Space Station
GPS	Global Position System
GSO	Geostationary Orbit
BER	Bit Error Rate
SNR	Signal to Noise Ratio
UV	Ultra-Violet
PSD	Power Spectral Density
BPP	Beam Parameter Product

LIST OF PRINCIPAL SYMBOLS

λ = wavelength.

k =wavenumber.

ω_0= Gaussian beam waist radius.

$\psi(z)$= the *Gouy phase shift* at point *z*.

$R(z)$= radius of the wavefront of the beam at point *z*.

η = the characteristic impedance of the medium of propagation.

θ = Angle of divergence of Gaussian Beam from waist or cone angle of Bessel beam.

ϕ = Bessel beam azimuth.

J_n = nth order Bessel function of the first kind.

ϵ = Electric permittivity.

μ = Magnetic permeability.

ϵ_0 = Permittivity of free space or electric constant.

μ_0 = Permeability of free space or magnetic constant.

χ_e = Electric susceptibility.

χ_m = Magnetic susceptibility.

ρ = Electric charge density.

$\nabla \times$ = Curl of a vector

∇^2 = Laplacian.

$\Im$ = Fourier Transform.

$\Im^{-1}$ = Inverse Fourier Transform.

H = Transfer function.

h = Impulse response.

D_{ij} = Structure tensor.

N = Refractive index.

L_0 = Outer scale.

l_0 = Inner scale.

C_n^2 = Refractive index structure constant.

r_0 = Coherence parameter.

Φ_n = Refractive index Power spectral density.

Φ_ϕ = Phase Power spectral density.

χ = log-amplitude perturbation.

σ_χ^2 = Scintillation index.

D_ϕ = Phase structure function.

LIST OF RELATED PUBLISHED PAPERS

- Iniabasi Ituen, Philip Birch, Chris Chatwin, and Rupert Young, "Propagation of Bessel Beam for Ground-to-Space Applications," *Propagation through and Characterization of Distributed Volume Turbulence and Atmospheric Phenomena*, Arlington, Virginia United States, June 2015, paper PM3C.4.**doi**: http://dx.doi.org/10.1364/PCDVTAP.2015.PM3C.4
- Philip Birch, Iniabasi Ituen, Rupert Young, Chris Chatwin, "Long-distance Bessel beam propagation through Kolmogorov turbulence," *J. Opt. Soc. Am. A.* vol. **32**, Issue 11 (2015), pp. 2066-2073. **doi**: http://dx.doi.org/10.1364/JOSAA.32.002066.

CHAPTER 1

1.0 INTRODUCTION

1.1 Background

It is believed that the use of light as a vehicle for information transportation has been used for millennia with the first written evidence by Aeschylus in a play, *Agamemnon,* referring to the era of Trojan War in 1200 BCE. Since then, it has gradually gained relevance in many fields of technology. The advent of Free Space Optical (FSO) Communication has introduced a huge potential to the future of the global telecommunication industry. FSO is a line-of-sight communication technology that communicates optical signals in free space. FSO can be deployed for terrestrial applications (ground-to-ground applications) or satellite applications (ground-to-space applications, and vice versa). There is a wide range of applications for FSO: Security and military applications, telecommunications and computer networking, satellite applications, observatory astronomy, to mention but a few.

In FSO, optical signal carriers are modulated with the message signal instead of radio wave carriers as used in the traditional Radio Frequency (RF) communication. Compared to RF communication, the prospect of providing huge data rates, broad and unlimited bandwidth, transmitted data security, immunity to RF interference, requiring no license for operation, to mention but a few, makes FSO highly promising. It is mostly an outdoor technology that promises data rates higher than 1Gb/s per link, and if Wavelength Division Multiplexing (WDM) is incorporated, the aggregate bandwidth per link may exceed 10Gb/s and potentially 50 or 120Gb/s per link" [1]. In addition, optical components are cheaper and consume less electrical power compared to high-speed Radio components [2].

The major difference between FSO and fibre optic technology is the fact that no optic fibre cables are used as the channel, hence it is quicker and easier to deploy as well as requiring minimal need for maintenance compared with fibre optics [2]. For terrestrial applications, fibre optics technology has established itself after meeting all the expectations earlier predicted, and it is not expected to be replaced by another technology for many years to come. However, FSO will be complementary for scenarios where there is no existing fibre infrastructure, or for topographies and scenarios where it is impossible to run the fibres [1].

However, the FSO channel is known to have the major disadvantage of its high sensitivity to adverse phenomena. The main adverse phenomena that affects FSO are *diffraction, scattering/absorption by aerosols* and *atmospheric turbulence*. When deployed for terrestrial applications, tropospheric conditions (like fog, rain, snow, cloud cover, and so on) impair the communication. For Optical satellite communications, the ionospheric losses are also taken into consideration for an earth-to-space optical link, as well as the extreme space radiations especially for Inter-Satellite links.

1.2 Research Motivation and Objectives

The Longley-Rice model has been officially adopted as the standard prediction model for the transmission loss of tropospheric radio signals. This model is essential to the radio engineer as it helps to formalize the propagation of radio waves along a link, predicting the path loss as well as the coverage area. It aids in planning the optimal location of the antenna, antenna height, power of the transmitter, possible interference on the coverage area, and so on, for a particular location [3]. Such an efficient model is

yet to be adopted for the optical regime as it is still under intense research, although several location-specific prediction models as well as empirical models have been devised [4, 5, 6, 7, 8] one of which is the popular Kolmogorov's turbulence model. This research aims to utilise global research to characterise the behaviour of optical beams as they propagate through free space. The Longley-Rice model only makes predictions for terrestrial communication through the troposphere, making it not ideal for satellite links [4]. Therefore an optical signal propagation model is needed not only for tropospheric communications but also accounting for the ionosphere and possibly deep space.

An engineer designing a system for FSO propagation will be concerned with not only errors introduced by the transmitting and receiving electronics, but also the errors introduced into the system by the propagation medium. As optical beams propagate through the atmosphere, they are distorted by the fluctuations in refractive index due to turbulent flow. Astronomers have found this distortion errors frustrating for decades now. To overcome the distortion, an accurate physical model of the atmospheric turbulence is required to sample the effect of the turbulence in Free Space Optical wave propagation. This work aims to provide progress towards addressing this urgent need.

1.3 Methodology

The research question or research objective is to characterise, through modelling, the performance of Gaussian and Bessel beams propagating through atmospheric turbulence. The effect of scattering, which is also present in the atmosphere, was ignored in this case and this forms part of the researcher's proposed future work. Figure 1 summarises the research approach.

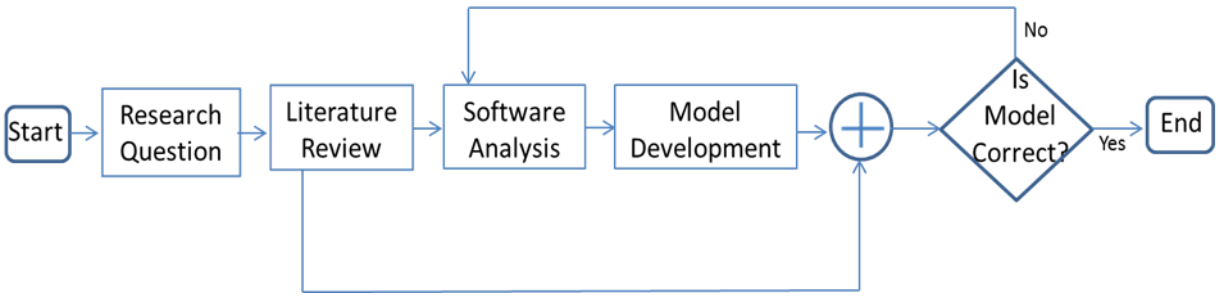

Fig.1: Research Approach

Literature Review

A detailed review of past works done in this area was completed, going over some basic concepts on wave propagation through the atmosphere, channel impairments, and previous optical beam propagation models. These added to the library of facts needed to develop a robust model. Before commencing the simulation, some system models needed to be developed mathematically based on some of the reviewed existing theory.

Software Analysis

The MATLAB has proven to be an invaluable tool for such simulations as this, other software options are Mathematica, Labview, and Light-pipes. The desired software should be able to model up to six different atmospheric conditions and the corresponding effect on the received signal. MATLAB was eventually the chosen software as it is easier to adapt to suit the research.

Model Development

Engineering modelling is becoming more popular due to the high cost of implementing experiments. This stage entails implementing on software, the system models earlier developed from the literature. The two different beams where modelled first, then the beam propagation was modelled, also including the effect of atmospheric turbulence.

The robustness of MATLAB also aided an effective presentation of the results based on different performance measures.

Comparative Evaluation:

The developed model was evaluated with the earlier defined system models, established hypotheses and compared with other available results obtained from the literature. This was necessary to ensure the model is performing as expected. If not, the whole process is repeated from the Software Analysis as seen from the Fig. 1.

1.4 Related Past Researches

In the last century, the effect of turbulence in Optical communication has received a lot of attention from optical physicists and optical communications engineers. Quite a lot of work has been done to characterise the propagation of Gaussian beams, which is the common beam profile from most lasers. However due to diffraction, the Gaussian beam suffers from beam spreading resulting in severe loss of its initial energy and poor signal to noise ratio at the receiver. To address this, Durnin [9] proposed a cylindrically-symmetric non-diffracting beam called the Bessel beam, with a central core surrounded by a set of same-energy-level concentric rings. Some authors have shown that the central core of a Bessel beam is resistant to diffractive spreading compared to that of a Gaussian beam with similar beam radius [10,11].

The Bessel beam can be decomposed into an infinite set of plane wavefronts at different azimuths, but at a fixed inclination towards the direction of travel. When propagating, the wavefronts travel inwardly adding up to the energy of the central core [9,12,13]. This

inward diffraction is what helps its on –axis intensity to remain constant as it propagates. Another effect of the inward diffraction is an attribute called *self- healing*: the beam is capable of recovering back its profile down the path after being scattered by an obstruction. These properties make Bessel beams very promising for various applications like the FSO Communications as well as observatory astronomy.

This research will investigate the possible improvement to FSO by modelling the propagation of this Bessel beam through free space, and comparing it with the Gaussian beam. The additional effect of atmospheric turbulence on the propagating beam will also be considered. Modelling the turbulence in the atmospheric channel is a very critical consideration in designing an FSO system. Nelson *et al* [12] investigated the propagation of these two beams (Gaussian and Bessel beams) over a short ground-to-ground range of 6.4km, with a fixed strength of turbulence C_n^2. In this research, we will not only look at the ground-to-ground scenario, but will also investigate the more difficult beams propagation from ground to space. The ground-to-space model we propose in this work is a modification to the Hufnagel-Andrews-Philips model [14], considering C_n^2 to be larger in the lower atmosphere but gradually weakening with altitude. From our ground-to-space model, we define a maximum altitude of 22 km above which the effect of atmospheric turbulence is considered negligible. Beyond this altitude and up to 100 km height, the beams propagate *in vacuo.*

1.5 Research Achievements

We have been able to bring some contributions to the vast research going on globally with the aim of better characterising the medium for Free-Space Optical

communications. As mentioned earlier, we proposed our model for C_n^2 with respect to altitude, leading to a definition of a maximum height of 22 km above which turbulence effect will be negligible.

We have defined some ground-to-space propagation target altitudes and the minimum beam radius (for both Gaussian and Bessel beams) required to ensure not more than a half of the initial beam energy is lost. These definitions are based on the known fact that the longer the distance of the FSO communication, the bigger the required size of the aperture of the transmitter and receiver to minimise power losses.

We modelled the propagation of the two beams and observed their performances with and without the presence of atmospheric turbulence. Not only did we model the ground-to-ground and ground-to-space turbulence scenarios, we also modelled the deep space scenario were the beams are propagated beyond the 22 km turbulence limit. We compared the performance of the two beams based on some performance measures: Beam wander, normalised captured power and RMS intensity error of the propagated beam compared to the unaberrated beam.

1.6 Dissertation Outline

The rest of this dissertation will first discuss theoretical concepts that are central to the work, before going ahead to discuss the simulations and results. Chapter 2 will give an overview of the two kinds of beams that will be considered in this research: the Gaussian beam and the Bessel beam. A detailed review is carried out for both beams

including the Beam profiles and Intensity distributions, energy contained in the beams as well as a summarised comparison of the beams with each other.

The theory behind the propagation of the beams through atmospheric turbulence is covered in Chapter 3. This chapter is divided into two sections. The first section is an Overview of Fourier Optics, covering Maxwell's equations, Wave equation, Fourier transform, Scalar Diffraction theory and Sampling theory. The second section is a review of Atmospheric turbulence, covering its effects on Beam propagation, Phase screens and Split-step propagation.

The simulations part of this report commences in Chapter 4 where the two beam, to be propagated, are modelled first. This chapter also covers the derivation of some system models of power contained in the beams and Atmospheric turbulence, before going ahead to model it.

Chapter 5 shows the modelling of the propagation of the two beams for a range of 2 km. We first propagate the beams without atmospheric turbulence to analyse the effect of diffraction (without turbulence) on the beams. Then we propagate the beams through a constant turbulence in horizontal 2 km path and finally through gradually-weakening turbulence in a vertically-upwards 2 km path. The performance of the two beams is analysed and compared to each other based on some defined performance measures. The main aim of this chapter is to compare the performance of the beams in a horizontal path to that of a vertically-upwards path.

Chapter 6 provides another perspective to the propagation of the two beams, this time from ground to a much longer range of 22 km altitude, which will be defined as turbulence limit. Afterwards, the beams are propagated beyond this turbulence limit height into deep space. The beam performance is also analysed. The Conclusion and Recommendations, including proposed Future works are provided in Chapter 7. Appendix A contains some of the MATLAB functions used for the simulations and Appendix B shows some of the simulation errors as a result of undersampling and not adhering to the sampling conditions.

CHAPTER 2

2.0 OPTICAL BEAMS

Optical beams are electromagnetic waves (covering infra-red up to the UV wavelengths) that remain concentrated around a mean axis when propagated in free space, or electromagnetic waves that are guided by suitable structures [15]. This research concentrates on free-space optical beams. As an optical beam emerges from its laser source, it is well known that its intensity distribution along its cross section will not be uniform but will have a distribution. Many lasers today produce beams with Gaussian-like intensity profiles. The first section of this chapter will give an overview of the Gaussian beam, discussing its intensity profile as well as the energy contained in it. Furthermore, the non-diffracting Bessel beam is fast becoming widely accepted and implemented in optical experiments. The second section of the chapter will discuss the Bessel beam, the methods of producing it, and the energy contained in the beam profile. The third and last section of this chapter will compare the Gaussian beam to the Bessel beam, analysing their pros and cons.

2.1 Gaussian beam

2.1.1 Overview of Gaussian Beam

A Gaussian beam is a beam whose transverse electromagnetic field profile is described by the Gaussian function. The general mathematical expression for the electric field in complex notation for a Gaussian beam is a solution to the paraxial Helmholtz equation and it is given by [16,17]:

$$E_{r,z} = E_0 x \frac{\omega_0}{\omega(z)} \exp\left(\frac{-r^2}{\omega(z)^2}\right) \exp\left(-j\left(kz + k\frac{r^2}{2R(z)} - \psi(z)\right)\right) \qquad (2.1)$$

where:

k=wave number for 1 wavelength.

j=$\sqrt{-1}$, an imaginary unit.

r=radial distance from the centre of the beam.

ω_0= the beam waist radius.

$\omega(z)$=the beam spotsize;

z= the axial distance from the beam source (beam waist).

$\psi(z)$= an extra phase term called the *Gouy phase shift* at point z.

E_0= initial electric field, at r = 0 and z = 0.

$R(z)$= radius of the wavefront of the beam at point z.

These parameters are defined further in the next few pages.

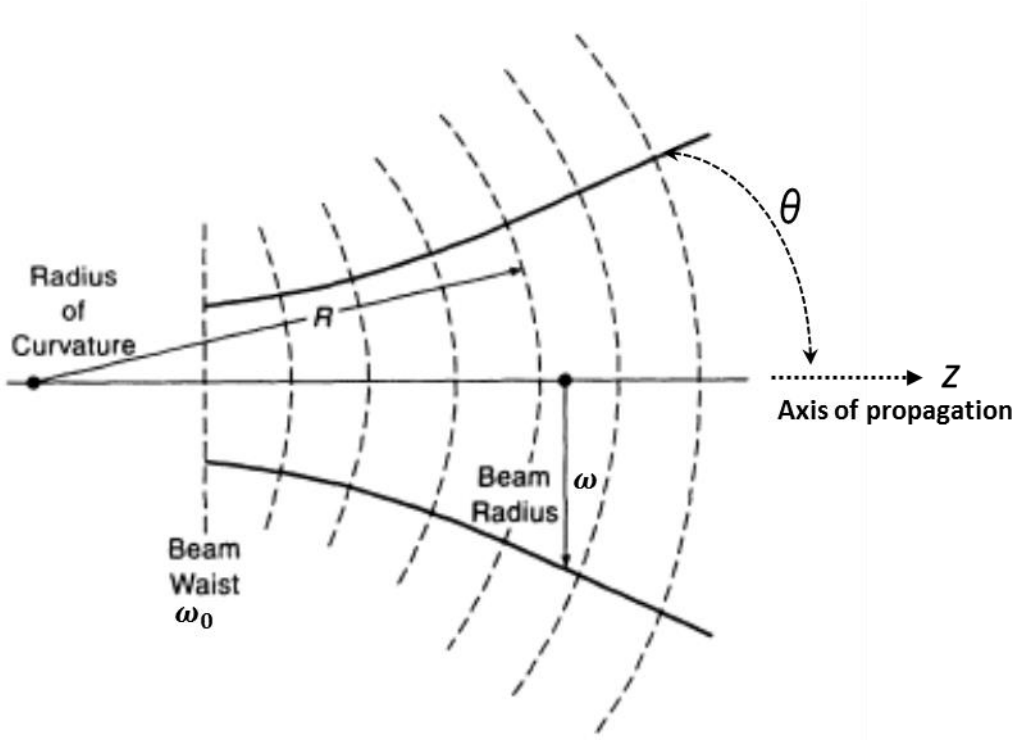

Figure 2.1: Geometry of a Gaussian beam. [Adapted from reference 18]

Gaussian beam has a longitudinal profile with a waist, w_0 beyond which the beam begins to diverge at a constant angle, θ as illustrated in figure 2.1 above. Circular beams have a sharp edge hence a more defined spotsize or beam radius. But for Gaussian beams, the intensity profiles do not have a sharp cut off at the edge. The edge is usually defined as the point where the intensity drops to 13.5% of its peak value [19,20,21]. This is called the *spotsize* or the $1/e^2$ point or the beam waist. For a Gaussian beam of wavelength λ, the beam radius or spotsize after being propagated to a receiver at a distance z is known to be:

$$\omega(z) = \omega_0 \sqrt{\left[1 + \left(\frac{z\lambda}{\pi\omega_0}\right)^2\right]} \tag{2.2}$$

As the beam propagates further the beam radius continues to increase with corresponding decreases in its peak amplitude as seen in figure 2.2 below:

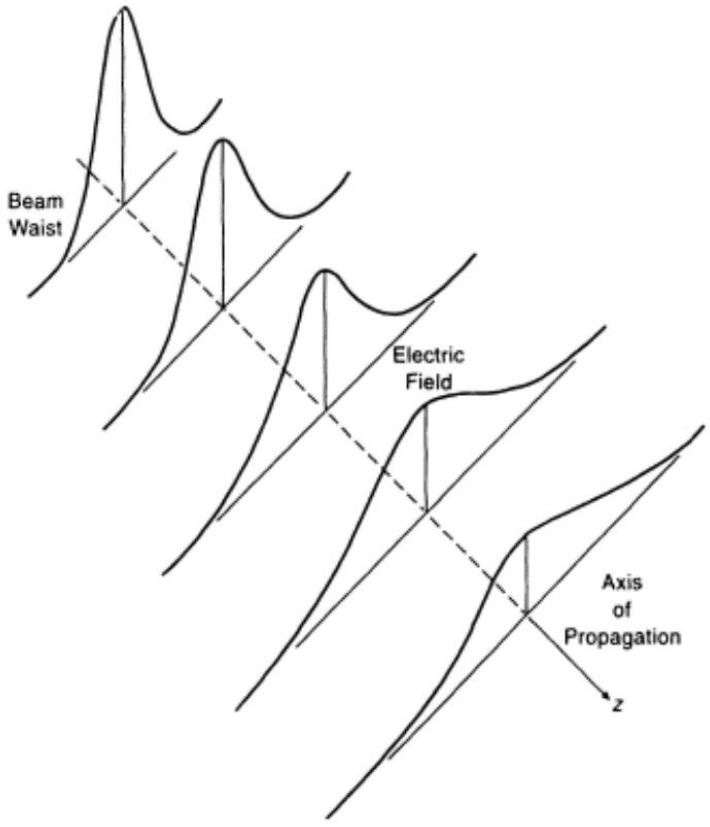

Figure 2.2: Gaussian beam propagation (Source: Goldsmith [17])

At some point down the propagation path, the spotsize $\omega(z)$ of the beam becomes $\sqrt{2}$ larger than its initial value ω_0. This point is called the *Rayleigh range* z_R and is given by:

$$z_R = \frac{\pi\omega_0^2}{\lambda} \tag{2.3}$$

The on-axis intensity at the Rayleigh range ($z=z_R$) is half of its initial value (at z = 0). The expression for the spotsize in equation 2.2 above can be re-written in terms of the Rayleigh range as:

$$\omega(z) = \omega_0\sqrt{1 + \left({}^{z}/_{z_R}\right)^2} \tag{2.4}$$

The angle of divergence of the beam θ (in radians) from the waist, as illustrated in figure 2.1 above, is defined as:

$$\theta \cong \frac{\lambda}{\pi\omega_0^2} \tag{2.5}$$

This shows that the Gaussian beam with a smaller beam waist radius will diverge more than one with a larger waist radius, as it propagates. To minimize divergence in the far field, a laser with large waist radius (aperture) must be ensured. The radius of curvature of the beam wavefront evolves as the beam propagates on and it is given by equation 2.6. Its initial value is zero at the beam waist position and approaches zero at + and – infinity [16,17]:

$$R(z) = z\left[1 + \left(\frac{z_R}{z}\right)^2\right] \tag{2.6}$$

Furthermore, the Gouy phase shift at *z* defined earlier as the additional phase term beyond the phase that can be accounted for by the phase velocity, is given by:

$$\psi(z) = \tan^{-1}\left(\frac{z}{z_R}\right) \tag{2.7}$$

The actual electric field at a particular point is given by the real part of the equation 4.1 above and it is can be expressed as:

$$E_r = E_0 \exp\left(\frac{-r^2}{{\omega_0}^2}\right) \tag{2.8}$$

The Fourier transform of a Gaussian beam is also a Gaussian distribution at every point along the propagation path. The time –averaged Intensity distribution, which is a Gaussian as well, is given by [16,22]:

$$I_{r,z} = I_0\left(\frac{\omega_0}{\omega(z)}\right)^2 \exp\left(\frac{-2r^2}{\omega(z)^2}\right) \tag{2.9}$$

where I_0 is the on –axis intensity at the beam waist given by $I_0 = {E_0^2}/{2\eta}$ and η is the characteristic impedance of the medium of propagation (η = 377Ω in free space).

Most real-life lasers produce beams which are only an approximation of the Gaussian profiles. The degree of variation from the theoretical Gaussian profile is defined by a quality factor called the *M-squared factor*, M^2. The M-squared is the ratio of the *Beam Parameter Product* (BPP) of the real life beam to that of an ideal beam. The BPP, on the other hand, is a term quality used to describe the product of the beam divergence angle θ with the beam waist radius ω_0 [23,24].

$$M^2 = \frac{BPP_{real}}{BPP_{ideal}} = \frac{(\omega_0\theta)_{real}}{(\omega_0\theta)_{ideal}} \tag{2.10}$$

For a theoretical Gaussian beam M^2=1 but for a real-life one, M^2 is greater than 1.

2.1.2 Power contained in the Gaussian beam

As the beam propagates down the path, it diverges resulting in losses in the eventual beam power that reaches the receiver aperture. For a beam with initial total power P_0, the power contained within an aperture of radius, r is [17]:

$$P_{r,z} = P_0\left[1 - \exp\left(-2r^2/\omega(z)^2\right)\right] \tag{2.11}$$

where $P_0 = \pi I_0 \omega_0^2/2$ is the initial beam power at a beam radius ω_0. From equation 2.11, if the radius if the aperture r is equal to the spot size of the arriving beam (r = $\omega(z)$), then:

$$\frac{P_{r,z}}{P_0} = 1 - \exp(-2) \approx 0.865 \tag{2.12a}$$

The equation 2.12 implies that for $r = \omega(z)$, about 86.5% of the beam's initial power is able to pass through the aperture. Likewise, for aperture radius $r = 1.07\omega(z)$, 90% of the beam's initial power is able to pass through the aperture. 95% of the initial power flows through an aperture radius $r = 1.224\omega(z)$ and 99% through an aperture $r = 1.52\omega(z)$[16].

The intensity of the Gaussian beam can be related to the total initial power of the beam as:

$$I_{r,z} = \frac{2P_0}{\pi\omega^2(z)} \tag{2.12b}$$

2.1.3 Peak intensity of a Gaussian Beam

If the limit of the power contained in the aperture in equation 2.11 above is taken, and dividing it by the area of the aperture which is circular and gradually shrinking with distance, then that gives the peak intensity at an on-axis (r = 0) position z away from the beam waist [16, 20,22]:

$$I_{0,z} = \lim_{r \to 0} \frac{P_0 \left[1 - \exp(^{2r^2}/_{\omega(z)^2})\right]}{\pi r^2} \tag{2.13}$$

The above expression in equation 2.13 shows that the on-axis intensity will be high for a small aperture area of the beam. When the limit is computed using *L'Hopital's* rule, the peak intensity is then given by:

$$I_{0,z} = \frac{2P_0}{\pi \omega(z)^2} \tag{2.14}$$

2.1.4 Complex Beam Parameter of Gaussian Beam

In order to help simplify mathematical analyses of Gaussian beam propagation, for example using ray transfer matrices to analyse the optical resonator cavities [25], the Gaussian beam is expressed in terms of a complex beam parameter *q(z)*. This complex beam parameter was introduced in the early days of laser theory and has become a widely acceptable notation in the field. It is expressed in terms of propagation distance z and Rayleigh range z_R as [16,24]:

$$q(z) = z + iz_R \tag{2.15}$$

The equations 2.16 and 2.17 below show that the reciprocal of *q (z)* comprises the radius of curvature of the beam in the real part and the relative on-axis intensity in the imaginary part.

$$\frac{1}{q(z)} = \frac{1}{z + iz_R} = \frac{z}{z^2 + z_R^2} - i\frac{z_R}{z^2 + z_R^2} \tag{2.16}$$

$$\frac{1}{q(z)} = \frac{1}{R(z)} - i\frac{\lambda}{\pi\omega^2(z)} \tag{2.17}$$

When the equations for Gaussian beam electric fields defined earlier is expressed in this form, it is largely simplified. Hence the circular beam field is given by (details of derivation can be found in reference 16):

$$E_{r,z} = \frac{1}{q(z)}\exp(-ik\frac{r^2}{2q(z)}) \tag{2.18}$$

2.1.5 Higher Order Gaussian Modes

In the earlier sections, only one solution of the paraxial wave equation has been considered and this was a Gaussian beam whose width changes as it propagates down its axis. This is certainly the most widely-used solution. However, there are other higher order solutions to the wave equations with beam spot size and radius of curvature of similar attributes as those of the fundamental mode in previous sections, but their phase shifts are different. The higher order modes form a complete and orthogonal set of functions called the *modes of propagation* [17,20]. All arbitrary distribution of monochromatic light can be expanded in terms of these two modes which are:

(a) Modes in the Cartesian coordinates, also called *Hermite-Gaussian mode*:

This mode is used to approximate beam profiles from lasers that are asymmetric in the rectangular coordinate.

(b) Modes in the Cylindrical coordinates, also called *Laguerre-Gaussian mode*:

This mode is suitable to be used to solve beam profiles that are circularly symmetrical and are written using the Laguerre polynomials [26].

Further details about these two modes can be found in reference 17.

More recently, some more higher-order modes have been discussed. They are the modes in elliptical coordinates called the *Ince-Gaussian mode* [27] and another cylindrical coordinate mode called the *Hypergeometric-Gaussian modes* [28].

2.2 Bessel beam

2.2.1 Overview of Bessel Beam

Bessel beam is also a solution to the Helmholtz equation in circular cylindrical coordinates. It is an electromagnetic field whose amplitude is described by the Bessel function of the first kind. It was introduced by Durnin [9] in 1987, who derived the beam profile from the wave equation as follows:

$$\left(\nabla^2 - \frac{1}{c^2}\frac{\partial^2}{\partial t^2}\right) E_{\boldsymbol{r},t} = 0 \tag{2.19}$$

The exact solution of the wave equation in equation 2.19 above for scalar fields propagating into the region z $\geq$ 0 is given as:

$$E_{x,y,z\geq 0,t} = \exp[i(k_z z - \omega t)] \int_0^{2\pi} A(\phi) \exp[ik_r(x\cos\phi + y\sin\phi)]\, d\phi \tag{2.20}$$

where $A(\phi)$ is an arbitrary complex function of ϕ and ${k_r}^2 + {k_z}^2 = k = (\omega/c)^2$ = wave number. The equation 2.20 above represents a class of non-diffracting fields when k_z is real, in the sense that the time-averaged intensity distribution at *z* = 0 is exactly reproduced for all *z* > 0, in every plane that is transverse to the *z* axis:

$$I_{x,y,z\geq 0} = {}^1\!/_2 \left|E_{\boldsymbol{r},t}\right|^2 = I_{x,y,z=0} \tag{2.21}$$

When $A(\phi)$ in equation 2.20 is not dependent on ϕ, a non-diffracting beam of axial symmetry is obtained whose amplitude is proportional to:

$$E_{\boldsymbol{r},t} = \exp[i(k_z z - \omega t)] \int_0^{2\pi} \exp[ik_r(x\cos\phi + y\sin\phi)] \frac{d\phi}{2\pi} \tag{2.22}$$

$$E_{r,t} = \exp[i(k_z z - \omega t)]J_0(k_r r) \tag{2.23}$$

The J_0 is a zero order Bessel function of the first kind and $r = x^2 + y^2$. For k_r = 0, the solution is a plane wave. But for $0 < k_r < k^{1/2}$, the solution is a non-diffracting beam whose intensity distribution changes at a rate inversely proportional to $k_r r$.

Hence an ideal Bessel beam in terms of radial r, azimuthal ϕ and longitudinal z components is given by [17]:

$$E_{r,\phi,z} = A_0 \exp(ik_z z)J_n\,(k_r r)\exp(\pm in\phi) \tag{2.24}$$

where k_r = the radial component of the wave vector = $ksin\theta$, k_z = axial component of wave vector = $kcos\theta$ and k = wave vector = $\sqrt{{k_r}^2 + {k_z}^2} = \frac{2\pi}{\lambda}$. J_n is an *nth* order Bessel function of the first kind. As seen in figure 2.3 below, a zero-order (n = 0) Bessel beam has a bright central core while a higher order Bessel beam has a dark central core.

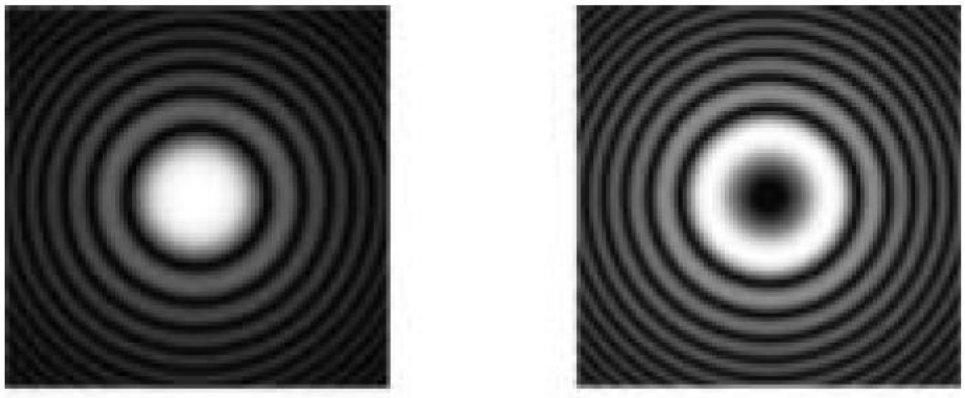

(a) (b)

Figure 2.3: Intensity profile of Bessel beam (a) zero-order beam (b) higher order beam (Source: McGloin and Dholakia [11])

The infinite Bessel beam in equation 2.24 above is only ideal and has to be truncated into an aperture of radius B_w, in practise. This aperture results in the Bessel beam only being non-diffracting over a finite distance, Z_{max}. This can be visualised by considering a set of plane waves propagating through a cone resulting in some phase shift as shown in the figure 2.4 below:

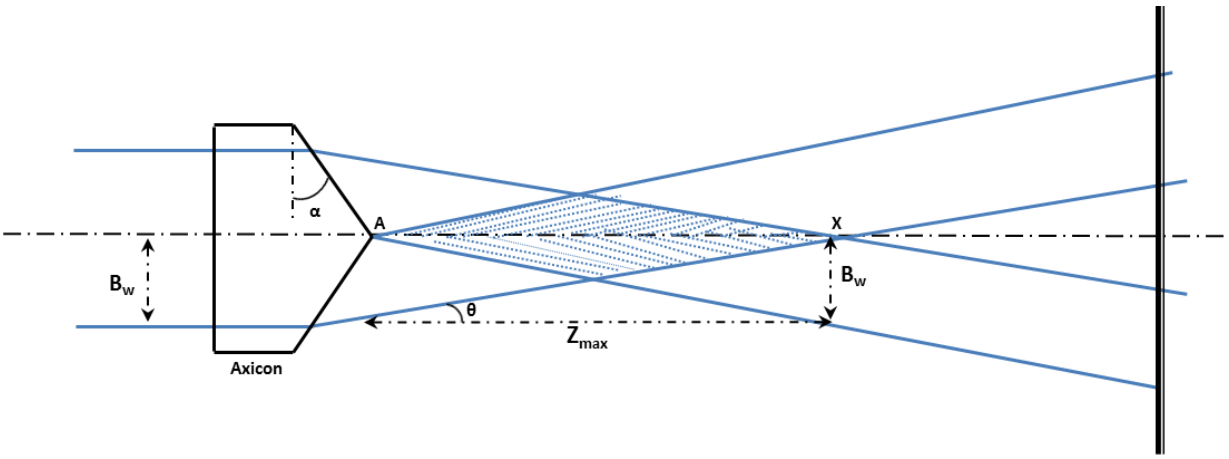

Figure 2.4: Bessel beam decomposed into plane waves

Z_{max} is the shaded portion between point A and X in the figure 2.4 above and it is given by the expression below:

$$Z_{max} = \frac{B_w}{tan\theta} = \frac{B_w k}{k_r} \tag{2.25}$$

Here, θ is the cone angle or the deviation angle of the beam's plane wavefront from the axis of travel defined as follows:

$$\theta = \tan^{-1}\frac{k_r}{k_z} \tag{2.26}$$

$$\theta = (n-1)\alpha \tag{2.27}$$

where *n* is the refractive index of the axicon material and α is the base angle of the cone. Equation 2.25 above shows that to propagate a Bessel beam to a long distance, either B_w has to be large, making the telescope inconveniently large, or k_r must be made small. By limiting k_r such that the aperture function radius is equal to the Bessel function's first root defined as [11]:

$$B_w = \frac{2.405}{k_r} \tag{2.28}$$

we can determine the maximum possible propagation distance:

$$Z_{max} = \frac{{B_w}^2 k}{2.405} \tag{2.29}$$

This allows us to directly equate the maximum distance the beam can propagate with the radius of the transmitter telescope.

Bessel beam possesses a profile that is cylindrically symmetrical: a central core surrounded by a set of nearly-same-energy-level concentric rings. It has been validated that the central core of a Bessel beam is remarkably resistant to diffractive spreading compared to a Gaussian beam with spot size equal to the width of the central core of the Bessel beam [9,10].When propagated, the outer rings of Bessel beams diffract inwardly adding up to the energy of the central core [9,12,13]. This inward diffraction is what helps its on –axis intensity to remain constant as it propagates.

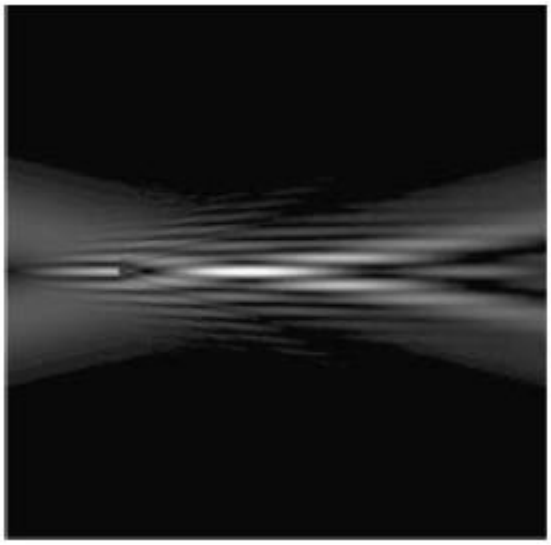

Figure 2.5: Bessel beam self-healing (Source: McGloin and Dholakia [11])

Another effect of the inward diffraction is an attribute called *self- healing*: the beam is capable of recovering back its profile down the path after being scattered by an obstruction. If an object is placed at the centre of the propagating beam, the set of plane waves that create the beam are able to move beyond the obstruction leaving a shadow into the beam. But eventually the beam intensity profile is recreated beyond the obstruction as shown in figure 2.5. This is due to the conical wavefront of the beam [9]. Geometrically, the minimum distance after which the beam is able to regain its profile is given by:

$$z_{selfhealing} \approx \frac{mk}{2k_z} \tag{2.30}$$

where *m* is the width of the obstruction object measured from the centre of the beam.

For a Bessel beam to have its diffraction free attributes, it has to be ideal, with infinite radius and this is not physically realisable. Nevertheless in reality, the apertured Bessel beam can be designed such that it still maintains its desirable non-diffracting attributes over extended distances.

These properties make Bessel beams very promising for various application like the Free Space Optical Communications as well as observatory astronomy. Despite its diffraction-free attribute demonstrated in its longer depth of field, one major downside of the Bessel beam is known to be that each ring carries about the same energy level as the central core which means that the more the number of rings, the less the amount of energy carried by the central core. However, Durnin and his colleagues [29] pointed out that although this fact might seem obvious, it is not necessarily correct. Gaussian beam on the other hand, concentrates the energy but has less depth of field.

2.2.2 Energy contained in Bessel Beam and Power Transferred

An ideal Bessel beam is infinite in radius and consequently infinite in its diffraction-free depth, Z_{max} as well as energy contained. But as earlier mentioned, practical Bessel beams are apertured with a finite Z_{max} and carry a finite amount of energy. Basically, the power contained in the Bessel beam apertured to radius B_w can be obtained by integrating the Bessel beam field in equation 2.24 as:

$$P_{B_w} = A_0^2 \int_0^{2\pi} \int_0^{B_w} J_0^2\,(rk_r) r dr d\phi \tag{2.31}$$

$$P_{B_w} = A_0^2 B_w^2 \pi (J_0(k_r B_w)^2 + J_1(k_r B_w)^2) \tag{2.32}$$

According to Durnin *et al* [29], if the Bessel beam aperture is limited to an initial aperture of radius B_w at z=0, the Z_{max} is given by:

$$Z_{max} = r\sqrt{\left(\frac{k}{k_r}\right)^2 - 1}\ ; \text{for } k > k_r > \frac{2\pi}{r} \tag{2.33}$$

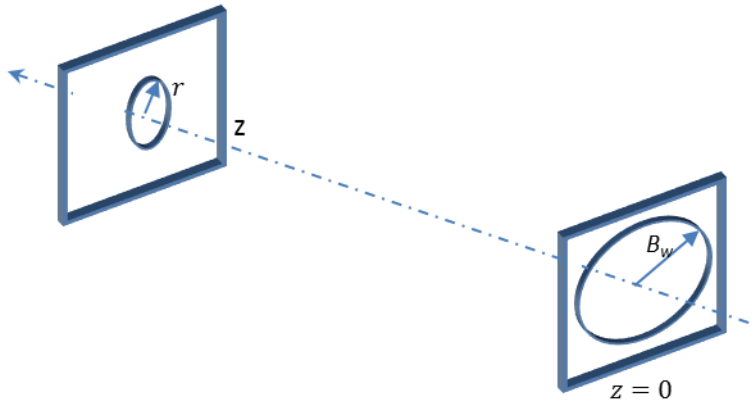

Figure 2.6: Aperture Geometry [Adapted from Durnin *et al*,[29]]

If the radius of the central core of the Bessel beam is equal to the radius *r* of an aperture placed along the propagation plane at a distance *z* away from the initial plane as shown in figure 2.6, the fraction of power *P* of the initial power P_0 (at z=0) that is transferred through the aperture of radius *r* (which is equal to that in the initial plane) is given by [29]:

$$P = \frac{1}{(1 + {}^{4N}/_{3})} \tag{2.34}$$

where *N* is the number of rings of the Bessel beam captured in the initial aperture of radius B_w. Hence if B_w is chosen such that there is no rings (N = 0) and only the central

spot fills up the initial aperture, then *P* in equation 2.34 will be equal to 1 meaning no power loss. If the Z_{max} in equation 2.33 is expressed in terms of *r*, it will be expressed as:

$$Z_{max} \approx {}^{\pi B_w r}/_{\lambda} \tag{2.35}$$

From equation 2.35 above, B_w is derived as:

$$B_w = {}^{\lambda z}/_{\pi r} \tag{2.36}$$

Hence, the fraction of power *P* of the initial power transferred through aperture *r* is given as:

$$P = \frac{r}{B_w} = \frac{\pi r^2}{\lambda z} \tag{2.37}$$

where the total initial power P_0 is defined as:

$$P_0 = \left(\frac{c}{2\pi}\right) A_0^2 \frac{B_w}{k_r} \tag{2.38}$$

and the *c* is the speed of light and A_0 is the Bessel beam amplitude defined as:

$$A_0^2 = \left(\frac{4\pi}{c}\right)\left(\frac{P_0}{B_w r}\right) \tag{2.39}$$

2.2.3 Bessel beam Production

Bessel beams are produced mainly by two methods namely [30]:

- Using refractive axicon lenses called Durnin rings, and
- Using diffractive elements called holographic plates.

2.2.3.1 Axicon or Durnin Ring Method

The most common method is using the axicon – a conical lens. Axicons convert the incoming collimated light into waves propagating through its conical surface which are approximations of Bessel beams [31,32].

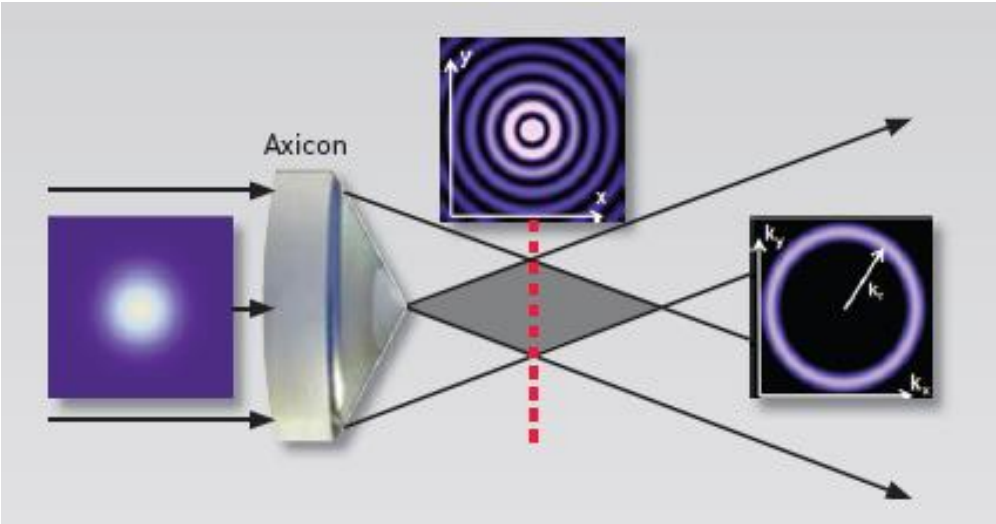

Figure 2.7: Bessel beam generation using an axicon [33]

Bessel beam produced using the axicon method only exist at the near field as seen in the figure 2.7 above, while an annular ring is formed at the far field. Since the Bessel beam has an annular ring in its far field, they can be generated, as done by Durnin *et al* [34,35], by combining an annular slit with a Fourier transforming lens [33]. The set up Durnin *et al* used here was a coherent plane wave illuminating the thin annular slit placed along the focal plane of a positive lens. They demonstrated satisfactory agreement with the initial prediction and their experimentally measured transverse and longitudinal intensity distributions. If the aperture of the lens was infinite, the conical Bessel wavefront after the lens would have been independent of the distance of propagation. However since the aperture of the lens will have to be truncated in practice, the Bessel beam wavefront will exist for a limited distance, *Zmax*.

The Durnin ring method has the advantage of being compatible with microfabrication technology as the rings can easily be fabricated in mass production using conventional lithography techniques. This method is also simple and easy to align. However, this method has a disadvantage of having a small amount of energy passing through the ring, and hence transported by the resulting beam [31]. If one attempts to increase the size of the ring in order to allow more power, it will reduce the beam quality. The axicon method, on the other hand is more efficient than the ring method as it utilises the whole or most of the incident Gaussian beam.

2.2.3.2 Holographic Plates Method

The alternative experimental set up for generating an approximate Bessel beam is using a holographic optical element (HOE) [36]. Here, the incident plane wave is directly modulated in amplitude or in phase by a computer – generated hologram (CGH) often implemented using a Spatial light modulator (SLM) [37]. A good number of authors have implemented the phase modulation holographs, which encode the CGH with the phase profile [38,39,40,41]:

$$T_{\rho,\theta} = \exp(in\theta)\exp(-\frac{i2\pi r}{k_r}) \tag{2.40}$$

The HOE performs the conversion of incident plane wave to a conical wave with the attributes of a Bessel beam. Again in this method, the HOE aperture is finite and this implies that the resulting Bessel beam will be limited to the distance Z_{max} but using this method, the Z_{max} is twice that for the first method, which gives the holographic method an advantage.

Furthermore, the holographic method offers up to a 100% power conversion efficiency from the input flat top beam to resulting approximate Bessel beam. The intensity distribution of the resulting Bessel beam was satisfactorily similar to the theoretical Bessel beam. However, it was observed that the peak intensity of the central core varied with distance, with a maximum towards the end of the useful focal range [42].

Some work has also been done to show that higher order non-diffracting beams can be experimentally generated using holographic elements [40,43].

2.3 Comparison of Gaussian and Bessel Beams

Some authors have done some work in the past attempting to compare these two beams [29, 44]. The first basis for comparison is energy focusing and diffraction attributes. Gaussian beams concentrate the energy but are known to be diffracting the energy as it propagates. On the other hand, Bessel beams are non-diffracting but do not concentrate all its energy along the central axis. The central core of the Bessel beam is known to possess desirable non-diffractive attributes. However, since each of the side lobes has nearly equal energy with the central core, a Bessel beam with say more than 20 side rings will have less than 5% of the energy in the central core. This off-axis energy waste is a major disadvantage for the Bessel beam compared to the Gaussian beam whose energy is more localized with up to 50% of its energy within the Full Width Half Maximum (FWHM). This fact is still in debate out there [29].

Another basis of comparison of these two beams will be the definition of their spot sizes or beam radius. It is generally easier to define the spot size of a beam that has a well-

defined and sharp edge. The Gaussian beam intensity profile does not have a sharp edge. Its spot size is usually defined as the $1/e^2$ point, which is the point when the intensity drops to 13.5% of its peak value. The Bessel beam, on the other hand, reaches its first zero at a well specified value, $J_1(3.8) = 0$, which is the first root (dark ring) and this a region of destructive interference. Hence, the spot size of a Bessel beam is the radius of its central core [19]. Hence generally speaking, the comparison between Bessel and Gaussian beams is usually between the Bessel beam's central core and a Gaussian beam of similar spot size.

With respect to beam divergence, the Gaussian beam spreads by a factor of $\sqrt{2}$ at the Rayleigh range position while the central core of the Bessel beam remains free from spreading within its Z_{max} which is comparable to the Rayleigh range. If both Gaussian and Bessel beams have the same FWHM at the initial plane (z = 0), Durnin *et al* [29] defined a relationship in terms of the distance at which their peak intensity drops to 50% of its initial value, $Z_{0.5Intensity}$. The Bessel beam's half-intensity distance is given as:

$$Bessel\ Z_{0.5Intensity} \approx Gaussian\ Z_{0.5Intensity} \times N \tag{2.41}$$

where N is the number of rings of the Bessel beam at the initial plane. It is clear from equation 2.41 that the more the number of rings N of the Bessel beam, the longer its non-diffracting distance. In addition, since the total integral power in each ring of the Bessel beam is roughly equal to that in the central core, a similar relation occurs for the total power in the beams:

$$Bessel\ P_{total} \approx Gaussian\ P_{total} \times N \tag{2.42}$$

2.4 Chapter Summary

This chapter covered the basic theory on the Gaussian and Bessel beams. For the Gaussian beam, we did a review of the beam profile, power contained in the beam, the peak intensity, the complex beam parameter and the higher order Gaussian beams. For the Bessel beam, we covered the beam profile, the energy contained in the beam, the power transferred in the beam and the two beam production methods: the holographic plate method and the Durnin ring method. We dedicated a full section to discuss on the comparison of the attributes of the two beams based on energy focusing and diffractive attributes, definition of their spot sizes and beam divergence.

CHAPTER 3

3.0 THE THEORY OF FREE SPACE OPTICAL PROPAGATION THROUGH ATMOSPHERIC TURBULENCE

In this chapter, the theory behind the propagation of the two optical beams analysed in chapter two, the Gaussian beam and Bessel beam, is considered. One of the main techniques used for modelling the propagation of beams from one point to another is called Fourier Optics. An overview of Fourier optics, starting from the Maxwell's equations down to sampling theory, is what comprises the first section of this chapter. The second section will encapsulate the theory of atmospheric turbulence, its causes, its effects on the propagated beam and how it can be modelled on the computer.

3.1 Overview of Fourier Optics

Since the advent of the discipline of Fourier Optics in the 1940s, it has become fundamental in the analysis of imaging, diffraction, holography and even in applications like wave propagation through random media. It utilises Fourier transforms in the study of classical optics. In Fourier optics, the optical wave is considered as a superposition of plane waves that are not traceable to any identifiable source. This section of the chapter essentially summarises some basics of Fourier Optics starting from derivations of the fundamental preliminary theories like the Maxwell's equations, wave equation and Helmholtz equation which are the building blocks for Fourier optics. This section will also cover the Fourier transform which is an important tool in Fourier Optics. Next, the Scalar Diffraction theory will be summarised here, which describes the evolution of an optical field as it propagates from source to destination. The last sub-section expatiates on the constraints considered when sampling the real signals onto computer simulations.

3.1.1 Maxwell's Equations

Maxwell's equation is a set of paraxial differential equations that describes the electric field and the magnetic field, as well as the relationship between these two fields, electric charge and currents. Although Maxwell's equations are only approximations and not absolutely accurate, their solutions encompass all the diverse set of phenomena in classical electromagnetism. In Fourier optics, optical fields are seen as solutions to the Maxwell's equation, hence the need for it to be summarised here. Jason Schmidt [45] did a thorough job in deriving these equations and his notation will be followed in this section.

The interaction of any test charge with any bulk material of non-zero volume current density **J**, volume polarisation density **P** and volume magnetisation density **M**, generates a force on the charge. This electrostatic force, as described by Lorentz force law, is a function of two field vectors; the electric field, **E** and the magnetic induction, **B** [46]:

$$F_{electrostatic} = q(\mathbf{E} + v \times \mathbf{B}) \tag{3.1}$$

The force is either in same direction or opposite direction to the field, hence the name *push-and-pull* force. When these two fields were related to the sources, Maxwell's equations were derived experimentally and mathematically. The Maxwell's equations describe the Faraday's law:

$$\nabla \times \mathbf{E} + \frac{\partial \mathbf{B}}{\partial t} = 0 \tag{3.2}$$

and the Ampere's law:

$$\nabla \times \mathbf{B} - \epsilon_0 \mu_0 \frac{\partial \mathbf{E}}{\partial t} = \mu_0 \left(\mathbf{J} + \frac{\partial \mathbf{P}}{\partial t} + \nabla \times \mathbf{M} \right) \tag{3.3}$$

where ϵ_0 is the permittivity of free space or electric constant and μ_0 is permeability of free space or magnetic constant. When the Ampere's law in equation 3.3 is re-expressed in a more functional form as:

$$\nabla \times \left(\frac{\mathbf{B}}{\mu_0} - \mathbf{M} \right) = J + \frac{\partial}{\partial t} (\epsilon_0 \mathbf{E} + \mathbf{P}) \tag{3.4}$$

then the definitions for the medium's response to the applied fields, electric displacement **D** and magnetic field **H**, can be made:

$$\mathbf{D} = \epsilon_0 \mathbf{E} + \mathbf{P} \tag{3.5}$$

$$\mathbf{H} = \frac{\mathbf{B}}{\mu_0} - \mathbf{M} \tag{3.6}$$

Hence, the Maxwell's equations are now re-expressed as:

$$\nabla \times \mathbf{E} = -\frac{\partial \mathbf{B}}{\partial t} \tag{3.7}$$

$$\nabla \times \mathbf{H} = \mathbf{J} + \frac{\partial \mathbf{D}}{\partial t} \tag{3.8}$$

Furthermore, after relating equation 3.7 and 3.8 with the conservation of charge and performing some algebraic manipulation before the source is turned on, Coulomb's law (also part of the Maxwell's equations) is deduced as:

$$\nabla . \mathbf{D} = \rho \tag{3.9}$$

$$\nabla . \mathbf{B} = 0 \tag{3.10}$$

It is necessary to define a few relations in order to apply Maxwell's macroscopic equations, which have an undesirably high number of unknown scalars and vectors. These relations are called Constitutive relations [47] and they are as follows:

$$\begin{aligned} \mathbf{P} &= \epsilon_0 \chi_e \mathbf{E} \\ \mathbf{M} &= \chi_m \mathbf{H} \\ \mathbf{D} &= \epsilon \mathbf{E} \\ \mathbf{B} &= \mu \mathbf{H} \end{aligned} \tag{3.11}$$

where χ_e and χ_m are the electric and magnetic susceptibilities respectively and ϵ and μ are the electric permittivity and magnetic permeability respectively. Substituting the constitutive relations into equations 3.7 and 3.8 simplifies them to:

$$\nabla \times \mathbf{E} = -\mu \frac{\partial \mathbf{H}}{\partial t} \tag{3.12}$$

$$\nabla \times \mathbf{H} = \mathbf{J} + \epsilon \frac{\partial \mathbf{E}}{\partial t} \tag{3.13}$$

Hence, the Maxwell's equations are equations 3.7, 3.8, 3.9, 3.10, 3.12 and 3.13.

3.1.2 Scalar Wave Equation and Helmholtz Equation

The Maxwell's equations defined in the immediate previous section can be refined into uncoupled *wave equations*, written in closed form without an integral. The wave equation shows that all waves travel at a single speed, which is the speed of light. The Helmholtz equation, which also shows up in Quantum mechanics and Thermodynamics, is a time-independent form of the wave equation often used to reduce the complexity of the analysis.

This sub-section will show how the wave equation and the Helmholtz equation are derived from the Maxwell's equations (that is the Ampere law and the Faraday's law), based on Goodman [48] and Schmidt's [45] notations. If a source-free region is assumed here, no charges nor currents are flowing in the medium. This implies that, $\mu = \mu_0$, and $\rho = \mathbf{J} = 0$, ϵ is a scalar independent of wavelength, position in space and time. From equations 3.12, taking the curl results in:

$$\nabla \times (\nabla \times \mathbf{E}) = -\mu_0 \frac{\partial}{\partial t} (\nabla \times \mathbf{H}) \tag{3.14}$$

and substituting equation 3.13 into the above yields:

$$\nabla \times (\nabla \times \mathbf{E}) = \mu_0 \epsilon \frac{\partial^2}{\partial t^2} \mathbf{E} \tag{3.15}$$

By vector identity to the LHS of equation 3.15, it becomes:

$$\nabla(\nabla . \mathbf{E}) - \nabla^2 \mathbf{E} = \mu_0 \epsilon \frac{\partial^2}{\partial t^2} \mathbf{E} \tag{3.16}$$

Substituting equation 3.9 and $\mathbf{D} = \epsilon \mathbf{E}$ from equation 3.11 into equation 3.16 now yields:

$$\nabla^2 \mathbf{E} - \mu_0 \epsilon \frac{\partial^2}{\partial t^2} \mathbf{E} = 0 \tag{3.17}$$

where ∇^2 is the Laplacian operator. Similarly, taking the curl of 3.13, substituting equation 3.12 into it, applying the vector identity and equivalent substitutions yields a corresponding equation for magnetic field:

$$\nabla^2 \mathbf{B} - \mu_0 \epsilon \frac{\partial^2}{\partial t^2} \mathbf{B} = 0 \tag{3.18}$$

For the purpose of simplification, when the vector field **E** and **B** are now replaced a common term for scalar field in the Cartesian coordinate, it results in *the Scalar Wave Equation* given as:

$$\left(\nabla^2 - \mu_0 \epsilon \frac{\partial^2}{\partial t^2}\right) U_{x,y,z} = 0 \tag{3.19}$$

The Scalar Wave equation can also be expressed in terms of the speed of light $c = \frac{1}{\sqrt{\mu_0 \epsilon_0}}$ and refractive index $n = \sqrt{\epsilon / \epsilon_0}$ below:

$$\left(\nabla^2 - \frac{n^2}{c^2}\frac{\partial^2}{\partial t^2}\right) U_{x,y,z} = 0 \tag{3.20}$$

According to Goodman [48], all components of a linear, homogenous, isotropic and nondispersive dielectric medium behave identically and their behaviour is described by a single Scalar wave equation. The scalar theory is known to be accurate as long as the diffracting structures are large compared with the wavelength of the light signal. Optical signals comprise electric field **E** and magnetic field **B** that are time harmonic travelling waves. Hence substituting $\exp(-i2\pi\nu t)$ into equation 3.20 yields the *Helmholtz equation*:

$$\left[\nabla^2 + \left(\frac{2\pi n \nu}{c}\right)^2\right] U = 0 \tag{3.21}$$

In terms of the wave number $k = 2\pi/\lambda$ and wavelength $\lambda = c/\nu$, the Helmholtz equation is commonly expressed as:

$$[\nabla^2 + k^2 n^2] U = 0 \tag{3.22}$$

3.1.3 Review of Fourier Analysis

Fourier analysis is a very important tool in Fourier Optics as well as Electrical networks, useful for the analysis of linear and non-linear phenomena. The fundamental mathematical concepts of the Fourier theory is well treated by Bracewell [49]. The following sections will cover the Fourier analysis of functions of two independent variables, also covered by Goodman [48].

3.1.3.1 Definition of analytical Fourier Transform

The analytical Fourier transform of a 2-dimentional spatial function $g(x, y)$ is defined as:

$$G(f_x, f_y) = \Im\{g(x, y)\} = \int_{-\infty}^{\infty}\int_{-\infty}^{\infty} g(x, y)e^{-i2\pi(f_x x + f_y y)}dxdy \tag{3.23}$$

where f_x and f_y are independent spatial-frequency variables associated with spatial variables *x* and *y*. The analytical reverse, called the inverse Fourier Transform, is given by:

$$g(x, y) = \Im^{-1}\{G(f_x, f_y)\} = \int_{-\infty}^{\infty}\int_{-\infty}^{\infty} G(f_x, f_y)e^{i2\pi(f_x x + f_y y)}df_x df_y \tag{3.24}$$

The above two definitions of the Fourier transform is only mathematically realisable if the function $g(x, y)$ satisfies the conditions listed below [48, 50]:

i. $g(x, y)$ must have only a finite number of discontinuities.
ii. $g(x, y)$ must be absolutely integrable over the infinite range of x and y.
iii. $g(x, y)$ must have no infinite discontinuities.

However, it has been demonstrated that some of the above conditions can be weakened in some important cases, and proposed an idealised transform approach to be used to find useful transform representations [48]. In Fourier analysis, the Fourier Transform defined in equation 3.23 and 3.24 have some basic mathematical properties presented as the theorems listed below:

I. Linearity theorem
II. Similarity theorem
III. Shift theorem
IV. Rayleigh's or Parseval's Theorem
V. Convolution theorem
VI. Autocorrelation Theorem
VII. Fourier integral theorem.

Table 3.1: Fourier Transforms of basic functions

Functions	**Definition**	**Fourier Transform**
Rectangle	$rect\left(\frac{x}{a}\right)$	$\|a\|sinc(af_x)$
Sinc	$sinc\left(\frac{x}{a}\right)$	$\|a\|rect(af_x)$
Triangle	$\Lambda\left(\frac{x}{a}\right)$	$\|a\|sinc^2(af_x)$
Comb	$comb\left(\frac{x}{a}\right)$	$\|a\|comb(af_x)$
Circle	$circ\left(\frac{\sqrt{x^2+y^2}}{a}\right)$	$a^2\frac{J_1(2\pi a\sqrt{f_x^2+f_y^2}}{a\sqrt{f_x^2+f_y^2}}$
Chirp	$\exp\left[-\pi\left(\frac{x^2}{a^2}+\frac{y^2}{b^2}\right)\right]$	$\|ab\|\exp[-\pi(a^2f_x^2+b^2f_y^2)]$

Since different basic functions are used to describe various physical or analytical apertures and structures in optics, then defining the Fourier Transforms of the basic functions can be useful in finding diffraction solutions. The table 3.1 above presents the basic functions and their Fourier Transforms, as highlighted by David Voelz [50].

3.1.3.2 Discrete Fourier Transform

For modelling the Fourier optics problem, the analytical continuous Fourier optics expression in equation 3.23 has to be discretized; this is called the Discrete Fourier Transform (DFT). The forward and inverse Discrete Fourier Transform, as will be defined in this section, are not usually directly implemented for simulations, but are most efficiently presented in the form called the Fast Fourier Transform (FFT). FFT algorithms are not most efficient when *M* and *N* are of a power of 2. The Fourier Transform in equation 3.23 can be approximated using a Riemann sum, substituting for the equation

$$\int_{-\infty}^{\infty}\int_{-\infty}^{\infty} \dots dxdy \tag{3.25}$$

with

$$\sum_{n=-N/2-1}^{N/2-1}\sum_{m=-M/2-1}^{M/2-1} \dots \Delta x\Delta y \tag{3.26}$$

Although the $\Delta x\Delta y$ is not included in the DFT definition which operates on discrete values without details of sample intervals, it is needed for appropriate scaling of a physical problem. The derivation for the expression for the DFT of $g(x,y)$ [now presented here as $g(m,n)$] is given as[50]:

$$G_{DFT}(p,q) = \sum_{m=-M/2-1}^{M/2-1} \sum_{n=-N/2}^{N/2-1} g(m,n) \exp\left[-i2\pi\left(\frac{pm}{M} + \frac{qn}{N}\right)\right] \quad (3.27)$$

and the inverse DFT of $G_{DFT}(p,q)$ as:

$$g(m,n) = \frac{1}{MN} \sum_{p=-M/2}^{M/2-1} \sum_{q=-N/2}^{N/2-1} G_{DFT}(p,q) \exp\left[i2\pi\left(\frac{pm}{M} + \frac{qn}{N}\right)\right] \quad (3.28)$$

where the continuous frequency domain samples f_x and f_y in the continuous Fourier transforms are now divided into *M* and *N* evenly-spaced coordinate values. The *p* and *q* are integer multiples of the frequency sample intervals are defined as $-M/2 < p < M/2 - 1$ and $-N/2 < q < N/2 - 1$, and have the same values as *m* and *n* respectively.

One major downside of the FFT is seen in indexing of array data values as well as arrangement of the coordinates. In square grids, it is convenient to a *centre* the coordinate position for the function of interest in the vector, for display purposes. But the centred vector needs to be shifted first before any FFT operation is carried out. Another major difference between the Discrete Fourier transform and the analytical Fourier transform is that the results of the DFT has an attribute called periodic extension, discussed in detail by Brigham [51].

3.1.4 Scalar Diffraction

The Scalar Diffraction theory in Fourier Optics describes the propagation of an optical signal from one point to another, under an ideal condition where the medium of propagation is assumed to be linear, homogenous, isotropic, nonmagnetic and nondispersive. Based on the Scalar diffraction theory, the propagation of electromagnetic waves through a vacuum is analogous to a linear system where a convolution of a monochromatic electric field magnitude in the source plane and the impulse response of the free-space channel will result in the electric field magnitude in the observation plane [48]. This is why Scalar Diffraction is known as the physical basis of wave optics. The concept of the linear systems, when combined with Fast Fourier Transform makes it efficient for computation of wave optics scenarios.

When an optical signal is confined to an aperture, the optical signal is said to be going through Diffraction. Unlike reflection and refraction which are more obvious in our everyday life, diffraction is only noticed when the optical wave is laterally confined to an aperture of dimension on the order of the wavelength of the optical signal [48, 52]. Hence, Sommerfeld [53] defines diffraction as the deviation of light rays from the rectilinear paths, which cannot be interpreted as refraction nor reflection. The diffraction effect is a general attribute of a wave that occurs when a portion of a wavefront encounters an obstruction resulting in alteration of its amplitude or phase [54,55]. The interference of the sections of the wavefront that propagates beyond the obstacle causes an energy distribution called the *diffraction pattern*.

3.1.4.1 The Huygens-Fresnel Principle

Christiaan Huygens [56] proposed a principle that every single point on any wavefront can be considered as a source of secondary spherical wavelets. The shape of the wavefront, at every instant, is the envelope of the secondary wavelets. The limitation of this principle is that it ignores the majority of these secondary wavelets and taking into consideration only the portions that are common to the envelope. This way, it is unable to account for most of the diffraction process. This limitation was resolved by Fresnel in 1818 [57], who modified the Huygens's principle mathematically and added the concept of interference to it. The resulting *Huygens-Fresnel principle* states that every unobstructed point of a waveform, at any instant, serves as a source of spherical secondary wavelets (with the same frequency as that of the primary wave). The amplitude of the optical field at any point beyond is the superposition of all these wavelets, considering all their amplitudes and relative phases. A bit later on in 1882, Gustav Kirchhoff [58] showed that the Huygens-Fresnel principle was a direct consequence of the differential wave equation. Sommerfeld eventually modified the Kirchhoff's theory by making use of the Green's function, eliminating the assumption concerning the amplitude of light. The Sommerfeld's theory is called the *Rayleigh-Sommerfeld diffraction theory*. The Rayleigh-Sommerfeld Diffraction solution is an accurate and a general expression used to predict field at the observation plane.

Based on the Huygens-Fresnel principle, the observation plane $U_2(x, y)$, at a distance z from the source field $U_1(\xi, \eta)$, in rectangular coordinates, can be written as:

$$U_2(x,y) = \frac{z}{i\lambda} \iint_{\Sigma}^{\Sigma=aperture} U_1(\xi,\eta) \frac{\exp(ikr_{12})}{r_{12}^2} d\xi d\eta \tag{3.29}$$

The $r_{12} = \sqrt{z^2 + (x-\xi)^2 + (y-\eta)^2}$ is the separation between a point on the source plane and another point of the observation plane, *k* is the wavenumber and λ is the wavelength of the optical signal. Some approximations to this general theory have been derived which have helped reduce diffraction pattern calculations to simple mathematical manipulations. These approximations are the *Fresne*l and *Fraunhofer Diffraction approximations* [48].

3.1.4.2 Fresnel Diffraction Approximation

By introducing some binomial approximations for the distance variable r_{12} in the general the equation 3.29 above, explained in details by Voelz [52], the Fresnel approximation is derived as:

$$U_2(x,y) = \frac{e^{ikz}}{i\lambda z}\iint U_1(\varepsilon,\eta) exp\left\{i\frac{k}{2z}[(x-\varepsilon)^2 + (y-\eta)^2]\right\} d\varepsilon d\eta \tag{3.30}$$

Equation 3.30 can be expressed as a convolution integral expressed below:

$$U_2(x,y) = \iint U_1(\varepsilon,\eta) h(x-\varepsilon, y-\eta) d\varepsilon d\eta \tag{3.31}$$

When the Fourier convolution theorem is applied to equation 3.31 above, where both source and observation planes are parallel and assumed to have the same variables *x* and *y*, the following expression is obtained:

$$U_2(x,y) = \mathfrak{I}^{-1}\{\mathfrak{I}\{U_1(x,y)\}\mathfrak{I}\{h(x,y)\}\} \tag{3.32}$$

with its equivalent equation given as:

$$U_2(x,y) = \Im^{-1}\{\Im\{U_1(x,y)\}H(f_X,f_Y)\} \tag{3.33}$$

Typically, Equations 3.32 and 3.33 above are both similar Fresnel (near field) diffraction expressions but are liable to produce different results due to some sampling criteria discussed in detail in section 3.1.5.3. Here, *H* and *h* are the Rayleigh-Somerfield *Transfer Function (TF)* and *Impulse Response (IR)* function respectively, given by:

$$h(x,y) = \frac{e^{jkz}}{j\lambda z} exp\left[\frac{jk}{2z}(x^2+y^2)\right] \tag{3.34}$$

$$H(f_X,f_Y) = e^{jkz} exp\left[-j\lambda z\pi\left({f_X}^2+{f_Y}^2\right)\right] \tag{3.35}$$

Fresnel propagators are modelled by implementing either equations 3.34 or 3.35 depending which one suits the regime under consideration.

The two different forms of Fresnel approximation Integral expression in 3.32 and 3.33 are presented differently to aid numerical evaluations. Jason Schmidt [59] went deeper to analyse these two forms and calls them the Fresnel Integral and the Angular Spectrum forms respectively:

3.1.4.2.1 Fresnel Integral Form or Fresnel Transfer Function

The first method is obtained from the equation 3.30 by expanding the squared terms in the exponential and factoring out the integrals, resulting in the expression:

$$U_2(x,y) = \frac{e^{ikz}}{i\lambda z} e^{i\frac{k}{2z}(x^2+y^2)} \iint \left[U_1(\xi,\eta) e^{i\frac{k}{2z}(\xi^2+\eta^2)}\right] e^{-i\frac{2\pi}{\lambda z}(x\xi+y\eta)} d\xi d\eta \qquad (3.36)$$

This approach can either be a one-step Fourier Transform which is more straightforward or a two-step propagation which computes the Fresnel integral twice and adds some flexibility in the grid spacing. The one-step propagation is more efficient computationally where the observation plane field is obtained by a single Fourier Transform step: the source field is multiplied by a quadratic phase factor, Fourier transformed, converted from a spatial frequency coordinate to spatial coordinate, and multiplied by another quadratic phase factor.

3.1.4.2.2 Angular Spectrum Form or Fresnel Impulse Response

The second method has to do with treating the Fresnel integral in equation 3.30 as a convolution of the source field and the free-space amplitude spread function:

$$U_2(x,y) = U_1(\xi,\eta) \otimes \left[\frac{e^{ikz}}{i\lambda z} e^{i\frac{k}{2\Delta z}(\xi^2+\eta^2)}\right] \qquad (3.37)$$

This method has been treated and applied by some authors in the past [60,61].

3.1.4.3 Fraunhofer Diffraction Approximation

The Fraunhofer approximation of the Rayleigh-Sommerfeld diffraction solution has no impulse response nor transfer function, hence cannot be written as a convolution integral. It is commonly called the *far field* diffraction and Goodman [48] expressed it as:

$$U_2(x_2, y_2) = \frac{e^{ikz} e^{i\frac{k}{2z}(x^2+y^2)}}{j\lambda z} \iint U_1(\varepsilon, \eta) exp\left[-i\frac{2\pi}{\lambda z}(x\varepsilon + y\eta)\right] d\varepsilon \, d\eta \qquad (3.38)$$

The Fresnel number criterion is generally used to determine when the Fresnel expression can be applied with minimal loss of accuracy or when the Fraunhofer is suitable. The Fresnel number is given by:

$$N_f = \frac{w^2}{\lambda z} \qquad (3.39)$$

If N_f is far less than (<<) 1, then the observation plane is generally regarded to be in the Fraunhofer region. But if N_f is > 1, then it is in the Fresnel zone. However, if the N_f is less than or equal to 1, it is commonly acceptable that the observation plane is in the Fresnel region, hence the Fresnel approximation is applied for useful results. It is considered in Fraunhofer region when N_f is more that 20 to 30 times less than 1.

3.1.5 Sampling Theory

When modelling the wave optics on the computer, functions are represented with discrete arrays of sampled values, then transforms are applied to them and processed, as needed. To represent the functions as accurately as possible, the physical element will need to be represented with several samples, but at the expense of the execution timing and computing memory requirements. Hence the aim in practical simulations will always be to strike a balance between these two factors [48,50]. If the function $g(x, y)$ is sampled in the *x* and *y* directions with sample interval Δx and Δy respectively, the sampling is described as:

$$g(x, y) \rightarrow g(m\Delta x, n\Delta y) \tag{3.40}$$

where *m* and *n* are integers representing the indices of the samples often defined with the following values, for a finite sampled space with $M \times N$ number of samples:

$$-\frac{M}{2} \leq m \leq \frac{M}{2}, \qquad -\frac{N}{2} \leq n \leq \frac{N}{2} \tag{3.41}$$

The lengths of the physical area L_x and L_y, in the *x* and *y* directions respectively, are given by:

$$L_x = M\Delta x, \qquad L_y = N\Delta y \tag{3.42}$$

It is important to define a support span area, $D_x \times D_y$ within the physical area, $L_x \times L_y$ where the significant part of the values of the function $g(x, y)$ will be contained, to ensure they fit into the physical area. This entails that

$$D_x < L_x \text{ and } D_y < L_y. \tag{3.43}$$

It is a good practise to provide an extra area called the guard area around the area of interest to help reduce artifacts at the edges of the observation array after propagation due to the periodic extension properties of the FFT. In this case the array side lengths

$$D_x < 2L_x \text{ and } D_y < 2L_y \tag{3.44}$$

Furthermore, to ensure that the sample intervals Δx and Δy are small enough to preserve the features of the function $g(x, y)$, the *Shannon-Nyquist* sampling theory defines a requirement for bandlimited functions needed to ensure an exact recovery of a continuous function from the samples. This sampling criterion requires that the sample intervals be smaller than a specific value, as defined in equation 3.45 below, in terms of the spectral bandwidths B_x and B_y in the *x* and *y* directions respectively [48]:

$$\Delta x < \frac{1}{2B_x}, \qquad \Delta y < \frac{1}{2B_y} \tag{3.45}$$

In relation to this, the Nyquist frequency is the maximum spatial frequency that can be effectively represented with the sample interval Δx or Δy. The Nyquist frequency in both the *x* and *y* directions are given by:

$$f_{nx} = \frac{1}{2\Delta x}, \qquad f_{ny} = \frac{1}{2\Delta y} \tag{3.46}$$

If the Shannon-Nyquist criterion in equation 3.45 above is not adhered to, it results in a sampling defect called *aliasing*. Aliasing is a condition where the undersampled high frequency components in the signal are interpreted in error as low frequency content.

Aliasing is known to be the main impairment to wave optics simulations which are based on the Discrete Fourier Transform. To avoid aliasing, the bandlimited waveform to be transformed needs to be sampled so finely that it satisfies the Nyquist sampling condition. The part of the analytical frequency spectrum that lies beyond the Nyquist frequency cannot be ignored as it can still introduce some erroneous aliased frequency content [50].

3.1.5.1 Effective Bandwidth

The Shannon-Nyquist sampling criteria earlier defined is only applicable for bandlimited functions. However, practical functions with finite support cannot be bandlimited which implies the Shannon-Nyquist criteria cannot be fully satisfied [62,63,64]. Though not bandlimited, these practical functions do still have their most significant frequency values enveloped in an *effective bandwidth*. Hence a small enough sample

interval can provide acceptable representation of the function with minimal aliasing effect.

This poses a problem to sampling as the *quadratic phase factor* or *chirp factor* inside the Fresnel integral is not bandlimited. The effective bandwidth can be described as the spectral radius that contains a high enough percentage of the total signal power in the whole spectrum. The total spectrum power in a 2-dimensional square signal, $f(x,y) = rect\left(\frac{x}{2w}\right) rect\left(\frac{y}{2w}\right)$ of half-width *w* is given by [50]:

$$P_{total} = \int_{-\infty}^{\infty} (4w^2)^2 sinc^2(2wf_x) sinc^2(2wf_y) df_x f_y \tag{3.47}$$

$$P_{total} = \int_{-\infty}^{\infty} rect^2\left(\frac{x}{2w}\right) rect^2\left(\frac{y}{2w}\right) \tag{3.48}$$

A typical effective bandwidth would contain up to 98% of the total power. If the total spectral power in equation 3.48 is converted to polar coordinates, the effective bandwidth is derived as:

$$B \approx \frac{5}{w} \tag{3.49}$$

When equation 3.49 is applied to the Shannon-Nyquist sampling rate requirement in equation 3.45, it can be deduced in equation 3.50 that the half-width of the *rect* function must have at least 10 samples across it, to retain effective bandwidth.

$$\Delta x \leq \frac{w}{10} \tag{3.50}$$

3.1.5.2 Sampling Constraints for the 2 forms of Fresnel Diffraction

As earlier mentioned, most practical sources produce non bandlimited waveforms. This poses a problem to sampling as the quadratic phase factor inside the Fresnel integral is not bandlimited. Based on Coy's [62] work, Schmidt [59] defined some geometric constraints based on Nyquist Criteria, which if satisfied, will avoid aliasing in the observation plane. These geometric constraints are:

$$\Delta x_2 \leq -\frac{D_2}{D_1}\Delta x_1 + \frac{\lambda z}{D_1} \tag{3.51}$$

$$L_2 \geq \frac{D_1 \Delta x_2 / \Delta x_1 + \lambda z / \Delta x_1 + D_2}{2} \tag{3.52}$$

$$N \geq \frac{D_1}{2\Delta x_1} + \frac{D_2}{2\Delta x_2} + \frac{\lambda z}{2\Delta x_1 \Delta x_2} \tag{3.53}$$

where N is the number of grid points required in the observation plane. The observation plane is at a distance z away from the source, Δx_1 is the source plane grid spacing and Δx_2 the observation plane grid spacing. D_1 and D_2 are the maximum spatial extent of the source and observation fields respectively. L_2 is the observation grid extent. However, satisfying the above geometric constraints in equation 3.51, 3.52 and 3.53 will not still guarantee accurate results. This is because the two forms of Fresnel approximation (Fresnel Integral and Angular Spectrum approaches defined in section 3.4.1.2) have different constraints and one needs to decide which one will suit the occasion. [65,66,67]. Although they are analytically identical, they produce different results to each other with sampled data.

3.1.5.2.1 Constraints for Transfer Function (TF) Approach or Fresnel Integral Method

For the one-step Fresnel Integral method of propagation, the observation plane grid spacing is fixed at $\Delta x_2 = {\lambda z}/{N\Delta x_1}$. This becomes a disadvantage for applications where the fixed Δx_2 does not effectively sample the observation plane field. In this situation, the only way out is to reduce Δx_2 by increasing the number of pixel points N but at the expense of increasing the execution time of the program which will inconveniently require high processing capacity of the computer. Applying the geometric constraints in equations 3.51 and 3.53 to the grid spacing, the number of grid points in the observation plane for the one-step propagation is given as:

$$N \geq \frac{D_1 \lambda z}{\Delta x_1(\lambda z - D_2 \Delta x_1)} \tag{3.54}$$

where $N = {L_1}/{\Delta x_1} = {L_2}/{\Delta x_2}$. L_1 and L_2 are the grid width of the source and observation square plane respectively. The equation 3.54 above is valid if $\lambda z > D_2 \Delta x_1$ and if $\lambda z \rightarrow D_2 \Delta x_1$.

The two step Fresnel Integral propagation method offers more flexibility in selecting the grid spacings for both observation and source planes. [62, 68]. Here, the source field U_1 is first propagated from the source plane to an intermediate plane at z_{1a} and then further propagated to the observation plane. The selection of the position of the intermediate plane is such that the desired grid spacings are obtained. More details can be found in Rydberg and Bengtsson [68].

To avoid aliasing and achieve an accurate result in the Fresnel Integral method, the quadratic phase factor inside the Fourier Transform has to be sampled finely enough to satisfy the Nyquist condition. If it is not sampled at a high enough rate, the intended high frequency content will show up erroneously in the low frequencies and this results in an undesirable situation where these low frequency components will be found on the observation plane region of interest. Jason Schmidt [69] proposed finding the maximum local spatial frequency of the quadratic phase factor in the Fourier Transform, and then sample at twice this rate. The local spatial frequency of the quadratic phase factor in the x_1 direction (of the Cartesian coordinate) is given as:

$$f_{locx} = \left(\frac{1}{z} + \frac{1}{R}\right)\frac{x_1}{\lambda} \tag{3.55}$$

This value is at its maximum at the edge of the grid where $x_1 = L_1/2$. For an apodized source field having non-zero values at the centre of the grid with maximum spatial extent D_1, the phase is included within this field. In this case, the maximum local spatial frequency value of the product of the source field and the quadratic phase factor will be at $x_1 = \pm D_1/2$. The R is the radius of a parabolic wavefront within D_1. After applying the Nyquist condition to equation 3.55 and some algebra, expressions are obtained for the minimum propagation distance to apply Fresnel Integral propagation, for a finite R:

$$z \geq \frac{D_1 \Delta x_1 R}{\lambda R - D_1 \Delta x_1} \tag{3.56}$$

and for an infinite R:

$$z \geq \frac{D_1 \Delta x_1}{\lambda} \tag{3.57}$$

3.1.5.2.2 Constraints for Impulse Response (IR) Approach or Angular Spectrum Method

Unlike the Fresnel Integral propagation, the observation plane grid spacing Δx_2 in the Angular Spectrum approach is variable. Hence, this method has its own requirement of avoiding aliasing of the quadratic phase factor. There are two basic conditions that must be satisfied to ensure the high frequency components do not corrupt the observation plane area of interest.

As with the Fresnel integral method, the maximum local spatial frequency is calculated for each of the two quadratic phase factors inside the Fourier Transform (including the inverse Fourier Transform) operations. Then the Nyquist condition is applied to ensure the spatial frequencies are not aliased [69]. The local spatial frequencies for the two phase factors are given as:

$$f_{loc1} = \frac{1}{\lambda}\left(\frac{1 - \Delta x_2/\Delta x_1}{z} + \frac{1}{R}\right)x_1 \tag{3.58}$$

and

$$f_{loc2} = \frac{\Delta x_1 \lambda z}{\Delta x_2} f_{1x} \tag{3.59}$$

These two local spatial frequencies are maximum at $x_1 = \pm D_1/2$ and $f_{1x} = \pm 1/(2\Delta x_1)$ respectively. Applying the Nyquist sampling criterion and carrying out some algebra yields, the following two sampling constraints are derived for the Angular Spectrum method:

$$\left(1 + \frac{z}{R}\right)\Delta x_1 - \frac{\lambda z}{D_1} \leq \Delta x_2 \leq \left(1 + \frac{z}{R}\right)\Delta x_1 + \frac{\lambda z}{D_1} \tag{3.60}$$

and

$$N \geq \frac{\lambda z}{\Delta x_1 \Delta x_2} \tag{3.61}$$

3.1.5.3 Summary of Sampling Regimes

3.1.5.3.1 Oversampling, Undersampling, Critical Sampling

Oversampling is a positive and desirable sampling situation that ensures aliasing is avoided for the Impulse Response (IR) or/and Transfer Function (TF) propagation regimes. In undersampling, the chirp function is not adequately sampled resulting in an aliased representation of its phase; undesirable display artifacts and/or periodic copies of the field. The oversampling and undersampling criteria for the TF and IR pair are opposite to each other. The condition where both the TF and IR are both adequately oversampled is called critical sampling, minimizing simulation artifacts, while allowing optimum use of the array side length and sampling bandwidth [67].

To define the sampling regimes for both the TF and IF propagation regimes based on reference 70, it starts with the *H* and *h* functions in equations 3.34 and 3.35, which are repeated here:

$$H(f_X, f_Y) = e^{jkz} exp\left[-j\lambda z\pi\left({f_X}^2 + {f_Y}^2\right)\right] \tag{3.62}$$

$$h(x, y) = \frac{e^{jkz}}{j\lambda z} exp\left[\frac{jk}{2z}(x^2 + y^2)\right] \tag{3.63}$$

Beam propagation simulation requires sampling the above propagator expressions, including the problematic sampling of the chirp complex exponential phase terms. Extracting their phase of their respective chirp terms yields:

$$\phi_H(f_X, f_Y) = -\pi\lambda z(f_X^2 + f_Y^2) \tag{3.64}$$

$$\phi_h(x, y) = \frac{k}{2z}(x^2 + y^2) \tag{3.65}$$

The constraint for a definite representation of the phase is that the maximum change in the absolute phase between any two adjacent samples must not be more than π. The mathematical expression for the constraint is given by:

$$\Delta f_x \left|\frac{\partial \phi_H}{\partial f_X}\right|_{max} \leq \pi \tag{3.66}$$

where the slope $\partial\phi_H/\partial f_X$=-$2\pi\lambda z f_X$. From this slope expression, since λ and z are fixed, the maximum slope will be obtained when f_X is at its maximum. Hence, maximum slope is:

$$\left|\frac{\partial \phi_H}{\partial f_X}\right|_{max} = -2\pi\lambda z f_{X(\max)} \tag{3.67}$$

Substituting the maximum slope back into equation 3.66 yields the sample interval criterion in the frequency domain for the TF propagation regime:

$$\Delta f_X \leq \frac{1}{2\lambda z\left|f_{X(max)}\right|} \tag{3.68}$$

Presenting some of the frequency domain terms in equation 3.68 above in the spatial domain; $\left|f_{X(max)}\right| = 1/2\Delta x$, $\Delta f_x = 1/L$, we obtain the following the criterion in the spatial domain as:

$$\Delta x \geq \frac{\lambda z}{L} \tag{3.69}$$

This means that when $\Delta x > \lambda z/L$, it is adequately sampled (oversampled). Here, the size limit of the field in the observation plane that can be accurately represented is derived from the windowed magnitude [48,70] to be approximately:

$$D_2 \leq D_1 + \frac{\lambda z}{\Delta x} \tag{3.70}$$

For a simple source function, a significant part of the of the field in the observation plane usually fits into the above-defined support size D_2 in equation 3.70.

For the IR propagation regime, applying a similar maximum slope term as equation 3.67, yields a sample interval criterion as:

$$\Delta x \leq \frac{\lambda z}{2|x_{max}|} \tag{3.71}$$

And since $|x_{max}|$ is typically equal to $L/2$, the sample interval criterion for the IR propagation regime becomes:

$$\Delta x \leq \frac{\lambda z}{L} \tag{3.72}$$

This implies that for oversampling in the IR propagation regime, equation 3.72 must be adhered to. Otherwise, it results in undersampling with aliasing. Although the critical sampling condition may seem like the most ideal option, it is not really the case as maintaining this condition is not convenient. This is because the critical sampling condition will entail too many or too few number of samples for a practical FFT. Another point where the critical sampling will be inconvenient is where one is modelling beam propagation through atmospheric turbulence where the turbulence phase screens most likely used would require a different set of sampling criteria which would not fit in with the critical sampling. Table 3.2 summarises the propagation regimes and their respective sampling interval criteria, as well as which situation results in undersampling or oversampling.

Table 3.2: Sampling regimes and criteria.

Regime	**Chirp Sampling**	**Source Bandwidth Requirement**	**Comments**
$\Delta x < \frac{\lambda z}{L}$	*IR* is oversampled *TF* is undersampled	$B_1 \leq \frac{L}{2\lambda z}$	Also called the long distance regime. Due to source bandwidth limitation, there is an aliasing effect when TF is sampled resulting in artifacts. The IF approach produces smoother results, though not always accurate.
$\Delta x > \frac{\lambda z}{L}$	*IR* is undersampled (periodic copies). *TF* is oversampled	$B_1 \leq \frac{1}{2\Delta x}$	Also called the short distance regime. Here, the observation plane size is limited. TF produces good results and IR produces aliased, periodic copies of the field at the observation plane.
$\Delta x = \frac{\lambda z}{L}$	Critical sampling for both *IR* and *TF*	$B_1 \leq \frac{1}{2\Delta x}$ or $B_1 \leq \frac{L}{2\lambda z}$	Full source bandwidth and observation plane size are available. *H* and *h* are both adequately sampled.

3.1.5.3.2 Design Steps for Propagation Simulation

When simulating beam propagation, the following design steps should be considered [52].

Step 1: Ensure that the source support is at most 2 or 3 times less than the array side length.

Step 2: Work out the Sampling regime; find out the corresponding propagator that would suit.

Step 3: Consider the source bandwidth criteria.

Step 4: Observe the results and bandwidth, then reconsider source sampling.

3.2 Atmospheric Turbulence

As a result of differential heating and cooling of the earth by sunlight and diurnal cycles, the temperature of the atmosphere is known to fluctuate randomly. This results in random changes in wind velocity (as air moves, it transitions from a more uniform pattern called Laminar flow to Turbulent flow, where the velocity field is no longer uniform). The turbulent velocity field acquires randomly distributed pockets of air called *eddies* which fluctuate in size and temperature causing corresponding variations in the refractive index. These changes in refractive index act like lenses (of the size of the eddy that caused it) in the atmosphere to focus and redirect the wavefront of incident beam causing intensity variations. When the refractive index variations accumulate, it can distort the wavefront of a beam propagating through the atmosphere [71,72].

3.2.1 The Structure of Atmospheric Turbulence

The history of the study of turbulences began with its recognition as a distinct phenomenon by da Vinci in the 19th century. Due to the complexity of the atmosphere, the concept of predicting atmospheric turbulence is not based on deterministic prediction but based on statistical analysis. Turbulent flow is a nonlinear phenomenon known to be governed by Navier- Stokes equations. Due to the complexity of solving the Navier- Stokes equations for fully developed turbulence, Kolmogorov [73, 74] proposed statistical approximations of the [Navier-Stokes] equations. His theory is among the most widely accepted and most consistent with experimental observations. He submitted that the kinetic energy in large eddies is transferred into smaller eddies, in turbulent flow. The average size of the largest eddies is called the *outer scale* L_0 and that of the smallest eddies is called *inner scaler* l_0. The outer scale is the size above

which isotropic behaviour is violated and the inner scale is the size below which viscous effects are important [72]. The average size of the inner scale l_0 can be a few millimetres near the ground to a few centimetres high above the ground. The outer scale L_0 near the ground is on the order of the height above the ground, and up to tens to hundreds of metres high above the ground [75].The interval of eddy sizes between L_0 and l_0 is called the *inertial subrange*.

In his analysis, Kolmogorov used the structure function instead of the more common co-variance. This is because he made the assumption that eddies within the inertial subrange are statistically isotropic and homogenous within small areas of space, and this implies that their velocity and refractive index will not be incrementing with those areas of space. Another assumption made is that the atmospheric turbulence is incompressible. Based on these three assumptions, the structure tensor [72,76,77] D_{ij} between any two points in space separated by vector **r**:

$$D_{ij} = \langle [v_i(\mathbf{r_i} + \mathbf{r}) - v_i(\mathbf{r_1})] \left[v_j(\mathbf{r_1} + \mathbf{r}) - v_j(\mathbf{r_1})\right] \rangle \tag{3.73}$$

is reduced to the following structure function, for the sake of simplicity:

$$D_v = \langle [v_r(\mathbf{r_1} + \mathbf{r}) - v_r(\mathbf{r_1})]^2 \rangle \tag{3.74}$$

The brackets represent an ensemble average and the v_i and v_j are the velocity components. If we consider a case where the separation r is small and within the inertial sub-range of turbulence ($l_0 < r < L_0$), the structure function becomes:

$$D_v = {C_v}^2 r^{2/3} \tag{3.75}$$

where $C_v^{\,2}$ is the velocity structure constant which is a measure of the energy in the turbulence.

The velocity structure function has also been related to the refractive index, called the *Kolmogorov's Sub-range Expression* and is given as [78, 79]:

$$D_n(r) = C_n^2\, r^{2/3} \text{ for } l_o \ll r \ll L_o \tag{3.76}$$

where $C_n^{\,2}$ = refractive index structure constant, which is a measure of the strength of turbulence.

3.2.2 Power Spectral Density of Refractive Index

It is assumed that the atmosphere is made up of two parts of refractive index: a mean refractive index $\langle n(\mathbf{r})\rangle$ and a fluctuating refractive index part $n_1(\mathbf{r})$. The covariance of the refractive index field B_n will be [72]:

$$B_n = \langle n_1(\mathbf{r} + \mathbf{r_1}) n_1(\mathbf{r_1})\rangle \tag{3.77}$$

The Fourier transform of the covariance is known to give Power Spectral Density (PSD). Hence, the power spectral density of the above covariance of refractive index is given by:

$$\Phi_n(\mathbf{K}) = \frac{1}{(2\pi)^3}\int d^3 r B_n(r) e^{-i\mathbf{K}\,.\,\mathbf{r}} \tag{3.78}$$

where **K** is the three-dimensional wave number. If we change the coordinates of the Kolmogorov's subrange expression to spherical terms **K** = (K,θ, ϕ) and carrying out the ensemble averaging, the power spectral density becomes [80]:

$$\Phi_n(K) = \frac{5}{18\pi} {C_n}^2 K^{-3} \int_{l_o}^{L_o} dr \sin(Kr) r^{-1/3} \tag{3.79}$$

Furthermore, if limits of integration diverges to 0 to infinity ($l_o \to 0, \text{and } L_o \to \infty$), the integral reduces to the *Kolmogorov Spectrum* given by:

$$\Phi_n^K(K) = 0.033 {C_n}^2 K^{-11/3} \text{ for } \frac{1}{L_0} \ll K \ll \frac{1}{l_0} \tag{3.80}$$

The equation 3.80 above is only valid for random fields that are homogenous and isotropic locally. According to Tatarskii [81], a spectrum useful for cases of finite inner scale is as follows:

$$\Phi_n^T(K) = 0.033 {C_n}^2 K^{-11/3} \exp\left(\frac{-\mathrm{K}^2}{(5.92/l_\mathrm{o})^2}\right) \tag{3.81}$$

For cases with finite outer scales, the *von Karman Spectrum* and the *modified von Karman* power spectral density will be useful and they are defined respectively as [82]:

$$\Phi_n^{vK}(K) = \frac{0.033 C_n^2}{(K^2 + K_0^2)^{11/6}} \text{ for } 0 \le K \ll \frac{1}{l_0} \tag{3.82}$$

$$\Phi_n^{mvK}(K) = 0.033 C_n^2 \frac{\exp(-K^2/K_m^2)}{(K^2 + K_0^2)^{11/6}} \text{ for } 0 \le K < \infty \tag{3.83}$$

where $K_0 = 2\pi/L_0$ and $K_m = 5.92/l_0$ and their values are chosen to match the small scale and large scale behaviour predicted by the dimensional analysis [71]. Amongst all the power spectral density models, the modified von Karman is the simplest that includes the effects of both inner and outer scales [83].

3.2.3 Strength of Turbulence, C_n^2

The strength of Atmospheric Turbulence which is characterised by the refractive index structure constant, C_n^2 in $m^{-2/3}$. C_n^2 is not a constant as it sounds but it is a variable entity by all means. Several experiments have been carried out over the years to confirm that C_n^2 changes with time of the day [84], location [85] as well as with altitude [86].

3.2.3.1 Variation with Altitude

Based on altitude, C_n^2 is prevalent in the lower atmosphere due to more fluctuations in refractive index of air and it diminishes with altitude. Typical values of C_n^2 ranges from 10^{-13} to 10^{-18} $m^{-2/3}$, with weak turbulence falling within the range $C_n^2 \leq 10^{-17}$, moderate turbulence $10^{-17} \leq C_n^2 \leq 10^{-14}$ and strong turbulence $C_n^2 \geq 10^{-14}$ [87]. Hufnagel [88] was one of the first to make experimental observations on the variation of C_n^2 with height in meters above the ground, h. He suggested that:

$$C_n^2(h) = \left\{\left[(2.2 \times 10^{-53})h^{10}\left(\frac{W}{27}\right)^2\right]e^{-h/1000} + 10^{-16}e^{-h/1500}\right\}\exp[r(h,t)] \quad (3.84)$$

where the $r(h,t)$ is a zero mean homogenous Gaussian random variable and W is the wind correlating factor given as

$$W = \left[\frac{1}{15000m}\int_{5000m}^{20000m} v^2(h)dh\right]^{0.5} \tag{3.85}$$

and $v(h)$ is the wind speed at height *h*. G. C. Valley [89], in his work on anisoplanatism, made a slight alteration to the Hufnagel model. The Hufnagel-Valley model, which is one of the most widely accepted models, was put together by P. B. Ulrich [90] by adding a term to account for the boundary layer. The Hufnagel-Valley model is given by:

$$C_n{}^2(h) = 5.94 \times 10^{-53}(v_u/27)^2 h^{10} e^{(-h/1000)} + 2.7 \times 10^{-16} e^{(-h/1500)} + Ae^{(-h/100)} \tag{3.86}$$

where v_u is the high altitude wind speed typically about 21 m/s and A is a variable usually 1.7×10^{-14} $m^{-2/3}$. The inclusion of these two additional variables is one of the advantages of the Hufnagel-Valley model compared to others. However, its limitation is the ground level term as it does not compare well with real life measurements made from ground up to about 1 km. Walter and Kunkel [91] observed a decrease in near ground measurements of $C_n{}^2$ with height characterised by $h^{-4/3}$. From this, L. C. Andrews *et al* [14] proposed an alteration to the Hufnagel-Valley model that includes the $h^{-4/3}$ near-ground term. This model, which also accounts for the time of the day *p*, is called the *Hufnagel-Andrews-Philips (HAP)* model given as:

$$C_n^2(h) = M\left[0.00594\left(\frac{v_u}{27}\right)^2\left(\frac{h+h_s}{10^5}\right)^{10}\exp\left(-\frac{h+h_s}{1000}\right) + 2.7 \times 10^{-16}\exp\left(-\frac{h+h_s}{1500}\right)\right] + C_n^2(h_0)\left({}^{h_0}/_{h}\right)^p, h > h_0 \tag{3.87}$$

The h_0 is the height of the measuring instrumentation above the ground and h_s is the height of the ground platform above sea level. The $C_n^2(h_0)$ is the refractive index structure constant at h_0. The factor M (mostly> 5) is a scaling factor that describes the average value of the level of random background turbulence and can be adapted to fit the measured conditions at various locations.

3.2.3.2 Variation with time of the Day

The parameter p in the last term of the Hufnagel-Andrews-Philips model in equation 3.87 is dependent on the hour of the day that the measurements are taken. Hence, C_n^2 varies with time of the day. To measure the p parameter, the local time, the Sunrise and Sunset times should be known. The p was calculated to be 4/3 for the day time and 2/3 at night, sunrise or sunset. Details of how this was worked out can be found in reference 20 and 92.

3.2.3.3 Variation with location

The refractive index structure function C_n^2 also varies with location as the atmosphere over a coastal location will not have the same attributes as that over inland locations, or a desert. This is because the different locations will have different temperatures and wind speed resulting in different values for C_n^2. Several authors have done experiments to measure C_n^2 and the locations are clearly specified [85,93,94,95].

3.2.4 Coherence parameter, r_0 and Phase Power Spectral Density

C_n^2 is commonly used to compute other more useful parameters that are also measurable, like the atmospheric *coherence diameter* or *coherence parameter* or *Fried parameter*, r_0. Coherence Diameter was first proposed by D. L. Fried [96] hence it's popular name Fried parameter. It can be defined as a degree of the quality of the optical propagation through the atmosphere due to inhomogeneity and inconsistency in the refractive index of the atmosphere. In other words, the coherence parameter can be seen as the diameter of a circular area over which the rms aberration of a wavefront due to its propagation through the atmosphere, is equal to 1 radian.

The Fried parameter is related to the variable C_n^2 for a plane wave source with receiver h distance away, as follows:

$$r_{0,pw} = \left[0.423k^2 \int_0^h {C_n}^2(h)dh\right]^{-3/5} \tag{3.88}$$

For spherical wave point source, the Fried parameter is given as:

$$r_{0,sw} = \left[0.423k^2 \int_0^h {C_n}^2(h)\left(\frac{\Delta h}{h}\right)^{5/3} dh\right]^{-3/5} \tag{3.89}$$

Typical values for Fried parameter r_0 for visible wavelengths is known to be about 5 to 10 cm. Since r_0 incorporates C_n^2, propagation distance and wavelength in one expression, it is more widely used to characterise atmospheric phenomena [72].

The refractive index Power Spectral Densities defined in section 3.22 in terms of C_n^2 can now be redefined in terms of r_0. But before this, the phase Power Spectral Density $\Phi_\phi(K)$, which is the form that will be needed in generating phase screens subsequently, can be defined in terms of the refractive index Power spectral density $\Phi_n(K)$ for a plane wave as [71]:

$$\Phi_\phi(K) = 2\pi^2 k^2 \Delta z \Phi_n(K) \tag{3.90}$$

Hence the phase Power Spectral Densities for the Kolmogorov, von Karman PSD and the modified von Karman's models are as follows:

$$\Phi_\emptyset{}^k = 0.49 {r_0}^{-5/3} k^{-11/3} \tag{3.91}$$

$$\Phi_\emptyset{}^{vk} = \frac{0.49 {r_0}^{-5/3}}{(k^2 + {k_0}^2)^{11/6}} \tag{3.92}$$

$$\Phi_\emptyset{}^{mvk} = 0.49 {r_0}^{-5/3} \frac{\exp(-k^2/{k_m}^2)}{(k^2 + {k_0}^2)^{11/6}} \tag{3.93}$$

3.2.5 Optical propagation through turbulence

As earlier mentioned, the wave equation derived in section 3.1.2 describes the propagation of light signal both in a vacuum. This can also be used to describe the additional effect of atmospheric turbulence present in the medium. Jason Schmidt [71] as well as Andrews and Philips [83] derived this starting from wave equation for the electric field given as:

$$\nabla^2 \mathbf{E}(\mathbf{r}) + k^2 n^2(\mathbf{r}) + 2\nabla[\mathbf{E}(\mathbf{r}).\nabla \mathrm{In}\, n(\mathbf{r})] = 0 \tag{3.94}$$

The term $2\nabla[\mathbf{E}(\mathbf{r}).\nabla \mathrm{In}\, n(\mathbf{r})]$ stands for the change in polarisation of the wave as it propagates. However when the wavelength is smaller than the inner scale ($\lambda < l_0$), the wave equation is simplified to:

$$[\nabla^2 + k^2 n^2(\mathbf{r})]\mathbf{E}(\mathbf{r}) = 0 \tag{3.95}$$

where **E** is the electric field vector and *k* is the vacuum wavenumber, *n* is the refractive index. Since magnetic induction **B** also has the same relationship, the equation can be presented in a general form to cover all field components:

$$[\nabla^2 + k^2 n^2(\mathbf{r})]U(\mathbf{r}) = 0 \tag{3.96}$$

The refractive index in equation 3.96 above is position-dependent, and that is what makes it different from equation 3.22. To solve the equation 3.96, we assume a weak fluctuation condition which means that equation 3.77 becomes

$$n^2(\mathbf{r}) \cong 1 + 2n_1(\mathbf{r}) \tag{3.97}$$

When this is substituted into the wave equation in equation 3.96, it becomes:

$$\{\nabla^2 + k^2[1 + 2n_1(\mathbf{r})]\}U(\mathbf{r}) = 0 \tag{3.98}$$

This equation is solved by Fourier optics when the refractive index in the medium is constant. But the atmosphere is typically not homogenous and the refractive index is not constant. Hence the Fourier optics method is used along with some perturbative

methods to derive approximate solutions. The vacuum solution $U_0(\mathbf{r})$ to the equation 3.98 is one of the parameters of the optical field $U(\mathbf{r})$ in the Rytov [97] method given by:

$$U(\mathbf{r}) = U_0(\mathbf{r})\exp[\psi(\mathbf{r})] \tag{3.99}$$

The $\psi(\mathbf{r})$ is the complex phase perturbation. When the amplitude and phase quantities are isolated, it is written as:

$$\psi = \chi + i\phi \tag{3.100}$$

where χ is the log-amplitude perturbation and ϕ is the phase perturbation induced by the turbulence. More details of these two quantities are discussed in the section 3.2.6.

3.2.6 Propagation Defects of turbulence

When an optical beam is propagated through atmospheric turbulence, there are three categories of propagation defects known to happen to the beam namely beam wander, beam spreading and intensity fluctuations. The intensity variations, usually expressed as the log-amplitude fluctuations, are caused by eddies with the size on the order of $(\lambda L)^{1/2}$. The eddies that are large compared with the beam radius tend to deflect the beam; this is called Beam Wander. The eddies that are small compared with the beam radius do not deflect the beam much but tend to broaden the beam; this is called Beam spread [80]. The details of these defects come in the next three subsections.

3.2.6.1 Intensity Variation

An optical beam propagating through atmospheric turbulence, even over short paths, will definitely experience intensity fluctuations. All experimental and theoretical research on intensity fluctuations usually centres around the normalised variance of the intensity fluctuations, called *Scintillation index* and is defined by [98]:

$$\sigma_{\chi}^{2} = \frac{\langle I^{2} \rangle - \langle I \rangle^{2}}{\langle I \rangle^{2}} = \frac{\langle I^{2} \rangle}{\langle I \rangle^{2}} - 1 \tag{3.101}$$

where the angle brackets $\langle \quad \rangle$ denotes ensemble average, I is the intensity of the optical beam. The Scintillation index is dimensionless. Scintillation levels are divided into three categories [99], depending on the scintillation index: the weak intensity-fluctuation regime with ${\sigma_{\chi}}^{2} < 0.3$, the medium regime with $0.3 \leq \sigma_{\chi}^{2} < 5$ and the strong fluctuations or saturation regime with $\sigma_{\chi}^{2} \geq 5$. In the weak fluctuations regime, the scintillation index of an unbounded plane wave based on the Kolmogorov spectrum is called the *Rytov variance* given by: [72,79,97]:

$${\sigma_{\chi}}^{2} = 1.23 k^{7/6} L^{11/6} {C_{n}}^{2} \tag{3.102}$$

while the log-amplitude fluctuation variance for a spherical wave is:

$${\sigma_{\chi}}^{2} = 0.124 k^{7/6} L^{11/6} {C_{n}}^{2} \tag{3.103}$$

The above two log-amplitude fluctuation expressions in equations 3.102 and 3.103 were derived from perturbation theory hence they break down for long paths and strong turbulence. Since eddies are considered to act as lenses, the focal length of an eddy of diameter l will be $f \cong l/\Delta n$, where Δn is the difference in refractive index. In the

geometric optical domain (where $l > \sqrt{\lambda L}$ and $l_o < \sqrt{\lambda L}$), Clifford [100] expresses the log-amplitude variance as:

$$\sigma_\chi{}^2 \sim k^{7/6} L^{11/6} C_n{}^2 \tag{3.104}$$

where L is the propagation path length.

More authors [101, 102] have conducted experiments to measure Scintillation index, verifying that experimental results deviate from these theoretical predictions, as well as that the Scintillation index near the diffractive end of the collimated beam was considerably larger than the on-axis values. Optical scintillation can be reduced by *aperture averaging* [103]; increasing the collecting area of the receiver lens by the integral of all the components of the incident intensity on a particular part of the lens [104].

3.2.6.2 Phase Variation

Random variation in phase causes waveform distortion as mentioned earlier. These phase variations, mostly measured with an interferometer, is as a result of the refractive index being a random function of space and time. In practice, the distortion caused by intensity variations is small compared to that caused by phase variations [105]. When two parallel optical wave paths separated by a distance ρ propagate through space, the phase difference $\delta\phi$ between them is given by [72]:

$$\delta\phi \cong k\rho[\Delta n(\rho)] \tag{3.105}$$

In their study, Clifford [106] *et al* defined the phase structure function as:

$$D_\phi = \langle [\phi(\mathbf{r}+\rho) - \phi(\mathbf{r})]^2 \rangle \tag{3.106}$$

Again here, the angle brackets indicate ensemble average. The phase structure function is necessary for defining the phase coherence. After averaging over many statistical realizations, Tatarskii [79] defines phase structure function for plane waves as:

$$D_\phi(\rho) = 2.91k^2 L C_n^2 \rho^{5/3}, \text{for } \sqrt{\lambda L} \leq \rho < L_0 \tag{3.107}$$

and that for spherical waves as:

$$D_\phi(\rho) = 1.09k^2 L C_n^2 \rho^{5/3}, \text{for } \sqrt{\lambda L} \leq \rho < L_0 \tag{3.108}$$

The wave is most likely to lose coherence when it is propagated over long paths and over many eddies. The beam becomes coherent only if the phase difference $\langle (\delta\phi)^2 \rangle < \pi^2$. Substituting this condition for coherence into equation 3.107 above, the *coherent distance* ρ_o (largest eddy for which a plane is considered coherent) is obtained as [72]:

$$\rho_o = \left[\frac{\pi^2}{k^2 {C_n}^2 L} \right]^{3/5} \tag{3.109}$$

Hence, when two optical beams or two parts of the same beam propagate through the same distance *L* of atmospheric turbulence, though they may arrive at the same point, they arrive using a slightly different path and have different *angles of arrival*. Kon and Tatarskii [107] defines the variance of their angle of arrival difference as

$$\langle \alpha^2 \rangle = \frac{D_\phi}{k^2 \rho^2} \tag{3.110}$$

where the D_ϕ is the phase structure function for plane waves. For an aperture of diameter *D*, the angle of arrival variance becomes:

$$\langle \alpha^2 \rangle = 2.91 C_n^2 L D^{-1/3} \tag{3.111}$$

This variance in angle of arrival in equation 3.111 above is the quantity that measures *Beam Wander*: a random displacement of the received beam's focal spot from the centroid coordinate.

3.2.6.3 Beam Spread for Coherent Beam

Optical beams are known to spread out as they propagate, even without the additional effect of turbulence. This is primary as result of diffraction, resulting in the beam radius gradually increasing and the beam energy gradually weakening as it propagates. This effect was discussed in section 2.1. The beam spread is also made more severe with the additional effect of atmospheric turbulence. The constraint for coherence distance in equation 3.109 can be used to define the total beam spread as well. In an ideal case of constant turbulence ${C_n}^2$ regardless of altitude, the angular spread θ for a collimated uniform beam of radius ω in uniform turbulence is given by [108]:

$$\theta^2 \cong \frac{1}{k^2 \omega^2} + \frac{1}{k^2 {\rho_o}^2} \tag{3.112}$$

For a typical Gaussian beam whose intensity profile is defined by the function below (same as equation 2.9), with an initial beam waist diameter w_o:

$$I = \frac{{w_o}^2}{{w_b}^2} \exp\left(-\frac{2\rho^2}{{w_p}^2}\right) \tag{3.113}$$

When the Gaussian beam is propagated for long distances ($z \gg \pi {w_o}^2/\lambda$), the beam waist will spread to:

$$ {w_b}^2 = \frac{4z^2}{k^2 {w_o}^2} + 3.58 {C_n}^2 L^3 {w_o}^{-1/3} \tag{3.114} $$

When propagated for a short distance ($z \ll \pi {w_o}^2/\lambda$), the waist becomes:

$$ {w_b}^2 = {w_o}^2 + 2.86 {C_n}^2 k^{1/3} L^{8/3} {w_o}^{1/3} \tag{3.115} $$

3.2.7 Turbulence Phase Screen

It is important to be able to model properly the random turbulence in the lower atmosphere, in order to have an accurate FSO propagation simulation. For the purpose of simplification of analytical calculations and computer simulations, the technique commonly used to model atmospheric turbulence is to consider it as a finite number of discrete layers [109,110]. Each of the layers is a thin (its thickness is much less than the propagation distance that follows [111]) *phase screen* used to represent a much thicker volume of turbulence. In theory, the turbulence profile in the *ith* phase screens is in terms of the effective strength of turbulence $C_{n_i}^2$, the thickness of the turbulence Δz_i and the location of the phase screen along the propagation path z_i [71]. The phase screens are imaginarily placed at intervals through the lower atmosphere. The common process of propagation through turbulence phase screens is the *Split-step* beam propagation method [112,113].

Over the years, different methods have been used to model the phase screens like the Zernike polynomial method [114], covariance method [115], Discrete Fourier Transform method [116]. Although these different methods do have their own pros and cons, the

Fourier Transform method is most commonly used because of its computational efficiency. Its major drawback is inaccuracy due to the undersampling of the low spatial frequency, where most of the power reside. Several methods have been proposed to compensate for these deficient low frequency components, one of them is called the Subharmonic method [117,118]. The Subharmonic method was later validated to be accurate by Frehlich [119].

Phase screens are created by transforming random numbers generated on the computer into 2D arrays of phase values on a grid of sample points having the same statistical properties as the turbulence-induced phase variations [71]. For a finite square grid, the Fourier Transform-based phase screen is generated using the expression below [119, 120]:

$$\emptyset(x,y) = \sum_{n=-\infty}^{\infty} \sum_{m=-\infty}^{\infty} [R(N) + \mathrm{i}R(N)] \times \sqrt{\Phi_\phi} \times \exp[i2\pi(f_{x_n}x + f_{y_m}y)] \qquad (3.116)$$

where *R* represents Gaussian random numbers with zero mean and unit variance. *N* is the number of grid points per side of the screen, $f_{x_n}$and f_{y_m} are the discrete spatial frequencies in the *x* and *y* directions. As earlier stated, the phase screen generated from equation 3.116 above is deficient in the low spatial frequencies and this is augmented using the method proposed by Lane *et al* [117]. Also from equation 3.116 above, Φ_ϕ is the phase Power Spectral Density (PSD) of turbulence. This term characterises the turbulence and it is based on refractive index variations. Different phase PSD models have been defined earlier in section 3.2.4.

To supplement the low frequency components in the Fourier transform method, a low frequency screen is generated as a sum of N_p different screens given by [71,117]:

$$\emptyset_{lf}(x,y) = \sum_{p=1}^{N_p} \sum_{n=-1}^{1} \sum_{m=-1}^{1} C_{n,m} \exp[i2\pi(f_{x_n}x + f_{y_m}y)] \tag{3.117}$$

where *n* and *m* are discrete frequencies and each *p* represents the different grids. The $C_{n,m}$ are the random draws of the Fourier series coefficients.

3.2.8 Split-Step Propagation method

The method commonly used for optical beam propagation through atmospheric turbulence is the split-step propagation method. This method, which was first introduced by Tappert and Hardin [121], is a pseudo-spectral method that entails logically breaking the propagation path length into equal intervals, say Δz. The main advantage of this method, compared to other methods which are mostly time-domain finite difference methods, is speed and ease of implementation. The first step in this split-step method is to make an axial advance, propagating the initial beam forward by Δz using one of the propagators defined in section 3.1.4. Then the phase screen is applied in the coordinate space before another axial advance of Δz is made using the propagator. This continues until the whole propagation path length is covered. It should be noted that the phase screens do not need to be applied at every axial advance made and the interval between applications of the phase screens is expected to satisfy the condition [12]:

$$L_0 \ll \Delta z \ll L_d \tag{3.117}$$

where L_d is the diffraction length or Rayleigh length.

3.3 Chapter Summary

In this chapter, we discussed the fundamental theory behind the propagation of the Gaussian and Bessel beams through atmospheric turbulence. In the first section of the chapter, we did a thorough literature review of Fourier Optics, treating the Maxwell's equations and deriving the wave equations as well as the Helmholtz equation. We went on to discuss the Fourier Analysis, looking at the definitions of both the analytical and the Discrete Fourier Transforms as well as the Fourier transform theorems. We reviewed the Scalar Diffraction theory: the Huygens-Fresnel Principle, the Fresnel and Fraunhofer diffraction approximations. Then we did a detailed discussion of the sampling theory, covering the sampling regimes and criteria. The second section of the chapter covers the theory of atmospheric turbulence, encapsulating the structure of turbulence, the power spectral density of refractive index, the strength of turbulence, the coherence (Fried) parameter, propagation defects of turbulence, the theory of turbulence phase screens and Split-step propagation method which will be the method that will be adopted in the beam propagation in chapters 5 and 6.

CHAPTER 4

4.0 MODELLING THE BEAMS AND THE ATMOSPHERIC TURBULENCE

This chapter describes our model for creating the Gaussian beam and Bessel beam, which will be utilised in chapter 5 and 6. Here we model the power contained in the beams. This will include deriving the minimum radii for the both beams, with their respective altitudes, to ensure that not more than 50% of the initial beam power is lost before it arrives at the receiver. The second section of this chapter will encapsulate the modelling of the atmospheric turbulence as well as deriving the maximum height beyond which the effect of turbulence is negligible.

4.1 Gaussian Beam Model

Many lasers available in the market produce beams that approximate a Gaussian profile, a radially symmetrical distribution. In this section, we model the Gaussian beam that will be propagated in chapter 5. A few mathematical system models will be derived to help define the beam model. We also look at the power contained in the Gaussian beam we are creating.

4.1.1 Creating the Gaussian Beam

The general form of the Gaussian beam is given in equation 4.1 below, similar to the earlier defined equation 2.8, it is implemented in Matlab.

$$U_g = \mathrm{A}\exp\left(\frac{-r^2}{{\omega_0}^2}\right) \tag{4.1}$$

where *A* is 1 *V/m*, *r* the radial distance from the centre of the beam and ω_0 the beam waist radius or spotsize. The ω_0 is confined into a mask aperture of selected size. The selected size of the aperture *D* is such that it is much less than the array side length *L*. This is one of the sampling criteria ($D < 2L$) discussed in section 3.15, to help reduce artifacts at the edge of the observation plane after propagation of the beam, due to the periodic extension properties of the Fast Fourier Transform. For example, the figure 4.1 below shows an intensity profile of a Gaussian beam confined to a 0.2m mask aperture on an array of 8m x 8m. Notice the sharp discontinuation of the Gaussian profile by the aperture mask.

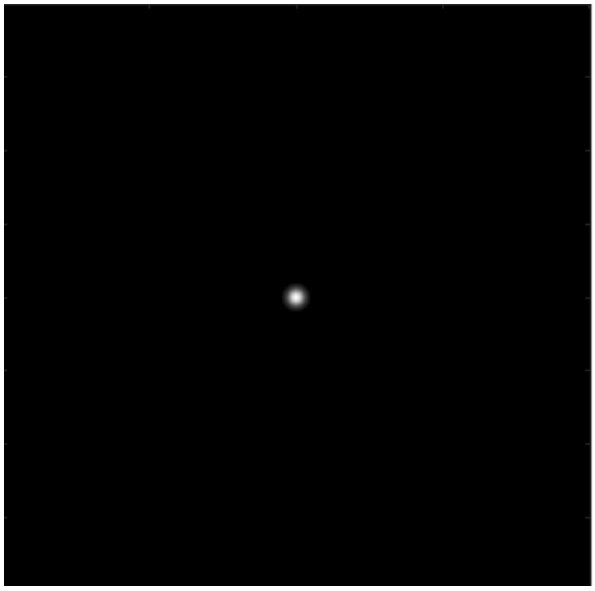

Figure 4.1: Apertured Gaussian Beam

4.1.2 Power contained in the Gaussian Beam

The total power contained in a transmitted Gaussian beam of aperture radius, *r* at a distance *z* from source has earlier been defined in equation 4.2 and is repeated below:

$$P = P_0\left(1 - \exp\left(-2r^2/_{w(z)^2}\right)\right) \tag{4.2}$$

where $P_0 = \pi I_0 w_0^2/2$ is the initial or total beam power at a beam radius w_0 and I_0 is the peak intensity. Typically for a Gaussian beam transmitting through an aperture radius *r* equal to the initial beam radius w_0 (i.e. at z=0), 86.5% of its total power will be transmitted according to equation 2.12. See section 2.12 for more details. To ensure that 99% of the initial beam power is transmitted, a transmitter aperture radius *r* of $1.5174w_0$ is required. This condition was satisfied to ensure that the beam in figure 4.1 had 99% of the energy passing through the aperture. If the receiver telescope also has aperture radius equal to $1.5174w_0$, 50% of the initial beam power will be lost at the receiver when the received beam waist radius is:

$$w(z) = 2.5775w_0 \tag{4.3}$$

and the distance that would be travelled for 50% of the initial power to be lost is given by:

$$z_{0.5P} = 1.2560\frac{\pi w_0^2}{\lambda} \tag{4.4}$$

From equation 4.4, the corresponding minimum initial beam wait radius required for 50% of the initial power to be lost (when 99% was transmitted) can be derived as:

$$w_{0.5P} = 1.5174\sqrt{\frac{z\lambda}{1.2560\pi}} \tag{4.5}$$

The table 4.1 below shows a list of useful propagation targets for ground-to-space Gaussian beam propagation. Here, it is assumed that the transmitter and receiver telescopes both have the same aperture radius.

Table 4.1: Useful propagation targets I

Propagation Target	**Altitude (km)**	**Beam radius ($W_{0.5P}$)**
An A320 Aircraft ceiling	12	59mm
Higher Altitude Aircrafts	27	89mm
International Space Station (ISS)	340	315mm
Low Earth Orbit (LEO) Satellite	700	452mm
Global Position System (GPS) Satellite	20,350	2.44m
Geostationary Orbit (GEO) Satellite	35786	3.23m

The beam radius in the third column is gotten by implementing equation 4.5. It can be observed that the higher the target altitude, the larger the size of the telescopes required to ensure that not more 50% of the initial power is lost in transit due to diffraction.

4.2 Bessel Beam Model

Here, we model the non-diffracting Bessel beam, creating the beam numerically and defining a few conditions to ensure not more than half of its initial power is lost in transit, before getting to the receiver.

4.2.1 Creating the Bessel Beam

A zero-order Bessel beam is generated analytically by implementing the expression for the *n*th order Bessel beam in equation 2.24, repeated in equation 4.6 below for reference:

$$E(r, \phi, z) = A_0 \exp(ik_z z) J_0 (k_r r) \exp(\pm in\phi) \tag{4.6}$$

A Bessel beam is known to be ideal and in order to be generated, it has to be truncated into an aperture function. The radial wave vector k_r was derived in equation 2.28 as:

$$k_r = \frac{2.405}{B_w} \tag{4.7}$$

where B_w is the radius of the circular aperture function placed on the beam. Like the Gaussian beam, the size of the aperture *D* is also much less than the array side length *L* to help reduce artifacts at the edge of the observation plane after propagation of the beam. The k_r is chosen such that the aperture B_w is equal to the size of the Bessel beam's central core (its first zero), trimming off the outer rings, which would have reflected off the walls of the observation grid and distort the beam. And since the Gaussian beam generated in section 4.1.1 is also masked by an aperture function w_0, which is set to be equal to B_w, this ensures a fair basis of comparing the two beams as proposed by Durnin in his comparison of these two beams. The ϕ is the argument of the radial distance, *r* from the centre of the beam.

Another implication of trimming off the outer rings of the Bessel beam is a severe loss in the beam energy as a significant part of the Bessel beam energy is carried in the outer rings. Another effect of having to truncate the Bessel beam is that its non-diffracting properties are only valid with the distance Z_{max} defined in equation 2.25, and rewritten as:

$$Z_{max} = \frac{B_w}{tan\theta};\ \text{for}\ \theta = \arctan(\frac{k_r}{k_z}) \tag{4.8}$$

where θ is the cone angle earlier defined in equation 2.26 and 2.27. In our modelling of the beam, we derived a very small cone angle of 0.000055° to ensure a very large Z_{max} of 209,004m. For an aperture mask size B_w of 0.2m, the intensity profile of the initial Bessel beam is as shown in figure 4.2. Notice that the outer rings have been trimmed off and the central core fills up the aperture.

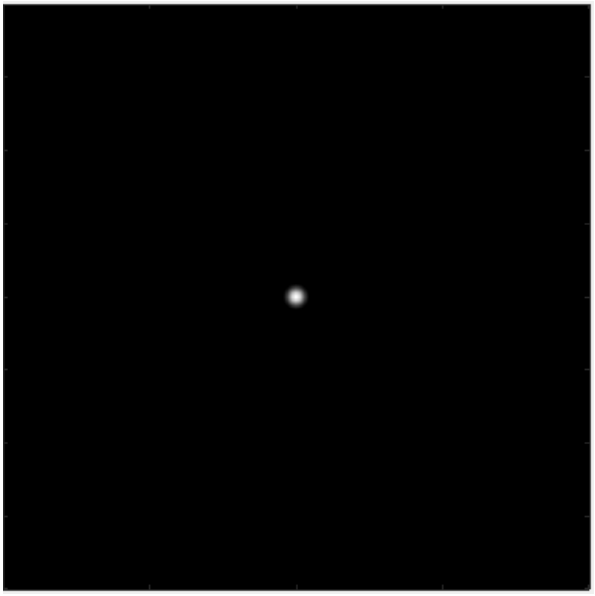

Figure 4.2: Apertured Bessel Beam

4.2.2 Power in the Bessel Beam

The power contained in the Bessel beam within a radial distance *b* can be derived by integrating the general Bessel beam expression in equation 4.6, this yields:

$$P = A_0^2 \int_0^{2\pi} \int_0^b J_0^2\,(rk_r) r dr d\phi = A_0^2 b^2 \pi (J_0(k_r b)^2 + J_1(k_r b)^2) \tag{4.9}$$

To obtain the power within the central core of the Bessel beam up to the first zero, we set $k_r = 2..4048/B_w$ and $b = B_w$, and this results in:

$$P_{B_w} = A_0^2 B_w^2 \pi J_1(2.4048) = 0.8467 A_0^2 B_w^2 \tag{4.10}$$

Let us consider a scenario where both Gaussian and Bessel beams are generated such that 99% of the Gaussian beam power passes through an aperture of radius B_w while 100% of the Bessel beam power passes through the same aperture. In this scenario, we can equate equation 4.10 to equation 4.2 and find that the peak intensity of the Bessel beam is about 1.176 times larger than the peak intensity of the Gaussian beam.

The general Bessel beam in equation 4.6 can decomposed into an infinite set of plane waves expressed below, for zeroth order (n=0), each at angle θ to the axis of propagation:

$$E(r, \phi, z) = A_0 \exp(ik_z z) \int_0^{2\pi} \exp[ik_r(x cos\phi + y sin\phi)] \frac{d\phi}{2\pi} \tag{4.11}$$

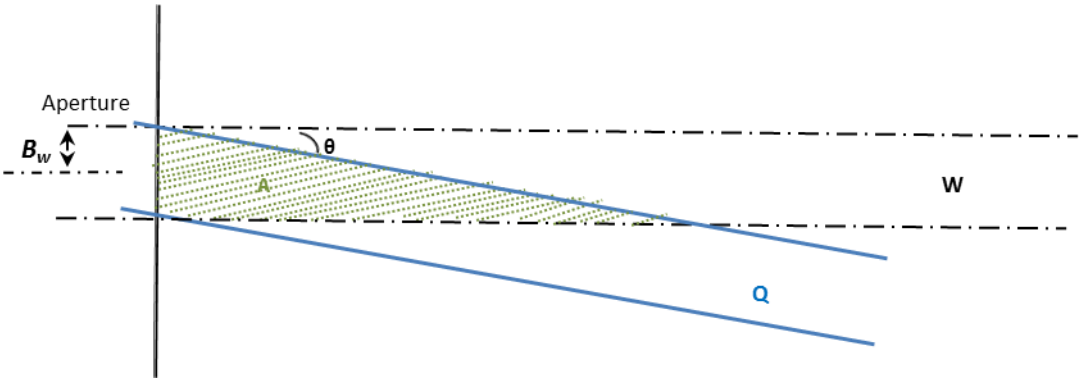

Figure 4.3: Bessel Beam decomposed into a set of plane waves.

Figure 4.3 is a pictorial representation of equation 4.11 for a single value of $\delta\phi$. Region W is the cylinder extruded from the aperture function while Q is that extruded from the

plane wave. The shaded region, A (= Q ∩ W) is the region of no power loss as the beam propagates. The energy contained within a single plane wavefront at angle $\delta\phi$ is the integral of the wavefront in the region A. The power contained in the W region can be obtained by integrating over all the ϕ:

$$P(z) = \left| \iint_A \int_0^{2\pi} \exp[ik_r(x\cos\phi + y\sin\phi)] \frac{d\phi}{2\pi} dxdy \right|^2 \tag{4.12}$$

$$P(z) = \left| \iint_A J_0(k_r r) \mathrm{d}x\mathrm{d}y \right|^2 \tag{4.13}$$

Some simulations were carried out to find out the distance at which half the power was lost. This was obtained by implementing equation 4.13 as well as the Fresnel propagation code, for a range of apertures 0.01 to 1 m. It was found that the half-power distance appears to be at Z_{max}. But when k_r is assumed to be small such that the first root of the beam is equal to the radius of the aperture function, the half-power distance appears at about $(1.1803532 \pm 0.0000067) Z_{max}$.

Again, if we assume that the amplitude of the Bessel beam is zero at the edge of the aperture function, we are able to derive an expression for the minimum beam radius, from equation 4.7 and 4.8, expressed as:

$$B_w^{min} = \sqrt{\frac{2.405 Z_{max}}{k}} \tag{4.14}$$

Recalling that when k_r is small, the half-power distance is at approximately $1.18Z_{max}$, hence equation 4.14 becomes:

$$B_w^{min} = \sqrt{\frac{2.405Z_{max}}{1.18k}} \tag{4.15}$$

Table 2 shows another list of useful propagation targets, this time for Bessel beam propagation from ground to space. Here, the third column is derived from equation 4.15, which are the minimum radius of the transmit and receive telescopes required to ensure that not more than half the power of the initial beam is lost.

Table 4.2: Useful propagation targets II

Propagation Target	**Altitude (km)**	**Beam radius (B_w^{min})**
An A320 Aircraft ceiling	12	44mm
Higher Altitude Aircrafts	27	77mm
International Space Station (ISS)	340	235mm
Low Earth Orbit (LEO) Satellite	700	337mm
Global Position System (GPS) Satellite	20,350	1.82m
Geostationary Orbit (GEO) Satellite	35786	2.41m

Clearly from table 4.2, larger diameters of telescopes are required for longer distance propagation of Bessel beams. Compared to table 1, it can be seen that Gaussian beams require larger diameters of telescopes to ensure not more than half the power is lost for the same distance of propagation, compared to the Bessel beam which requires a smaller transmitter size. This is the case because we have shown that to achieve maximum propagation distance, the Bessel beam's radial frequency k_r needs to be chosen such that the aperture function radius is equal to the first root of the Bessel function. Hence the

Bessel beam is more convenient than the Gaussian as it requires less weight, cost and size.

4.3 Modelling the Atmospheric Turbulence

In this section, we will model the atmospheric turbulence in the medium. It is critical to be able to model effectively the random turbulence in the atmosphere. As earlier mentioned in section 3.2.8, the phase screen method is used here due to its simplicity for analytical calculations and computer simulations. Here, a finite number of phase screens are imaginarily placed at intervals through the atmosphere, in a split-step method. In the split-step method, the entire propagation path is logically split into equal intervals and the beam is hence propagated in intervals. The phase screens are applied at every other interval, before the next advancement of the beam, and this continues till the whole propagation path length is covered. The first subsection discusses our derived model for the C_n^2 with respect to altitude, from where we derive a maximum height above which the effect of turbulence is considered negligible. The second subsection summarises the generation of the phase screens.

4.3.1 Maximum Height for Turbulence

As established in section 3.2, the strength of atmospheric turbulence C_n^2 is not fixed in any way as it varies with altitude, location and time of the day. However, C_n^2 is only considered fixed when trying to model terrestrial (ground-to-ground) applications; but for ground-to-space applications, it varies with height.

The Hufnagel-Valley's model of C_n^2 with respect to height h above the ground is one of the most widely accepted. The Hufnagel-Andrews-Philips (HAP) model, earlier defined in equation 3.87, is an efficient modification to the Hufnagel-Valley model and accounts for time of the day, *p.* It is repeated below for reference:

$$C_n^2(h) = M\left[0.00594\left(\frac{v_u}{27}\right)^2\left(\frac{h+h_s}{10^5}\right)^{10}\exp\left(-\frac{h+h_s}{1000}\right) + 2.7 \times 10^{-16}\exp\left(-\frac{h+h_s}{1500}\right)\right] + C_n^2(h_0)\left({}^{h_0}/_{h}\right)^p, h > h_0 \quad (4.16)$$

Here, the h_0 is the height of the measuring instrumentation above the ground and h_s is the height of the ground platform above sea level. The $C_n^2(h_0)$ is the refractive index structure constant at h_0. The factor M (mostly> 5) is a scaling factor that describes the average value of the level of random background turbulence and can be suited to fit the measured conditions at various locations. From the above HAP model in equation 4.16, using the factor M = 6.5, and if the ground platform and measurement instrumentations are assumed to be at sea level (h_s and h_o = 0), we derive a modification to the $C_n^2(h)$ as:

$$C_n{}^2(h) = 6.5\left[3.593 \times 10^{-3}\left({}^{h}/_{10^5}\right)^{10} e^{(-h/1000)} + 2.7 \times 10^{-16} e^{(-h/1500)}\right] \quad (4.17)$$

Given that typical values for C_n^2 are known to be ranging from 10^{-13} to 10^{-18} $m^{-2/3}$, we can deduce from equation 4.17 above that the maximum height above which C_n^2 would be lower than as 10^{-18} $m^{-2/3}$ will be 22 km high. Based on our model, the range for $C_n{}^2$ is from $C_n{}^2(0) = 1.75\times 10^{-15}$ to $C_n{}^2(22km) = 1.73 \times 10^{-18}$. This means that there would be negligible atmospheric turbulence at altitudes above 22km. This fact will be key when simulating the optical beam propagation for a ground-to-space scenario as the

turbulence phase screens will terminate at this altitude, then the beam will be assumed to be propagating through a vacuum for the rest of the path.

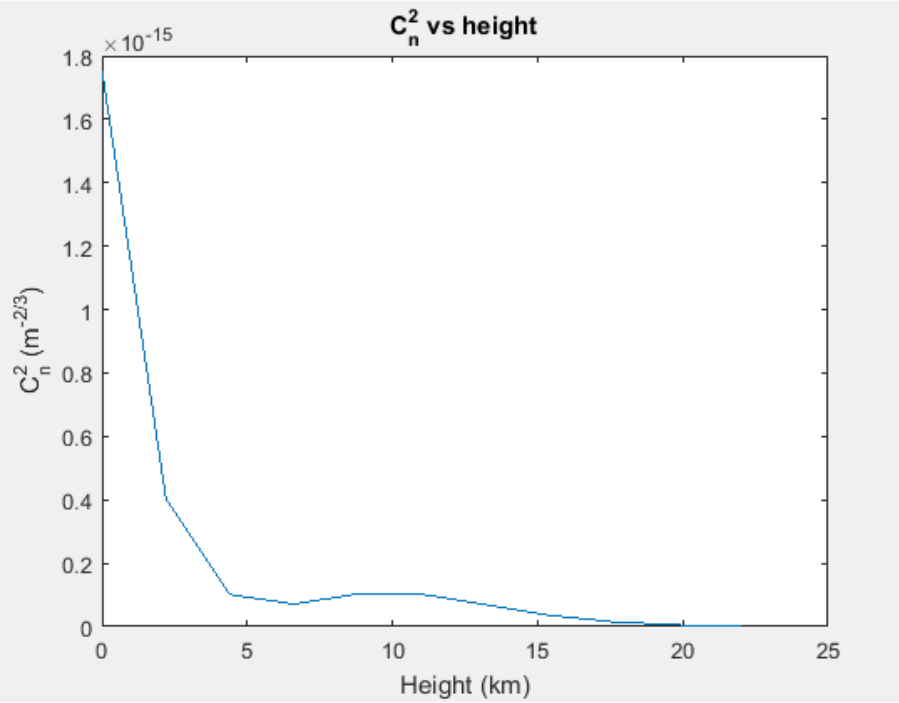

Figure 4.4: C_n^2 vs height

Figure 4.4 above is plot of C_n^2 against height, based on equation 4.17. It can be observed that the strength of the turbulence C_n^2 is at its maximum on the ground level and gradually weakens with altitude. From equation 3.88 which is repeated in 4.18 for reference, as the C_n^2 gradually weakens, the Fried parameter r_0 will be increasing with height as shown in the graph in figure 4.5.

$$r_{0,pw} = \left[0.423k^2 \int_0^h C_n^2(h)dh\right]^{-3/5} \tag{4.18}$$

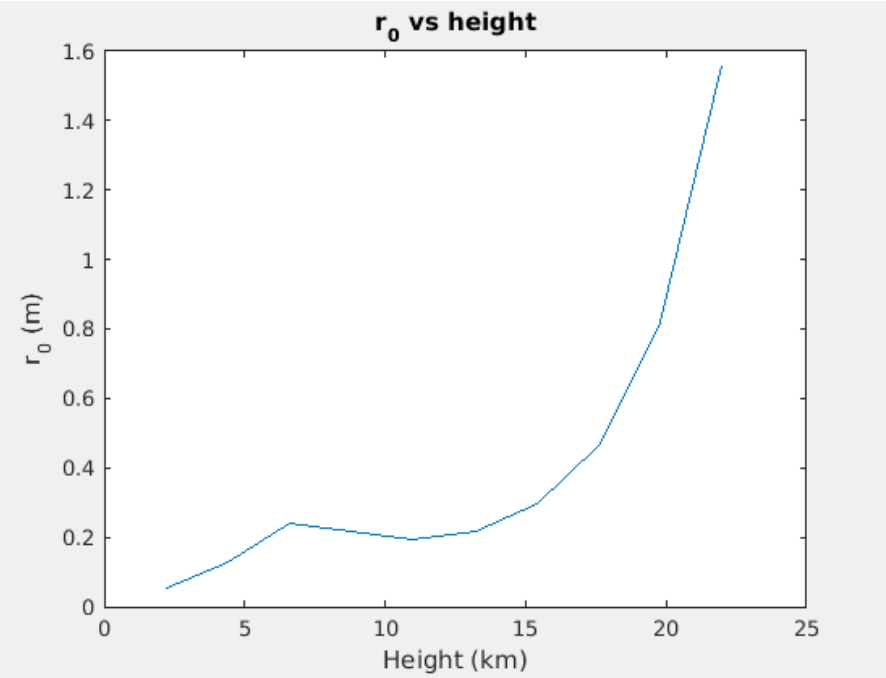

Figure 4.5: Fried parameter r_0 vs height

4.3.2 Turbulence Phase Screens

As earlier established in section 3.2.7, when modelling atmospheric turbulence, it is considered as a finite number of discrete layers, each layer being a thin phase screen. Here, we model the atmospheric turbulence using this generally-accepted approach of phase screen layers imaginarily placed within the atmosphere. Among the different methods used to model the phase screen, we adopt the Fourier Transform method because of its computational efficiency. Additional sub-harmonics are included to compensate for the deficient low frequency components.

For a finite square grid, the Fourier Transform-based phase screen is generated using the expression in equation 3.116, which is repeated below:

$$\emptyset(x,y) = \sum_{n=-\infty}^{\infty} \sum_{m=-\infty}^{\infty} [R(N) + \mathrm{i}R(N)] \times \sqrt{\Phi_\phi} \times \exp[i2\pi(f_{x_n}x + f_{y_m}y)] \qquad (4.19)$$

where *R* represents Gaussian random numbers with zero mean and unit variance. *N* is the number of grid points per side of the screen, $f_{x_n}$and f_{y_m} are the discrete spatial frequencies in the *x* and *y* directions. The Φ_ϕ is the phase Power Spectral Density (PSD) of turbulence. For this, we use the modified von Karman's phase PSD earlier defined in equation 3.93 but repeated below, since it is the simplest that includes the inner and outer scale:

$$\Phi_\emptyset{}^{mvk} = 0.49{r_0}^{-5/3}\frac{\exp(-k^2/{k_m}^2)}{(k^2+{k_0}^2)^{11/6}} \tag{4.20}$$

The r_0 is an implementation of equation 4.18 in terms of the C_n^2. At this point, a fixed C_n^2 for all the phase screens is used to model the atmosphere for cases where the beam is propagated across a horizontal and terrestrial path. But for the vertical and ground-to-space propagation path, the C_n^2 will be gradually-weakening with height in line with equation 4.17. After generating the phase screens using equation 4.19, the deficient low frequency components are generated based on the earlier defined equation 3.117, repeated below:

$$\emptyset_{lf}(x,y) = \sum_{p=1}^{N_p}\sum_{n=-1}^{1}\sum_{m=-1}^{1} C_{n,m}\exp[i2\pi(f_{x_n}x + f_{y_m}y)] \tag{4.21}$$

where *n* and *m* are discrete frequencies and each *p* represents the different grids. The $C_{n,m}$ are the random draws of the Fourier series coefficients.

One of the scenarios to be considered in chapter 5 is a ground-to-space scenario where the beams are propagated from sea level through turbulence up to 22 km altitude. In this case, the phase screens are produced every interval of 2.2 km such that 10 gradually weakening phase screens span equally across the 22 km height of atmospheric turbulence as seen pictured on figure 4.6. This is suited for the split-step propagation which will be adopted for the beam propagation in Chapter 5.

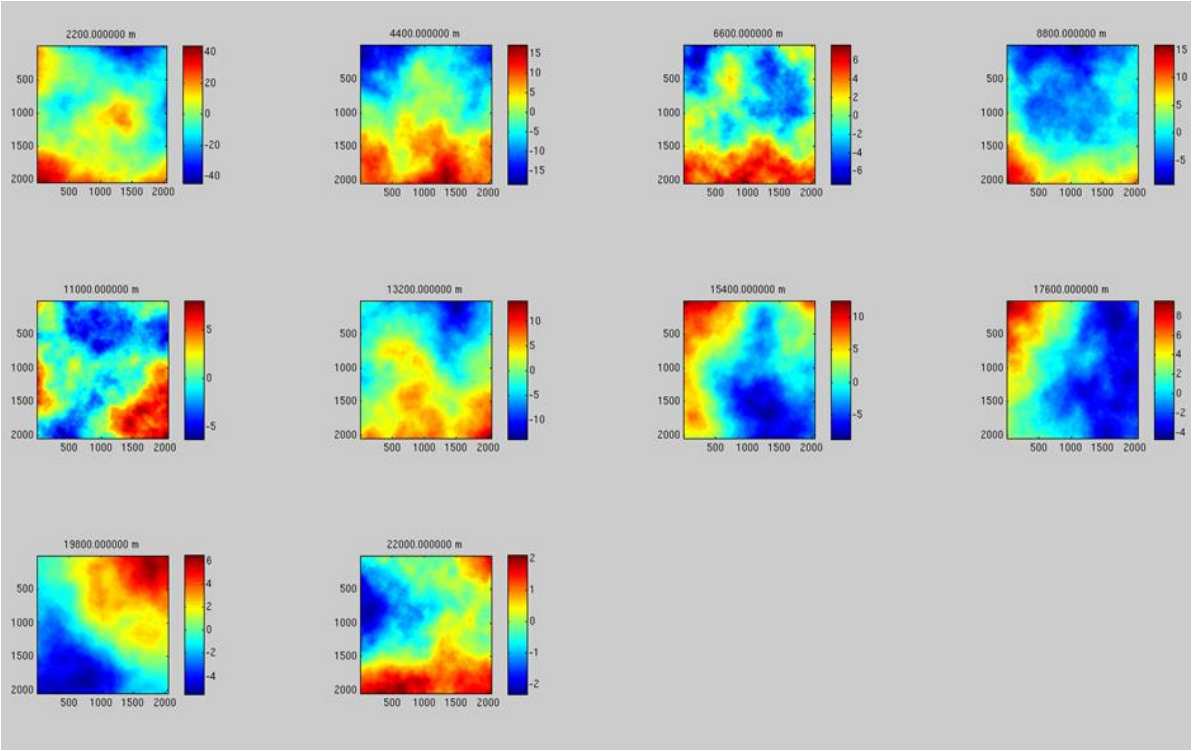

Figure 4.6: Phase screens for altitudes (2.2km to 22km). Grid 2000x2000 pixels.

Unit of phase (colour scale) in radians.

The phase screens grid side length as well as the number of pixel points N is taken to be the same as those for the source plane and the observation plane, which were chosen to satisfy the sampling constraints.

4.4 Chapter Conclusions

In this chapter, we were able to model the two beams; Gaussian and Bessel beams, which will be propagated in the chapters 5 and 6. We went on to derive some expressions to define the minimum source aperture radius for both beams, with their respective altitudes, to ensure that not more than 50% of the initial beam power is lost in transit before it arrives at the receiver. These definitions confirm the fact that the longer the distance of the FSO communication, the bigger the required size of the aperture of the transmitter and receiver to minimise power losses.

The second section of the chapter focused on modelling the atmospheric turbulence phase screens, using the Fourier transform method. We also arrived at a model for C_n^2 with respect to height, and based on this we derived a maximum height of 22 km above which the effect of turbulence will be negligible. This maximum height of 22 km will be very useful in Chapters 6 when simulating the optical beam propagation for a ground-to-space scenario as the turbulence phase screens will terminate at this altitude, and beyond this altitude the beam will be assumed to be propagating through a vacuum for the rest of the path. Based on the same C_n^2 model we derived, we saw that the C_n^2 will be considered fixed when modelling beam propagation through a horizontal terrestrial path (ground-to-ground applications) as will be seen in Chapter 5.

CHAPTER 5

5.0 SHORT RANGE BEAM PROPAGATION THROUGH TURBULENCE

In this chapter, the two beams generated in chapter 4 (Gaussian and Bessel beams) will be propagated for a short range of 2 km, first terrestrially with the transmitter and receiver at the same height of 100m above the ground, and then vertically- upwards with the transmitter on ground and the receiver at a 2 km altitude. A split step propagation method is called up here, where the total propagation distance is sectioned into smaller and equal intervals for more accurate modelling. We begin the chapter with consideration of the Fresnel Propagation sampling regimes then propagate the two beams without turbulence in order to investigate the diffraction effect on the beams. The horizontal path propagation through turbulence assumes that the C_n^2 will be fixed over the 2 km, while the vertically-upwards path assumes a gradually weakening C_n^2. The turbulence is modelled using phase screens described earlier in chapter 4. We compare the two scenarios (the horizontal 2 km path versus the vertically-upwards 2 km path) and see which one is better for short range FSO designs.

5.1 Fresnel Propagation Sampling Regimes (TF vs IF)

As seen in section 3.1.4.1, there are two approximations to the Rayleigh-Sommerfeld diffraction theory: the Fresnel and Fraunhofer Diffraction. Beam propagators are modelled based on these approximations. The Fresnel number criterion, $N_f = \frac{w^2}{\lambda z}$, is generally used to determine when the Fresnel expression can be applied with minimal loss of accuracy or when the Fraunhofer would be more suitable, w is the beam radius. If N_f is far less than (<<) 1, for example up to 20 to 30 times less than 1, then the observation plane is generally regarded to be in the Fraunhofer region. But if N_f is > 1, or slightly less or equal to 1, then it is in the Fresnel zone, hence the Fresnel

approximation is applied for useful results. Since we are adopting the split-step propagation where the long propagation path is split into intervals, then the observation planes will always be in the Fresnel zone. Therefore, we will use the Fresnel diffraction approximation for our propagator simulations.

The sampling regimes summarised in section 3.1.5.3 is key here to ensure that effects of aliasing do not impede the beams as they propagate. There are two forms of Fresnel propagation regimes: the Fresnel Transfer function *TF* and Fresnel Impulse Response *IR* are both the similar expressions but will produce different results due to some constraints earlier summarised in table 3.2. Depending on whether the chosen sampling interval Δx is greater than or less than $\frac{\lambda z}{L}$ (where z is the propagation distance, *L* is the source and observation plane side length and λ is the wavelength), *TF* or *IR* is selected. As earlier discussed, oversampling is the desirable situation to ensure aliasing is avoided whereas undersampling results in undesirable display artifacts and/or periodic copies of the field at the observation plane. The *TF* regime is suitable if $\Delta x > \frac{\lambda z}{L}$ the *IR* is suitable when $\Delta x < \frac{\lambda z}{L}$.

In this simulation, we defined a conditional statement on MATLAB for the Fresnel propagator that automatically selects the appropriate regime to use depending on the parameters. Again we ensure that the size of the beam apertures *D* were much less than the source and aperture side lengths, *L*. When the criteria are not adhered to, errors as shown in figure 5.1 are obtained, where there are periodic duplicates of the received field at the observation plane. More of these simulation errors and their causes can be found in Appendix B.

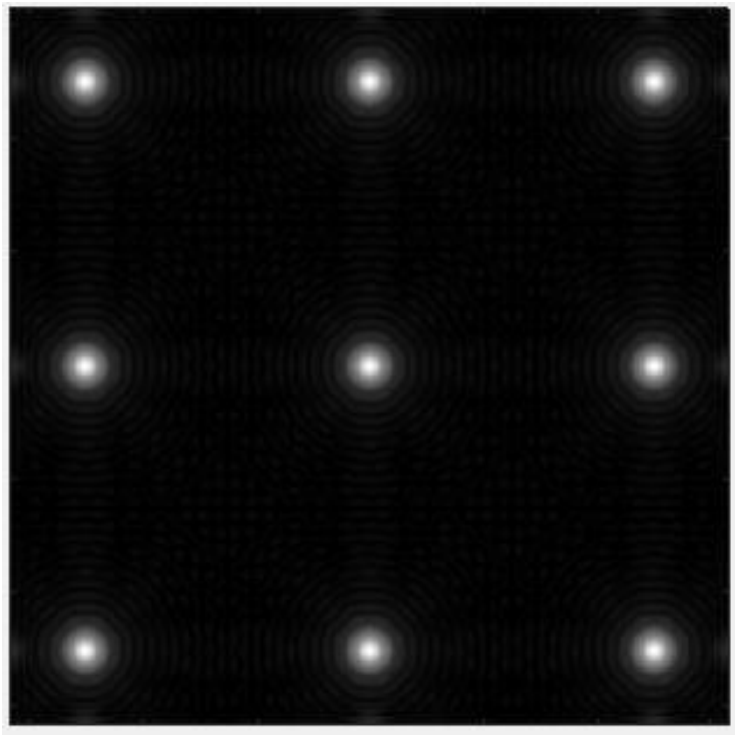

Figure 5.1: Aliasing on propagated Gaussian beam

5.2 Beam Propagation without Turbulence

The lower atmosphere definitely contains a considerable amount of turbulence. However, it is useful to monitor the effect of diffraction alone without turbulence, on the Gaussian and Bessel beam as they propagate over a range. Both beams have been apertured to the same radius of 0.2 m. Diffraction is known to cause the propagating beam to spread resulting in the on axis intensity of the beam decaying as it diffracts further.

The intensity error in figure 5.2 is the propagating beam intensity minus the intensity of the initial beam (at ground level for vertical propagation), before propagation. Clearly, the Gaussian beam diffracts a lot more than the Bessel beam as its intensity error from

the initial beam is much greater. The Bessel beam, known for its non-diffracting attributes, maintains an almost constant intensity error as it propagates.

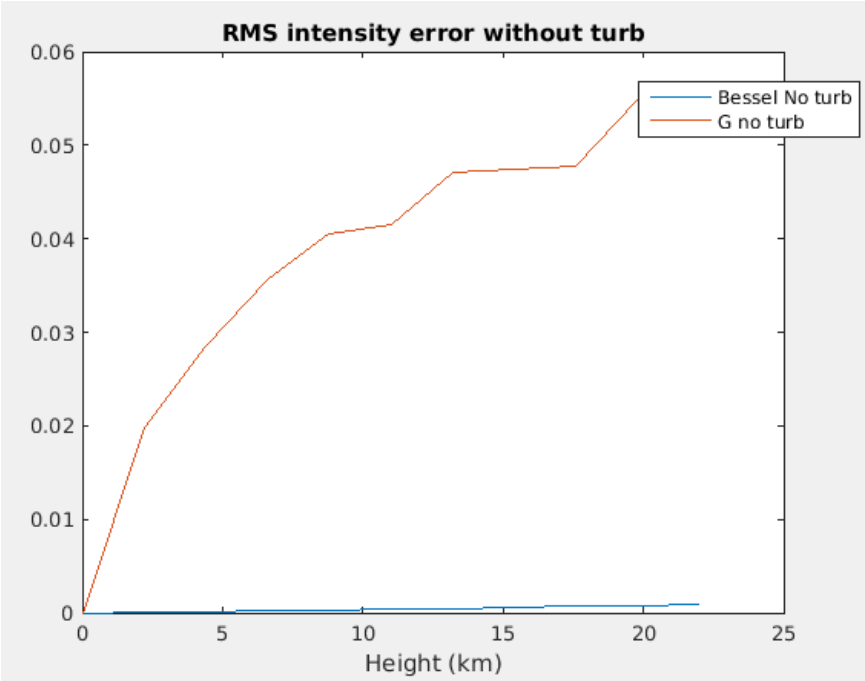

Figure 5.2: Beam Intensity error without Turbulence

5.3 Beam Propagation through a fixed atmospheric Turbulence (for a 2 km horizontal path)

For a ground-to-ground horizontal optical path, the strength of turbulence C_n^2 across the path will be fixed because the source and destination are at the same altitude. If the transmitter and receiver are both at an elevation of 100 metres above sea level, the corresponding strength of turbulence across the path C_n^2 (100 m) from the C_n^2 *(h)* model in equation 4.17 will be 1.64×10^{-15} m$^{-2/3}$. Equation 4.17 is repeated below for easy reference:

$$C_n{}^2(h) = 6.5\left[3.593 \times 10^{-3}\left(h/10^5\right)^{10} e^{(-h/1000)} + 2.7 \times 10^{-16} e^{(-h/1500)}\right] \quad (5.1)$$

and the corresponding coherence parameter r_0 is derived from equation 4.18, also repeated below:

$$r_{0,pw} = \left[0.423k^2 \int_0^h C_n{}^2(h)dh\right]^{-3/5} \quad (5.2)$$

We examine the propagation of the two beams across a 2 km horizontal path, through the fixed turbulence C_n^2 of 1.64×10^{-15} m$^{-2/3}$, when both transmitter and receiver are at 100 m altitude. We use an inner scale l_0 of 0.01 m and an outer scale L_0 of 100 m. Again, the two beams under consideration are apertured to 0.2 m radius. Fresnel diffraction is used for the beam propagation and the split step propagation method is adopted, splitting the 2 km path into 20 layers of 100 m each. The turbulence phase screens are logically placed at each of the intervals. The wavelength $\lambda = 500$ nm, the array size was 1024×1024 pixels^2 representing an array of 8×8 m^2.

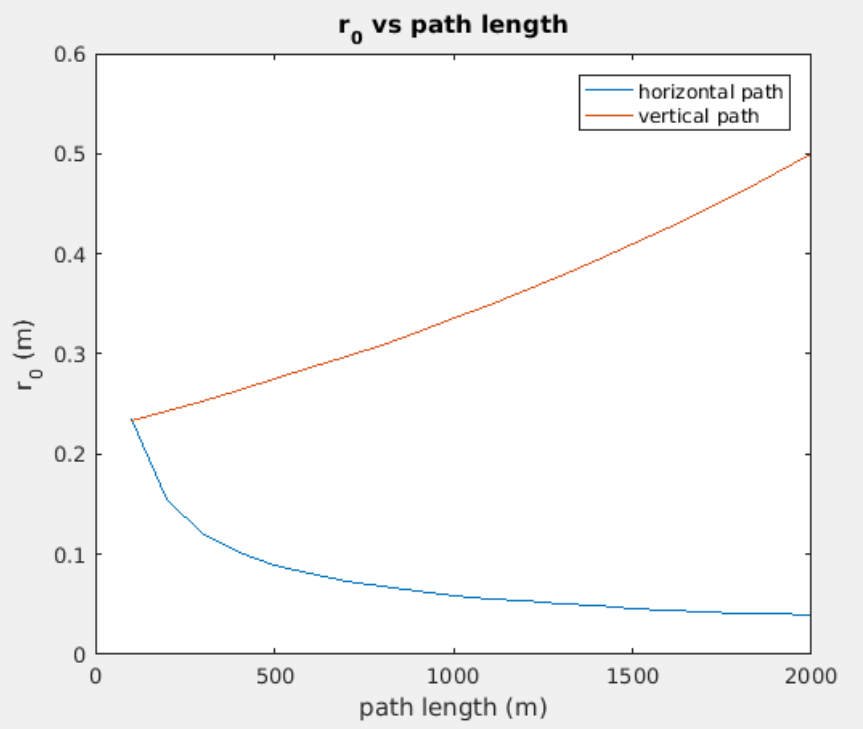

Figure 5.3: Comparison between r_0 for fixed turbulence and gradually-weakening turbulence

It should be noted that since the C_n^2 is fixed across the horizontal propagation path, the corresponding coherence parameter r_0 at every interval of propagation, derived from equation 5.2, will be decreasing gradually as the distance of propagation increases as shown in figure 5.3. This contrary is the case for an equivalent vertical path propagation through gradually weakening C_n^2, where r_0 was increasing as the propagation path increased. Hence, for a fixed-turbulence horizontal path optical propagation, the strength of turbulence builds up significantly with increasing propagation path length. From this, one can expect that a beam propagated through a horizontal path is more susceptible to errors than an equivalent vertical path, as will be demonstrated in figures 5.4 and 5.5.

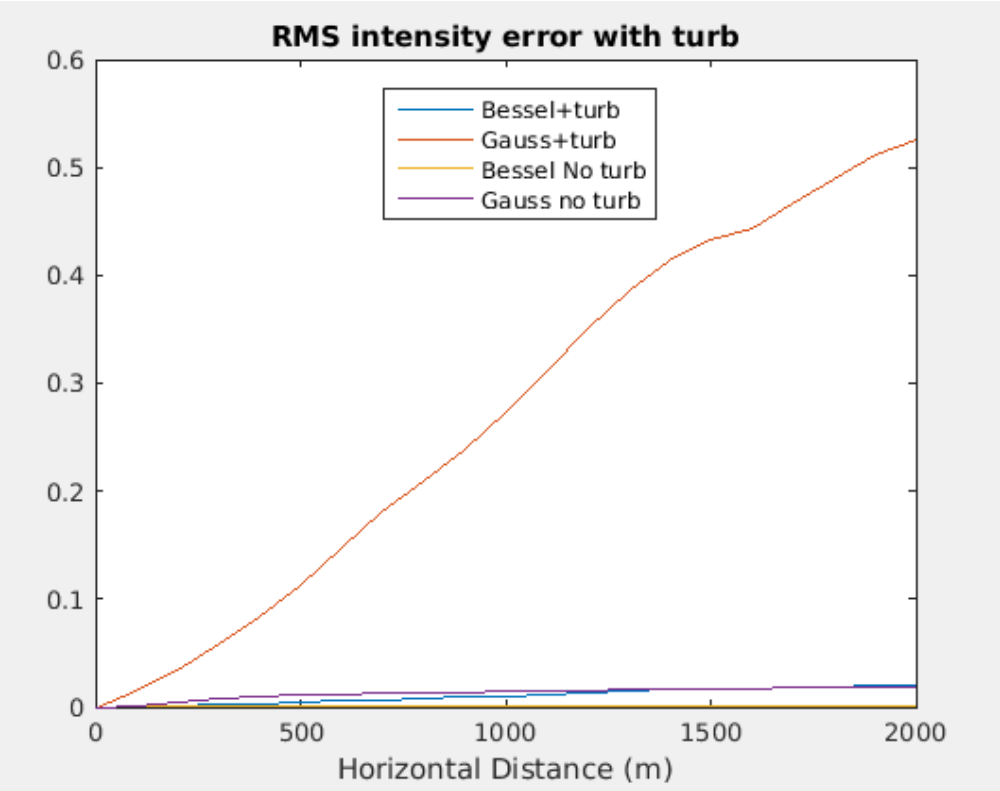

Figure 5.4: RMS Intensity Error for beam propagation through fixed Turbulence.
The intensity error is defined as the intensity of the propagating beam minus the intensity of the beam at sea level, before propagation.

When the two beams are propagated through the same 2 km horizontal ground-to-ground path scenario described above, it can be seen in figure 5.4 that the Gaussian beam is significantly aberrated by the strong turbulence as it propagates such that its intensity error from the initial beam is rapidly increasing as it propagates. The Bessel beam on the other hand, is only slightly aberrated as it propagates through the strong turbulence and there is no much difference between its intensity error when it is propagating through turbulence and when it is propagating without turbulence. As will be seen in section 5.4, for an equivalent 2 km range but for a vertical upwards propagation, the beams will experience less aberration as they propagate, compared to the ground-to-ground horizontal range.

5.4 Beam Propagation through gradually-weakening atmospheric turbulence

In this scenario, the transmitter is assumed to be on the ground (at sea level) and the propagation proceeds vertically-upwards to an altitude of 2 km. Again, Fresnel diffraction is used for the beam propagation. The wavelength $\lambda = 500$ nm, the array size was 1024×1024 pixels^2 representing an array of 2×2 m^2. The outer and lower atmospheric scales used were $L_0 = 100$ m and $l_0 = 0.01$ m.

The same beam aperture radius B_w of 0.2 m is considered for both initial Gaussian and Bessel beams, before propagating to the 2 km altitude. This allows us to be able to make a sensible comparison with the horizontal propagation path scenario in section 5.3 which was also considered for the same 2 km range. The simulation of the atmospheric turbulence for the vertically-upwards scenario is based on the model stated in equation 4.5 for a gradually diminishing C_n^2 with height.

Figure 5.5 below illustrates the beams propagated in this scenario. Comparing figure 5.5 to figure 5.4, the Bessel beam still has a better performance than the Gaussian, as it was in the horizontal ground-to-ground scenario. Furthermore, it can be observed that for the same propagation range of 2 km, if the propagation path is horizontal (fixed turbulence), the beams are more aberrated (with more intensity error) than for a vertical ground-to-space path.

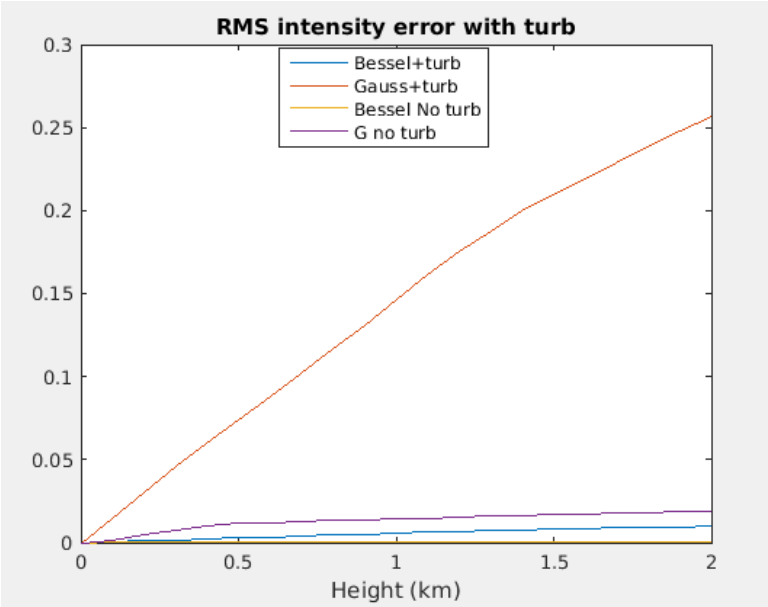

Figure 5.5: RMS Intensity Error for propagation through gradually-weakening turbulence. The intensity error is defined as the intensity of the propagating beam minus the intensity of the beam at sea level, before propagation.

5.5 Chapter Summary

In this chapter, we considered the propagation of the two beams for a 2 km FSO range. The primary aim was to demonstrate that the orientation of the path (whether horizontal or vertical) is an important consideration in FSO system design. The Gaussian beam clearly was more susceptible to diffraction and turbulence in all the scenarios as it had a higher Intensity error performance than the Bessel beam. Furthermore, the horizontal 2 km path, where both transmitter and receiver where 100 m above the ground, had a poorer intensity error performance than the 2 km vertically-upwards path. This is because the turbulence in the latter is gradually-weakening whereas that of the former is fixed resulting in accumulation of the turbulence effects as it propagates. Hence, we have shown that in the design of an FSO system, it is critical to ensure a considerable difference in altitude between the transmitter and receiver, rather than placing them on the same altitude. For example, the transmitter could be positioned on the ground level while the receiver is positioned at the top of a sky-scrapper or a high mountain.

CHAPTER 6

6.0 LONG DISTANCE BEAM PROPAGATION THROUGH TURBULENCE (UP TO 22 KM ALTITUDE AND DEEP SPACE)

This chapter will investigate the propagation of the two beams under consideration, the Gaussian and Bessel beams, from ground to space. The transmitter is assumed to be at sea level propagating vertically upwards. The first section will investigate the beams propagated up to the 22 km height; this height which was earlier derived in Chapter 4 to be the assumed maximum height for the existence of atmospheric turbulence. The second section will analyse what happens when the beams are propagated beyond the 22 km height, in vacuo, up to an altitude of 100 km. The performance of the two beams are compared to each other as they propagate through these two scenarios. We also investigated the performance of different beam sizes, for the two beams, in order to select the beam size that is more suitable for the different performance criteria.

The useful propagation targets and distances earlier derived in tables 4.1 and 4.2 are brought forward here in table 6.1, this time including labels to help identify their respective beam radii as they will be useful subsequently.

Table 6.1: Useful propagation targets and their respective half power beam radii

Label	Target	Altitude (km)	$W_{0.5P}$	B_w^{min}
∘	An A320 Aircraft ceiling	12	59mm	44mm
+	Higher Altitude Aircrafts	27	89mm	77mm
∗	International Space Station (ISS)	340	315mm	235mm
×	Low Earth Orbit (LEO) Satellite	700	452mm	337mm
□	Global Position System (GPS) Satellite	20,350	2.44m	1.82m
◊	Geostationary Orbit (GEO) Satellite	35786	3.23m	2.41m

Due to diffraction of the propagated beam, the beam tends to over-fill the array at a stage during its propagation. If any power is detected at the edge of array, the captured beam power is low, hence the propagation is safely halted. This happens approximately at 5 km altitude for the ∘ label and about 16 km for the + label, and so on as shown pictorially in figure 6.1 below. This point where the power is detected at the edge tends to be at longer range as the half-power beam radius increases for both Gaussian and Bessel beams.

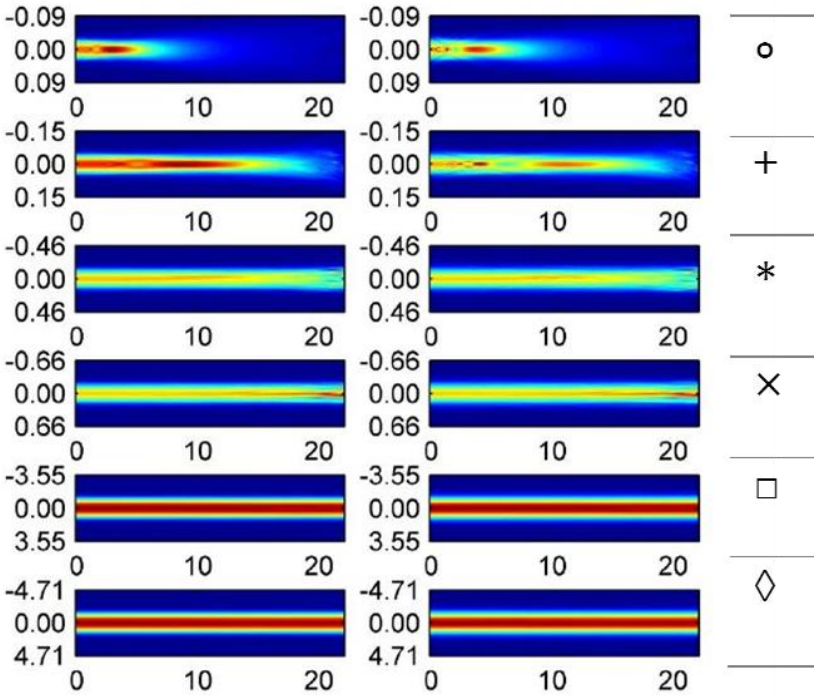

Figure 6.1: Intensity cross sections versus the propagation distance

Figure 6.1 above shows Intensity cross sections plotted against the propagation distance with a false colour map. The vertical axes are the beam radial coordinates in meters while the horizontal axes are the propagation heights in kilometres. The initial beamwidths before propagation are obtained from table 6.1 for both the Gaussian beam and Bessel beam. The images on the left hand side are for the Bessel beam propagation while those on the right hand side are for the Gaussian beam.

6.1 Beam Propagation from Ground to 22 km altitude

In this section, the two beams will be propagating from ground to space through atmospheric turbulence up to the turbulence altitude limit of 22 km. The results that will be discussed henceforth are obtained after averaging over 100 runs of the simulation.

An ideal and desirable FSO communication system needs to have the following attributes:

- The transmitting beam needs to have a high peak intensity with as little of the beam power as possible contained in the sidelobes.
- As much of the initial beam power as possible, successfully delivered to the receiver.
- The peak of the transmitting beam intensity profile needs to remain around the propagation axis. This will enable it not to wander away from the receiver aperture.
- The transmitter optics (including the receiver) should be as small as possible for convenience.

The remainder of this section discusses to what extent the above attributes have been realised when comparing the propagation of the different beamwidths of the Gaussian and the Bessel beam. This will considered based on 4 different performance measure: Normalised captured power, Peak Position error, RMS Intensity error and Beam Wander.

6.1.1 Normalised captured Power

This is the amount of power captured by a receiver of aperture radius equal to that of transmitter B_w. Here, it assumed that both Gaussian and Bessel beams have the same initial beam power, before they are propagated through atmospheric turbulence. As mentioned earlier for a desirable FSO system design, the receiver needs to successfully capture as much of the initial beam power as possible. Figures 6.2 and 6.3 show the performance of the beams based on this factor.

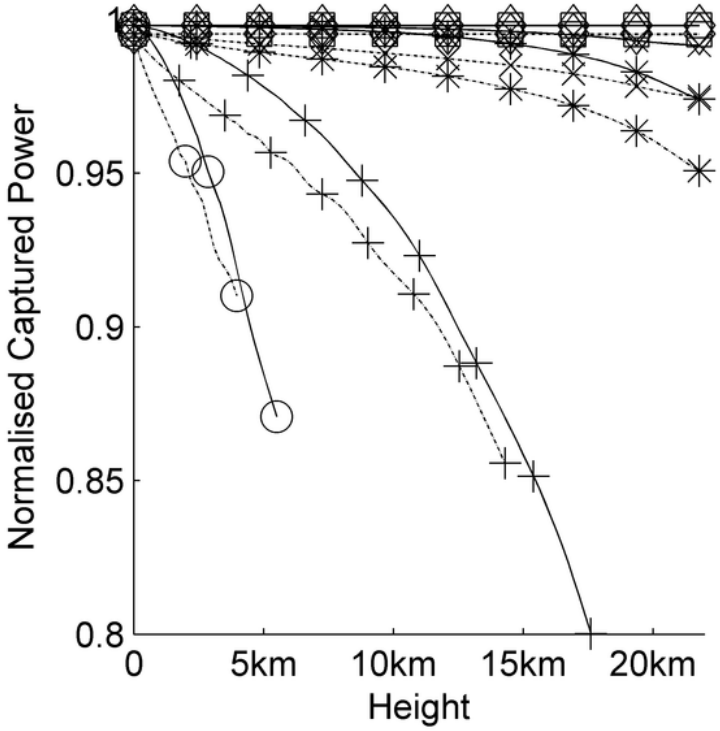

Figure 6.2: Captured Power versus Height.
—— Bessel Beam. ····· Gaussian Beam.
The labels are defined in table 6.1 for different aperture radii.

Figure 6.2 above shows the amount of power captured by a receiver whose radius is the same as the transmitter radius, for the two beams, and for different beam sizes. The labels represent the radii of the transmitter apertures and are as defined in table 6.1. The

solid lines are for the Bessel beams and the broken lines are for the Gaussian beams. Since both the Gaussian and Bessel beams have the same amount of initial power, it can be observed that for all of the beam aperture radii, the Bessel beam has more of its initial power successfully transferred to the receiver. Hence it outperforms the Gaussian beam in this regard. The beam power is integrated over the whole aperture and that ensures there is no ringing, compared to the peak intensity cases as will be seen later in figures 6.4 and 6.5.

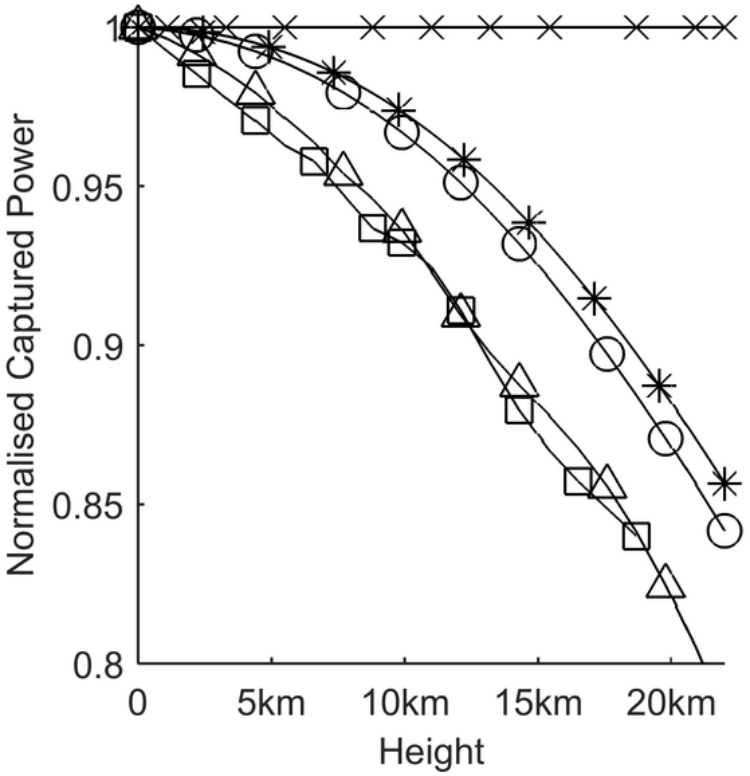

Figure 6.3: Power captured by a receiver versus height *in vacuo*.
∘ Gaussian beam with no ground level aperture. × Bessel Beam with no ground level aperture.
□ Gaussian with ground level aperture. Δ Bessel beam with ground level aperture.
∗ Theoretical apertured Gaussian beam power transmitted, from equation 4.5.

The aim of figure 6.3 is to verify that the propagation codes used are correct. Unlike the rest of the figures, the labels used in figure 6.3 are not based on table 6.1. But we consider only one of the items of table 6.1: the *High Altitude Aircraft* (+) beam aperture

radii which requires a minimum aperture radius of 77 mm for the Bessel beam and 89 mm for the Gaussian, to ensure not more than half the initial power is lost in transit. Hence for this, we use an initial beam radius of 77mm for Bessel and 89 mm for Gaussian beam. As seen in the figure 6.3, an un-apertured Bessel beam (×) propagates infinitely without any power loss. It can also be observed that the Gaussian beam without ground level aperture (o) has almost a similar power loss pattern as the theoretical Fresnel transmitted power. This proves that the simulation code used is giving correct results. Lastly from figure 6.3, the introduction of ground level apertures to both the Gaussian and Bessel beams results in ringing of the beam (shown by the wavy power-captured line) as well as significant power loss compared to the un-apertured ones.

6.1.2 Peak Intensity

Here, we investigate how much of the initial beam power remains in the central peak of the received beam. The desirable situation is that the transmitting beam needs to have a high peak intensity with as little of the beam power as possible contained in the side-lobes. Figures 6.4 and 6.5 show the performance of the two beams, and with a range of beam sizes, based on this factor.

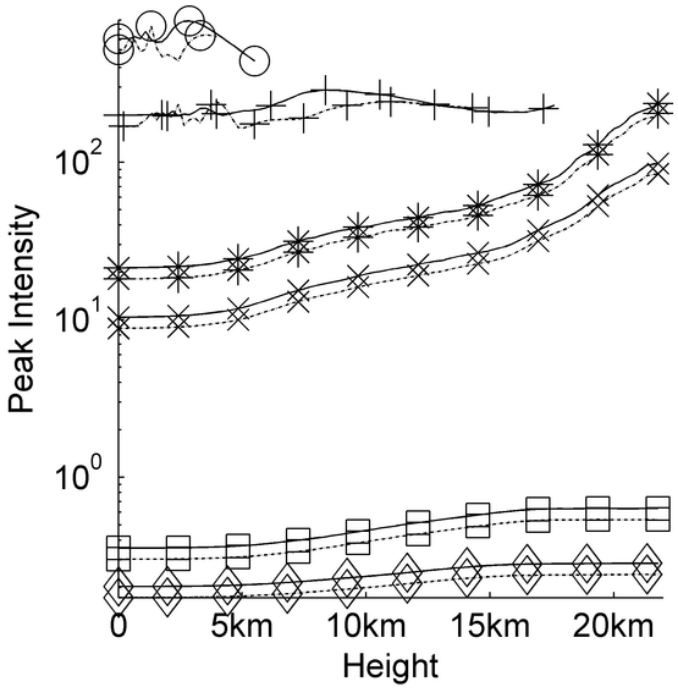

Figure 6.4: Peak intensity versus Height. —— Bessel Beam. ····· Gaussian Beam
The labels are defined in table 6.1 for different aperture radii.

If both the Bessel and Gaussian beams are set to an equal beam power of unity, the peak intensity of the Bessel beam is expected to be slightly higher than that of the Gaussian beam as earlier shown in equation 4.10. Again, from equation 4.10, the larger the aperture size, the smaller the peak intensity is expected to be. Figure 6.4 pictures this. Clearly, for each of the aperture sizes, the Bessel beam has a slightly higher peak intensity than the Gaussian beam and this remains the same as the beams propagate downstream and through the atmospheric turbulence. The smaller apertures have larger peak intensities as expected.

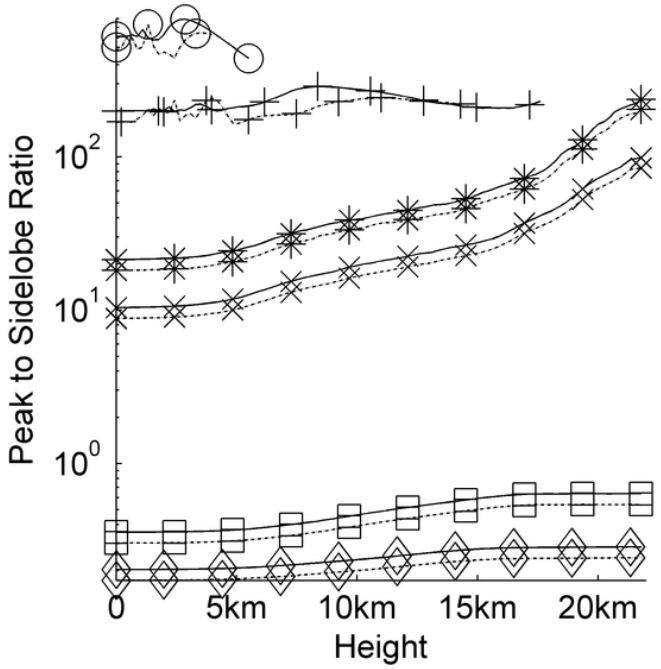

Figure 6.5: Peak intensity to sidelobe ratio versus Height.
—— Bessel Beam. ····· Gaussian Beam
The labels are defined in table 6.1 for different aperture radii.

A large peak intensity to side-lobe ratio implies that more of the power is concentrated in the centre region of the beam and is not spread out across the beam field. This is a desirable feature as the receiver is ideally designed to focus on the central core for cases where the arriving beam is too large. Figure 6.5 is somewhat similar to the figure 6.4 since most of the side-lobe power is still captured by the receiver. Figure 6.5 clearly illustrates that the Bessel beam has more of its received beam power concentrated in the central region. As it propagates through turbulence, the Bessel beam remains more concentrated at the centre region than the Gaussian beam. However, in section 2.3, it was established that before propagation, the Bessel beam concentrates less of its power in the central core and has a considerable amount of its power in the rings while the Gaussian beam is more concentrated. Figure 6.5 does not contradict this theory but shows that when propagated through turbulence, the Gaussian beam's power, though initially more concentrated, is eventually more spread out than the Bessel beam. The

effect of the ringing at the edge of the aperture is seen in the slight wavy plot lines but this is minimal because the peak intensity position can be anywhere within the aperture, not necessarily at the centroid position.

6.1.3 Intensity Error

Here, we measure the performance of the beams based on the RMS value of the difference between the intensity of the propagating beam (through turbulence) and that of the initial beam before it was propagated (at sea level in this case with z = 0). The performance of the beams based on this criterion is illustrated in figure 6.6. However, in figure 6.7, we have a special case were the intensity error is the difference between the propagating beam intensity and the intensity of the unaberrated beam that has travelled the same distance but without turbulence.

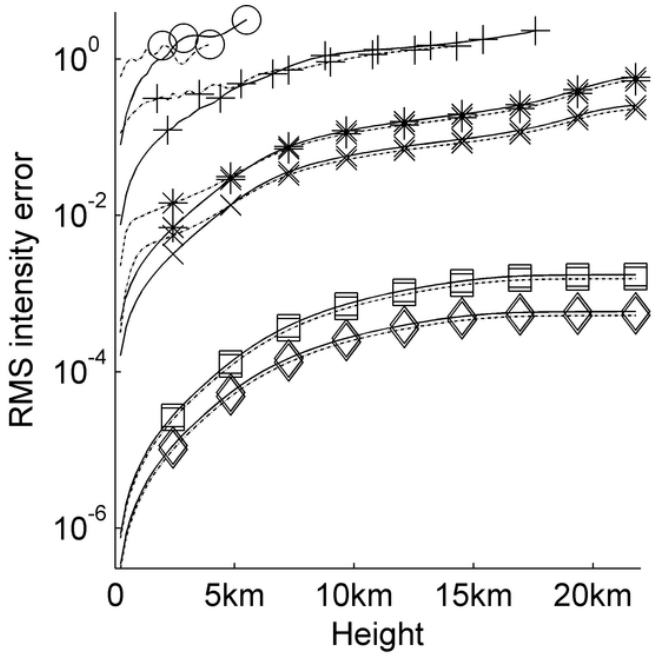

Figure 6.6: RMS Intensity Error versus Height. The intensity error is the intensity of the propagating beam minus the intensity of the beam before propagation.
—— Bessel Beam. ····· Gaussian Beam
The labels are defined in table 6.1 for different aperture radii.

A lower value for Intensity error indicates that the intensity has not dropped much from the initial intensity before propagation, hence entails better performance. The Gaussian beam shows better performance than the Bessel in this case as it has lower intensity error for all the beam aperture sizes. This is the case because the Gaussian beam's energy is more spread out than that in the central core of the Bessel beam which is more concentrated in the centroid region. The more spread out the energy of the beam, the less susceptible the beam will be to turbulence-induced phase errors. Hence, the turbulence-induced phase errors has less effect on the propagating Gaussian beam than the Bessel beam.

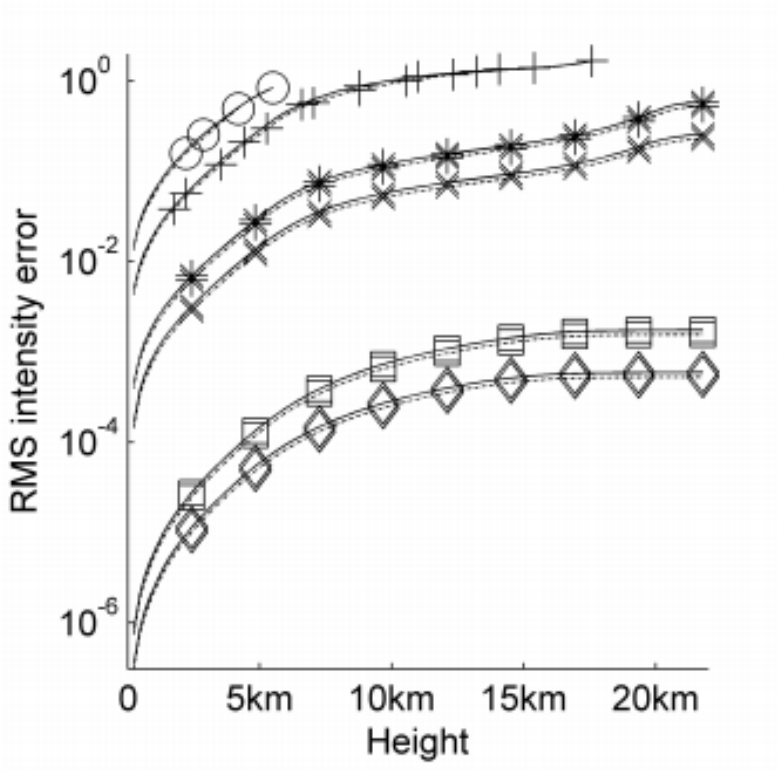

Figure 6.7: RMS Intensity Error versus Height. The intensity error is the propagating beam intensity minus the intensity of the unaberrated beam that has travelled the same distance but without turbulence.
—— Bessel Beam. ····· Gaussian Beam
The labels are defined in table 6.1 for different aperture radii.

Figure 6.7 shows the Intensity error from a different light. The Intensity error here is the difference between the beam intensity as it propagates through atmospheric turbulence and the beam intensity when it is propagating *in vacuo*. Again here, the Gaussian has a slightly better performance than the Bessel beam, hence the Bessel beam is more affected by turbulence than the Gaussian beam. For both figures 6.6 and 6.7, the larger beam apertures have better performance with less intensity errors as the beam power is directly proportional to beam size in line with equations 4.2 and 4.10.

6.1.4 Peak Position Error

This is known as Beam wander – the drift of the propagating beam's peak intensity position from the initial centroid position of the beam as a result of phase errors from the atmospheric turbulence. The initial beams are both created such that the pixel position of the peak intensity is in the centroid position of the source grid.

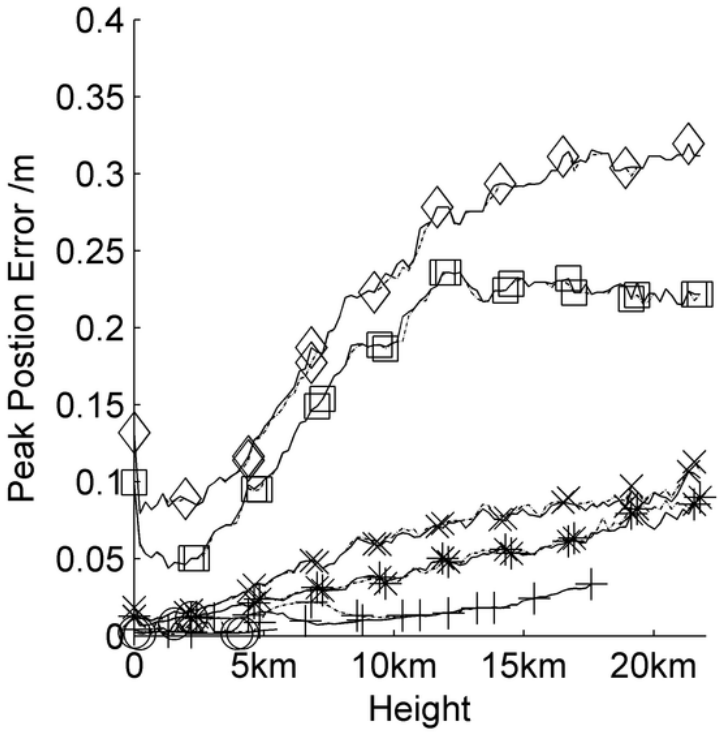

Figure 6.8: Peak position error ratio versus Height.
—— Bessel Beam. ····· Gaussian Beam
The labels are defined in table 6.1 for different aperture radii.

The peak position error on the y-axis of figure 6.8 is defined as the propagating beam's peak position minus the initial peak position of the beam before propagation (that is at z = 0). Here we see that both Bessel and Gaussian beams have identical beam wander results since they are both propagating through the same turbulence. The Bessel beams self-healing attribute cannot save it from the phase error as a result of propagating through atmospheric turbulence. Clearly from figure 6.8, the beam wander becomes more severe as the beams propagate further down the path, through atmospheric turbulence. Figure 6.9 illustrates this and supports these points from a different perspective, it plots the y-axis centroid positions of the beams, where the initial centroid position in this case is at the 512-pixel position.

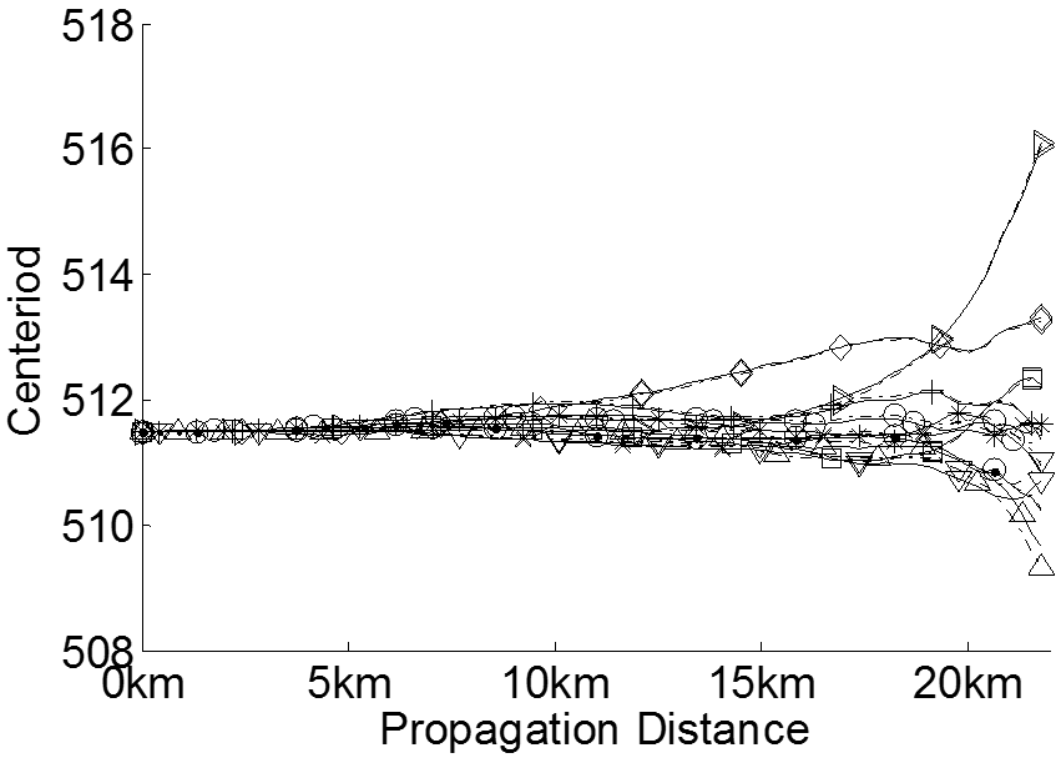

Figure 6.9: Centroid position versus Height.
—— Bessel Beam. - - - Gaussian Beam
The labels are defined in table 6.1 for different aperture radii.

6.2 Beam propagation from Ground to Deep Space (beyond 22 km altitude)

In this section, the aim is to further propagate the beams from ground beyond the 22 km altitude where the atmospheric turbulence terminates, up to a deep space altitude of 100 km. Beyond the 22 km, we have proven in section 4.3.1 that the effect of the atmospheric turbulence is negligible, hence propagation is done *in vacuo* in this region as pictured in figure 6.10 below. Again, Fresnel diffraction is deployed to simulate the propagation of the beams. It should be noted that in this section, we are propagating the Gaussian and Bessel beams that have been distorted by atmospheric turbulence up to the 22 km altitude. Hence, we further propagate them in vacuo to investigate their performance, with a range of beam sizes, based on the Captured power and Intensity error.

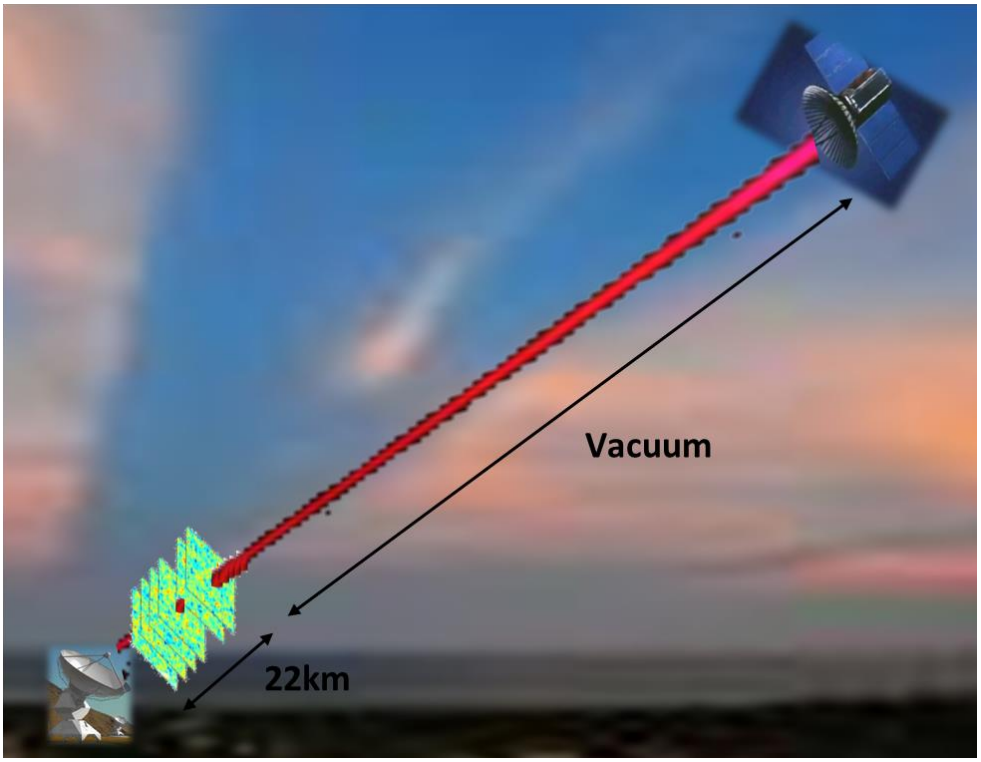

Figure 6.10: Deep Space FSO Communication

6.2.1 Captured Power

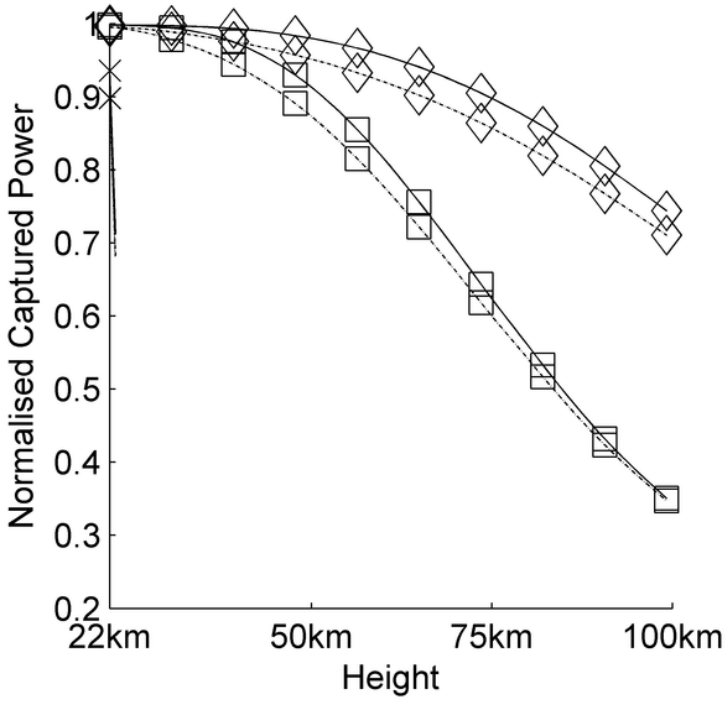

Figure 6.11: Captured Power versus Height. (Beyond the turbulence limit)
—— Bessel Beam. ····· Gaussian Beam.
The labels are defined in table 6.1 for different aperture radii.

Figure 6.11 shows the amount of power captured by a receiver whose radius is same as the ground level-transmitter radius. It is more or less, a further propagation of the beams in figure 6.2, from the 22 km limit, with no atmospheric turbulence, up to 100 km height. Here, both the Gaussian and Bessel beams have the same amount of initial power at the transmitters. The Figure 6.2 is repeated in figure 6.12 below for easy reference and comparison. Comparing figure 6.11 with 6.12, it can be seen that the lower beam sizes for both Gaussian and Bessel beams do not survive up to very high altitudes before losing more than half of their initial power, or before their propagation has to be halted due to having severe power loss. This is in line with table 6.1 that deep space beam propagation will require larger beam sizes to ensure that not more than half of the initial beam power is lost during propagation. Hence, only the beam size labels

for □ GPS satellite and ◊ GEO satellite are able to propagate beyond the 22 km height.

Figure 6.11 also shows that beyond the turbulence limit, the beams still get diffracted as they propagate, hence the captured power still gradually diminishes with height. The Bessel beam still maintains the advantage of having more of its initial beam power successfully captured by the receiver, compared to the Gaussian beam. Because of the absence of atmospheric turbulence in this region, the captured power declines at a slower rate than it does in the atmospheric turbulence region (below the 22 km).

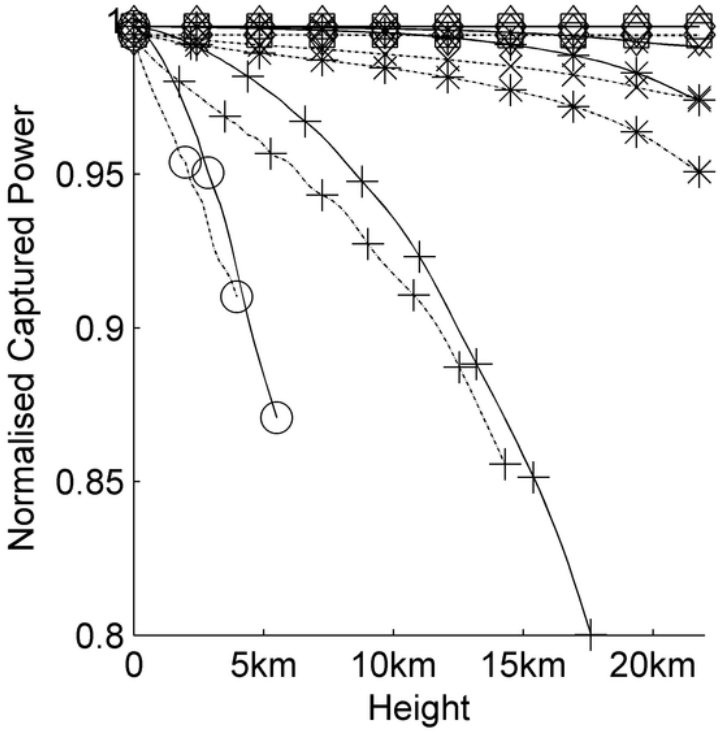

Figure 6.12: Captured Power versus Height. (Within the turbulence limit)
—— Bessel Beam. ····· Gaussian Beam.
The labels are defined in table 6.1 for different aperture radii.

6.2.2 Intensity Error

The intensity error performance of the both beams beyond the atmosphere is going to be similar to the one shown in figure 5.2 when the beams were propagated without turbulence: the Bessel beam has better Intensity error performance than the Gaussian beam. This is contrary to the case in the turbulence region from ground level to 22 km height, where the Gaussian beam had a better intensity error performance as shown in figure 6.7. Recall that we had established in section 6.1.3 that the reason the Gaussian beam had a better Intensity error performance than the Bessel beam, when propagating through atmospheric turbulence, was the Gaussian beam energy is more spread out hence will be less prone to be turbulence-induced errors, compared to the Bessel beam central core whose energy is more concentrated.

However, in this case where the beams have gone beyond the turbulence and now propagating in the absence of the turbulence, there will be no more phase errors on the beams. Hence, the more energy-concentrating Bessel beam now has a better Intensity error performance than the more spread-out Gaussian beam. Another reason the Bessel beam will eventually have a better Intensity error performance in this region is its self-healing property. This property enables it to eventually recover its inward diffraction attribute, after being distorted by atmospheric turbulence and the due to the inward diffraction, its on-axis intensity remains almost invariant as it propagates in this no-turbulence region. The Gaussian beam, on the other hand, does not possess this self-healing attribute and continues to diffract as it propagates in this region. This implies that the Bessel beam, though initially slightly under-performing in the turbulence region, eventually has better Intensity error than the Gaussian beam when propagated beyond the turbulence limit to deep space platforms.

6.3 Chapter Summary

This chapter investigated the propagation of the Gaussian and Bessel beams vertically upwards to high space orbits of 22 km altitude and beyond, up to 100 km. With the transmitter at ground level, we first considered the propagation of the beams up to the atmospheric turbulent limit of 22 km. Here, we analysed the performances of the two beams compared them to each other based on the defined performance criteria. We saw that the Bessel beam majorly outperformed the Gaussian based on the Captured power and Peak intensity while the Gaussian beam had better performance based on Intensity error. The both beams had a similar Beam wander performance since they are propagating through the same atmosphere. The second section of the chapter considered the ground to Deep Space scenario, where the beams are further propagated beyond the 22 km turbulence limit *in vacuo*. With no atmospheric turbulence, the beams were only subjected to diffraction showing that their performances decayed at a slower rate with distance. The Bessel beam had most of the advantage compared to the Gaussian beam as it had better Captured power and recovered its inward-diffracting attributes to produce better Intensity error performance.

CHAPTER 7

7.0 CONCLUSION AND RECOMMENDATION

7.1 Conclusion

Free Space Optics (FSO) clearly have huge potential including secure and robust high capacity communication links. The more common Gaussian beam is known to be extremely susceptible to diffraction resulting in the spread of its energy and lowering the amount that reaches the receiver. Since the main impairments to FSO have been identified to be Diffraction and Atmospheric turbulence, the so-called non-diffracting self-healing Bessel beam is an attractive alternative.

We have confirmed that the non-diffracting attribute of the Bessel beam is only for the ideal case where the beam will have to possess an infinite radius. But to produce the beam in reality, the beam will have to be approximated with the radius truncated into an aperture function and this will limit the range over which the Bessel beam remains non-diffracting to Z_{max}.

Furthermore, we have shown that the longer the distance of the FSO communication, the bigger the size of the transmitter and receiver apertures required to minimise power losses. This applies for both Gaussian and Bessel beams. This solution will be costly and bring an additional inconvenience of size and weight of the transmitter and receiver. To ensure that at least half of the initial power of the beam is delivered to the receiver, the Bessel beam will have a smaller transmitter and receiver aperture size requirements compared to the Gaussian beam, if both beams had an equal initial power before propagation.

When both beams were propagated through atmospheric turbulence, we were able to compare the effect of fixed turbulence in a horizontal 2 km path to that of a gradually-weakening turbulence in a vertically-upwards 2 km path. In the horizontal path scenario, both the transmitter and receiver are at the same altitude, and 2 km apart while the vertically-upwards scenario assumed that the transmitter was at sea level while the receiver was at 2 km altitude. We have seen that beams propagated in the vertically-upwards scenario are less aberrated because the turbulence in this case is gradually weakening with height, compared to the horizontal path fixed turbulence case where the turbulence keeps building up. From this, it is clear that in the design of an FSO system, it is more effective to ensure a substantial altitude difference between the transmitter and receiver to minimise the effect of atmospheric turbulence. For instance, the transmitter could be on the ground level while the receiver is positioned at the top of a sky-scrapper or a high mountain.

For the ground – to – space atmospheric turbulence scenario, we have arrived at a maximum altitude of 22 km above which atmospheric turbulence will be negligible. This 22 km altitude was obtained from an approximate model we derived from a variant of the Hufnagel-Andrews-Philips model of C_n^2 with respect to height, with a few more assumptions. Above this 22 km altitude, it is therefore assumed that the beams would be propagating in a vacuum. Hence, we propagated both the Bessel and Gaussian beam through a ground –to – space turbulence terminating at the 22 km. Then we investigated the performance of the two beams using four categories of performance measure namely: Beam wander, captured power, Intensity error and Peak intensity. The Bessel beam proved to have better performance based on the captured power and peak intensity. The

beam wander effect on both beams appeared to be identical. The Gaussian beam, on the other hand, slightly outperformed the Bessel beam based on the RMS Intensity error.

Beyond the 22 km turbulence limit, both beams were propagated *in vacuo*. As expected, both beams still diffract as they propagate *in vacuo*. The Bessel beam still maintains a better Captured-power performance compared to the Gaussian as it has more of its initial power captured at the receiver at a height of 100 km. Only large beam sizes are able to travel that far without more than half their initial beam lost in transit. Because of the absence of atmospheric turbulence in this region, the captured power declines at a slower rate than it does in the turbulence region. Unlike the turbulence region, the Bessel beam now demonstrates a better Intensity-error performance than the Gaussian as it possesses inward diffraction properties will aid its peak intensity to be almost invariant as it propagates. This indicates that the Bessel beam, though initially slightly under-performing in turbulence, eventually has better Intensity error than the Gaussian beam when propagated beyond the turbulence limit to deep space platforms.

In order to ensure that the advantages that the Bessel beam has over the Gaussian are sustained, the Bessel beam needs to be produced from high efficiency lasers. This could be challenging in reality, especially if the produced beam has to travel for a long distance. Another condition, to ensure that the Bessel beam retains its advantage is that it has to be produced with no side-lobes (rings); this implies that the radial frequency should be chosen such that the beam aperture is equal to the first root of the Bessel function. As shown in this research, the ring-less Bessel beams travels for a considerable distance through turbulence also ensuring efficient power delivery to the receiver, and especially since the turbulence distorts the ring structure of the beam as it

propagates. However, many lasers available in the market inherently produce beams with a near-Gaussian profile. Due to being more readily available, the Gaussian beam could be more frequently utilised and compensated for its poor power delivery performance by having higher transmitted beam power.

Finally, it is widely proposed that earth stations for Ground –to-Space communications be located on mountain tops. Clearly, situating an earth station on a mountain as high as Kilimanjaro for instance, of about 5.8 km height, will ensure that the most of the strong turbulence is avoided as the turbulence weakens with height.

7.2 Future Work

Diffraction and atmospheric turbulence are the most popular impairments to Free Space Optical Communications. These two phenomena and their respective effects on the Gaussian and Bessel beams have been exhaustively covered and analysed in this work. However, there exists another impairment to FSO – Aerosol Scattering. The additional effect of Aerosol Scattering to Free Space Optical Communications would make our model more accurate. Aerosols are tiny solid particles and liquid droplets present in the earth's atmosphere, below the planetary boundary layer. They tend to drift from the stratosphere downwards towards the earth surface. Aerosols vary greatly in size (generally from 0.002 to 100 microns), chemical composition, source, and distribution in time and space. Common examples of aerosols in the atmosphere are smoke, fog, smog, dust and cloud cover. The presence of these aerosols does affect (absorb or scatter) sun light or any other optical signal propagating through the atmosphere. The effect of an aerosol on light depends on:

i. *Colour of the aerosol particle*: Bright coloured/ translucent particles reflect significant amount of light in all directions while dark aerosols can absorb significant amount of lights.

ii. *The constituent of the aerosol*: Pure sulphates as well as nitrates reflect a significant amount of light incident on them. Black carbon, on the other hand, tends to absorb more radiation. Dust particles have varying effects on incident light depending on composition. Salt particles tend to reflect all light they encounter.

iii. *The shape of the aerosol particle*: Atmospheric aerosols are generally spherical but cylindrical particles could be found in viruses and asbestos fibres.

iv. *Size of the aerosol particle*:

This is usually considered with respect to the wavelength of the incident beam.

In Aerosol Optics, the necessary equations for scattered field were derived based on a factor that assumes that the beam size of the incident beam is laterally infinite. This assumption is ideal as an infinite beam size cannot be realistically produced in the laboratory. However, it is a logical assumption since the incident beam will completely drown the aerosol particle as the beam size is very large compared to the size of the aerosol particle. Hence the Scattering and Absorption will be independent of the incident beam size.

There are two main scattering theories widely used to approximate the scattering by a single sphere namely the Mie Scattering and Rayleigh scattering. Rayleigh scattering is known to apply in scenarios where the size of the aerosol particle is much less than the

wavelength of the incident light. For example solar radiations scattered by atmospheric gases. Unlike the Rayleigh scattering, the conditions for applying Mie scattering is somewhat arbitrary based on the size of the particle with respect to the wavelength of the incident light. However, past research has generally defined Mie Scattering as being applied for scenarios where the particle size is comparable or greater than the wavelength of the incident light. Mie Scattering is specific to aerosols and cloud particles which are generally spherical in shape.

For the proposed work of incorporating aerosol scattering into our propagation model, we will be considering atmospheric aerosols which are known to be spherical in shape with size comparable or greater than the incident optical wavelength. Considering the shape and size of the atmospheric particles, the so called Mie's scattering theory is most suitable. However, the Mie's theory only considers scattering by a single particle whereas natural environments like the atmosphere have a collection of particles. Past research on light scattering by a collection of particles mainly focuses on cylindrical particles, not spherical. Hence we seek to model the propagation of Gaussian and Bessel beams through a collection of spherical atmospheric particles present in the lower atmosphere up to the atmospheric boundary layer 1.5 km altitude. The proposed model will investigate the additional effect of aerosol scattering on the two beams.

Expressions will be derived for Amplitude Scattering Matrix for the scattering of optical beams from a collection of arbitrarily-placed spherical atmospheric particles. We will assume a forward scattering situation with no back scattering. Light absorption by the aerosol particles will be neglected while we focus on only scattering from the particles.

APPENDIX A: Related MATLAB Functions

A.1: Gaussian Beam

```
function [E,theta,w0 ] = genGaussianBeam( L,N,BWmask)

%GENGAUSSIANBEAM Produces a Gaussian beam with 99% energy going through
%mask BWmask. L is physical mask size, N number of pixels.

theta=0; %dummy varible

%sig=BW/(2*sqrt(2*log(2)));

L2=linspace(-L/2,L/2,N);

[R ]=radialspace(L2);

w0=BWmask/sqrt(0.5*log(20));

%w0=BWmask/1.5174;

E=exp(-R.^2/w0^2);

%E=1/(2*pi*sig^2)*exp(-R.^2/(2*sig^2));

E=E.*(R<BWmask); %add an aperture

end
```

A.2: Bessel Beam

```
function [ E,theta ] = genBesselBeam( L,N,r0,lambda,n,z,BWmask)

%GENBESSELBEAM genBesselBeam( L,N,r0,lambda,n,z)
%   [ E,theta ] = ggenBesselBeam( L,N,r0,lambda,n,z), L width of array, N number of
%   pixels,r0 bessel beam width, lambda wavelength, n beam order, z
%   distance. Returns 2D amplitude and theta in degrees
k=2*pi/lambda;

kr=2.405/r0;

kz=sqrt(k^2-kr^2);

theta=atand(kr/kz);  %bessel beam cone angle

L2=linspace(-L/2,L/2,N);

[R ,ang]=radialspace(L2);

E=exp(1i*kz*z).*besselj(n,kr.*R).*exp(1i*n*ang); %Bessel beam

E=E.*(R<BWmask); %add an apperture

end
```

A.4: Fresnel Propagation

```
function [ u2, L2] = FresnelPropagation( u1,L,lambda,z, varargin )

%FRESNELPROPAGATION Propergates using Fresenel diffraction
%   [ u2, L2] = FresnelPropagation( u1,L,lambda,z, [method, [options..] ]
%   propagates complex field u1 by distance z. Lambda is the wavelength,
%   L is the width of the array in physical units. Note the array must be
%   square. The function works out which propagation method to use by
%   default. This can be overridden by setting method to 'auto', or a function
handle'propTF',
%   'propIR' or 'propFT'. See those individual help files for details.
%   options are 'nowarn' - suppress warnings, 'verbose' increase verbose output.
%   The function returns u2 the complex field at z, and L2 the x coordinates.
%   Philip Birch 2013 Copyright

warn=1;

verbose=0;

if(length(varargin)>1)
   for p=2:length(varargin)
      switch varargin{p}
         case 'nowarn'
            warn=0;
         case 'verbose'
            verbose=1;
      end
   end
end


[n ,m]=size(u1);
if(n~=m)
   error('PMB:FresnelSq','Input field must be square');
end

N=FresnelNumber(L,lambda,z);
if(N>1 && warn)
   warning('PMB:Fresprop','The Fresnel number, %f, is greater than one. Results maybe
inaccurate',N);
end
dx=L/n;
if dx>=lambda*z/L
   %use TF
   prophandle=@propTF;
else
```

```
   prophandle=@propIR;
end
if N<0.01
   prophandle=@propFF;
end
if(~isempty(varargin))
   switch varargin{1}
      case 'auto'
         %do nothing
      otherwise
         prophandle=str2func(varargin{1});
   end
end
if(verbose)
   fprintf('Using propagation function %s\n',func2str(prophandle));
end
[u2, L2]=prophandle(u1,L,lambda,z);
end
```

A.5: Atmospheric Turbulence

```
function [r0] = calcR0( height,lambda,z )

%CALCR0 Calculates Fried parameter for given height
%   [ r0 ] = calcR0( height ,lambda, z) lambda is wavelength, height is
%   starting height, z the the top height limit of atmosphere slice.
% Philip Birch 2014


k=2*pi/lambda;
Cn2=@(z) 6.5*(3.593*10^(-3).*(z/100000).^(10).*exp(-z/1000)+2.7*10^(-16).*exp(-
z/1500));
%Cn2=@(h) 6.5*(3.593*10^(-3).*(h/100000).^(10).*exp(-h/1000)+2.7*10^(-16).*exp(-
h/1500));% @ () is to make it an anonymous function handle


%r0=(0.43*k^2*Cn2(height)*z).^(-3/5);  %this is not accurate
r0=(0.42*k^2*integral(Cn2,height,z)).^(-3/5);   %integral
%fprintf('Cn2=%f m^-2/3\n',Cn2);
%use quad in old versions of matlab
end
```

A.6: Phase Screens

```
function [phz_lo phz_hi] = ft_sh_phase_screen(r0, N, delta, Lout, Lin)
D = N*delta;
phz_hi = ft_phase_screen(r0, N, delta, Lout, Lin);
[x y] = meshgrid((-N/2:N/2 -1)*delta);
phz_lo = zeros(size(phz_hi));
for p = 1:3
   del_f = 1 / (3^p*D); %frequency grid spacing [1/m]
   fx = (-1 : 1) * del_f;
   [fx, fy] = meshgrid(fx);
   [~, f] = cart2pol(fx, fy); % polar grid
   fm = 5.92/Lin/(2*pi); % inner scale frequency [1/m]
   f0 = 1/Lout; % outer scale frequency [1/m]
   % modified von Karman atmospheric phase PSD
   PSD_phi = 0.023*r0^(-5/3) * exp(-(f/fm).^2)./(f.^2 + f0^2).^(11/6);
   PSD_phi(2,2) = 0;
   % random draws of Fourier coefficients
   cn = (randn(3) + 1i*randn(3)).* sqrt(PSD_phi)*del_f;
   SH = zeros(N);
   % loop over frequencies on this grid
   for ii = 1:9
   SH = SH + cn(ii) * exp(1i*2*pi*(fx(ii)*x+fy(ii)*y));
   end
   phz_lo = phz_lo + SH;
end
phz_lo = real(phz_lo) - mean(real(phz_lo(:)));

function phz = ft_phase_screen(r0, N, delta, Lout, Lin)
 % setup the PSD
 del_f = 1/(N*delta); % frequency grid spacing [1/m]
 fx = (-N/2 : N/2-1) * del_f;
 % frequency grid [1/m]
 [fx, fy] = meshgrid(fx);
 [th, f] = cart2pol(fx, fy); % polar grid
 fm = 5.92/Lin/(2*pi); % inner scale frequency [1/m]
 f0 = 1/Lout; % outer scale frequency [1/m]
 % modified von Karman atmospheric phase PSD
 PSD_phi = 0.023*r0^(-5/3) * exp(-(f/fm).^2)./ (f.^2 + f0^2).^(11/6);
 PSD_phi(N/2+1,N/2+1) = 0;
 % random draws of Fourier coefficients
 cn = (randn(N) + 1i*randn(N)) .* sqrt(PSD_phi)*del_f;
 % synthesize the phase screen
 phz = real(ift2(cn,1));
```

```
end
function g = ift2(G, delta_f)
  % function g = ift2(G, delta_f)+.

  N = size(G, 1);
  g = ifftshift(ifft2(ifftshift(G))) * (N * delta_f)^2;
end
```

APPENDIX B: Simulation Errors

Recall that oversampling is the desirable situation that ensures that the chirp function in the Fresnel Transfer Function (IR) and Impulse Response (IR) propagators are adequately sampled. When the appropriate Fresnel propagator are not chosen for the respective regime criteria in table B.1 below, it results in undersampling of the chirp function in the Fresnel propagators. This produces simulation errors and we demonstrate some of them in this section.

Table B.1: Sampling regimes

Regime	**Chirp Sampling**
$\Delta x < \frac{\lambda z}{L}$	*IR* is oversampled *TF* is undersampled (artifacts)
$\Delta x > \frac{\lambda z}{L}$	*IR* is undersampled (periodic copies). *TF* is oversampled
$\Delta x = \frac{\lambda z}{L}$	Critical sampling for both *IR* and *TF*

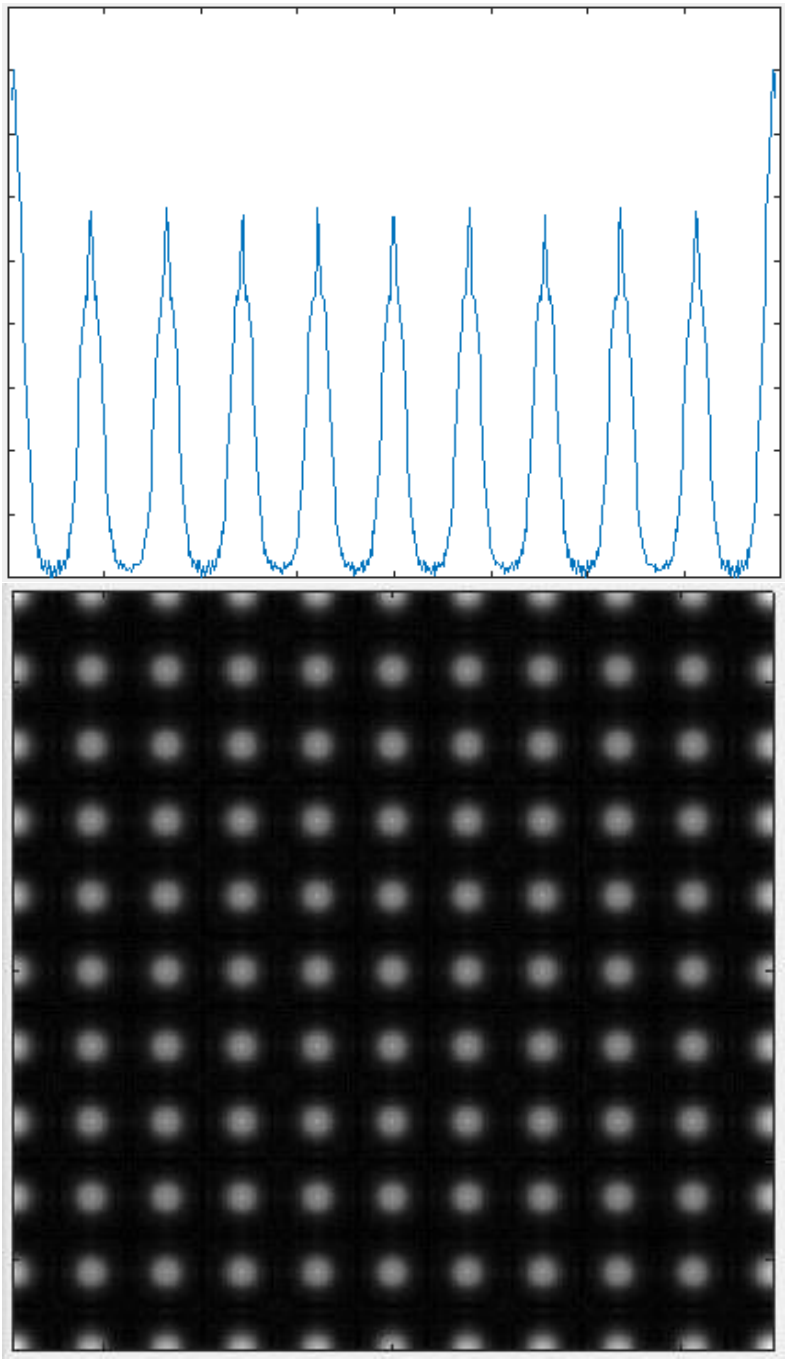

Figure B.1: Undersampled Fresnel IR.

When the Fresnel IR propagator is erroneously used for the a scenario where the $\Delta x > \frac{\lambda z}{L}$, it results in undersampling as seen in table B.1. As seen in the figure B.1 above, this results in periodic copies of the field at the observation plane, for a propagated Gaussian beam.

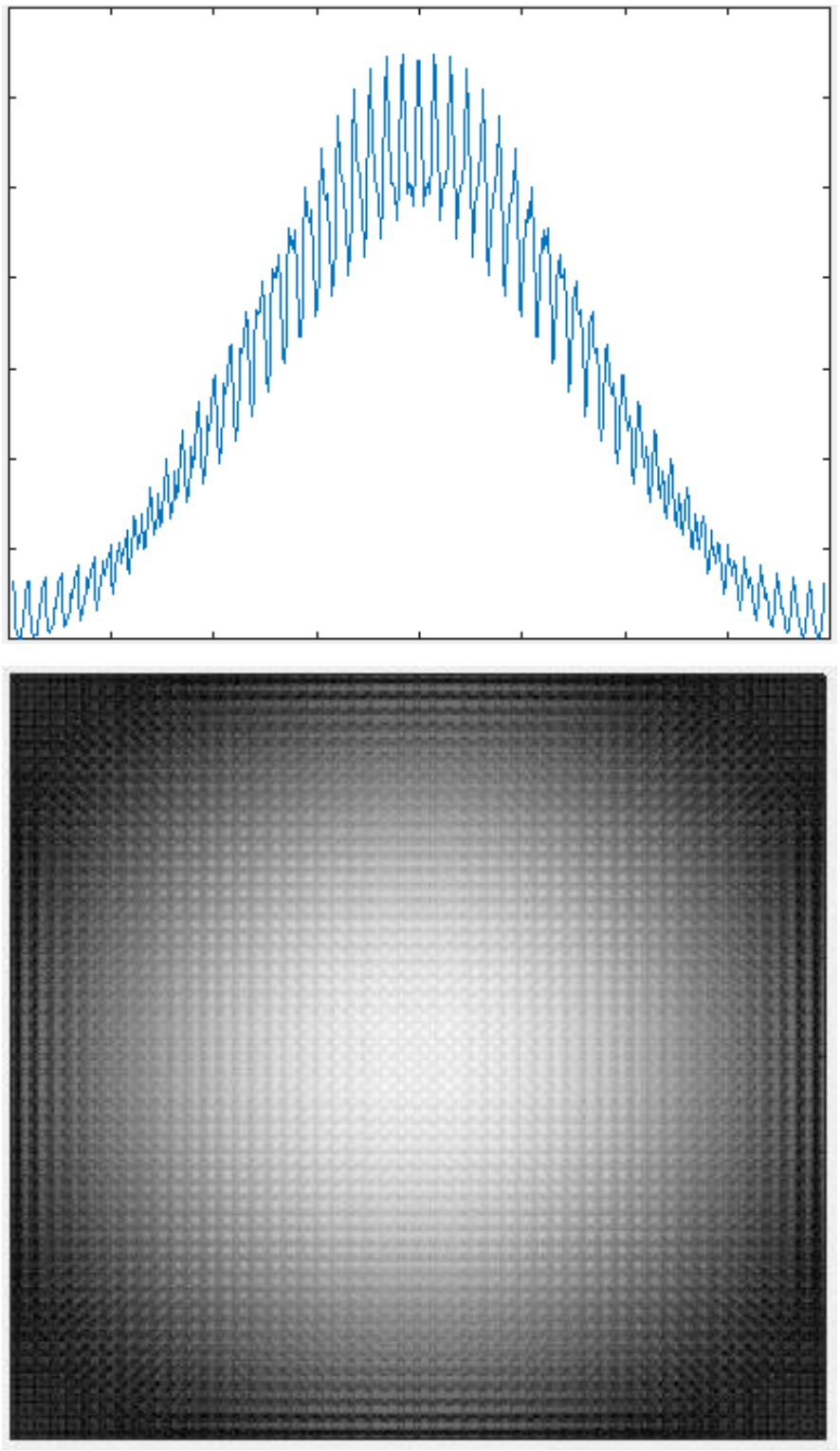

Figure B.2: Undersampled Fresnel TF

For a propagated Gaussian beam, the error in figure B.2 occurred when the Fresnel TF propagator was wrongly used in a $\Delta x < \frac{\lambda z}{L}$ regime. This produces artifacts as seen in the figure B.2 above.

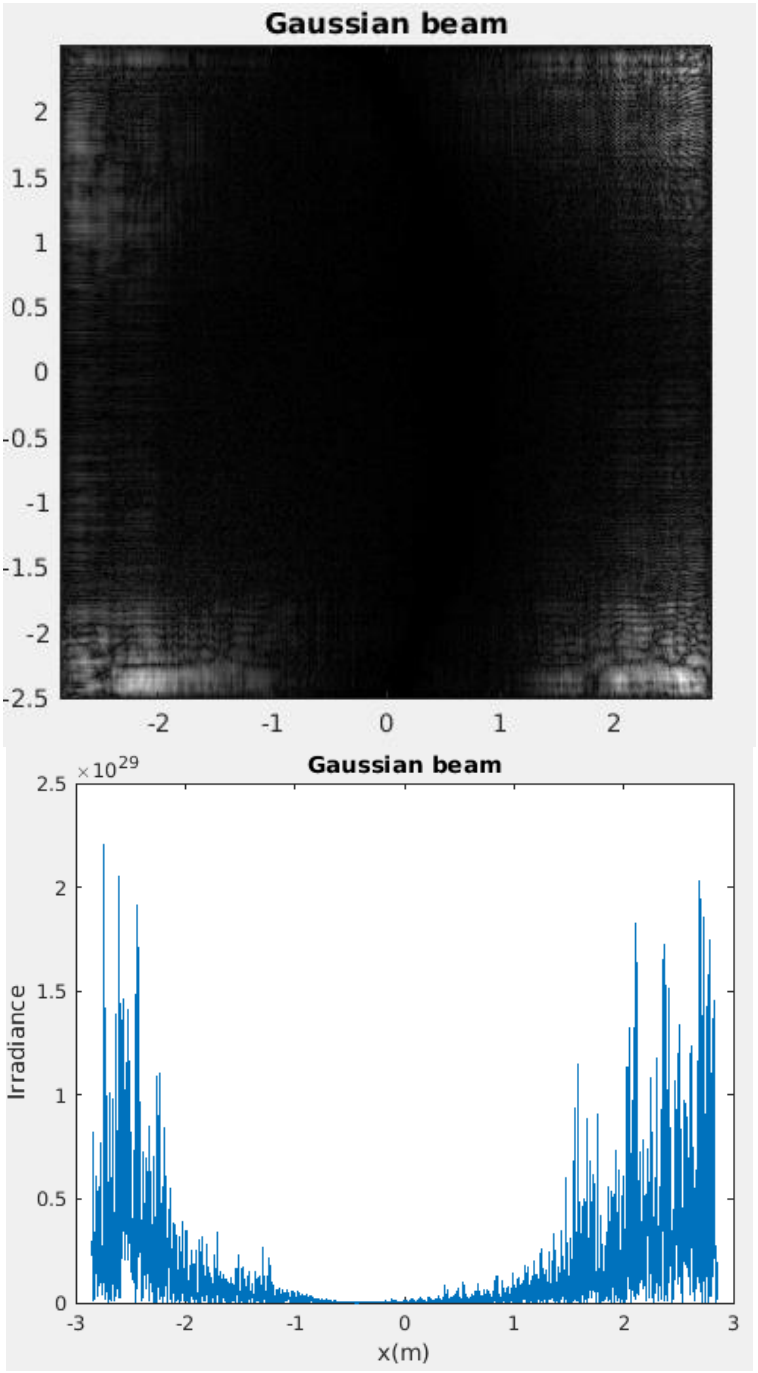

Figure B.3: Artifacts at the edge of the array

If the beam is not limited to a guard area or aperture with diameter $D \ll$ the source grid length L, it results in artifacts at the edge of the observation grid array due to periodic extension properties of FFT.

REFERENCES

1. Stamatious V. Kartalopoulos, *Free Space Optical Networks for Ultra-Broad Band Services,* 1st ed., IEEE, John Wiley & Sons, Inc. (2011), pp 1 – 10.
2. Deva K. Borah *et al*, "A Review of communication-oriented Optical Wireless Systems." *EURASIP Journal on Wireless Communications and Networking* (2012).
3. B. A. Witvliet *et al, Comparison of UHF Measurement with the propagation model of Recommendation ITU-R P.156,* Radiocommunications Agency Netherlands, 2010. pg. 13.
4. Stamatious V. Kartalopoulos, *Free Space Optical Networks for Ultra-Broad Band Services,* 1st ed., IEEE, John Wiley & Sons, Inc. (2011), Chapter 1.
5. Suriza Ahmad Zabidi *et al*, "The Effect of Weather on Free Space Optics Communication Under Tropical Weather Conditions and a Proposed Setup for Measurement." *ICCCE* (2010).
6. M. S. Awan *et al*. "Transmission of High Data Rate Optical Signals in Fog and Snow Conditions." *IEEE Wireless VITAE* (2009).
7. P.W. Kruse , L. McGlauchlin, and O.H. Vaughan , *Elements of Infrared Technology: Generation, Transmission and Detection*, John Wiley & Sons, New York (1962).
8. E. Leitgeb et al. "The Influence of Dense Fog on Optical Wireless Systems, analysed by Measurements in Graz for Improving the Link-Reliability." *ICTON* (2006).
9. J. Durnin, "Exact solutions for nondiffracting beams. I. The Scalar theory," J. *Opt. Soc. Am. A*, **4** (1987), pp. 651-654.
10. J. Durnin, J.J. Miceli and J.H. Eberly, *Phys. Rev. Lett*., **66** (1991), pp. 838.
11. D. McGloin and K. Dholakia, "Bessel beams: Diffraction in a new light," *Contemporary Physics*, **46** (2005), pp. 15-28.
12. W. Nelson, J. P. Palastro, C.C. Davis and P. Spangle, "Propagation of Bessel and Airy Beams through Atmospheric Turbulence". *J. Opt. Soc. Am. A*, Vol. 31, No 3, 2014.
13. P. Sprangle and B. Hafizi, "Comment on nondiffractive beams," Phys. Rev. Lett. **66**, 1991, pg. 837.
14. L.C. Andrews, R. Phillips, R. Crabbs, D. Wayne, T. Leclerc, and P. Sauer, "Atmospheric Channel Characterisation for ORCA Testing at NTTR," *Proc. Of SPIE* Vol. **7588** (2010).

15. Sergio Martelluci and Massimo Santarsiero (ed.,), "Free and Guided Optical Beams," *Proc. Int. Sch. Quant. Electronics*, Erice Slcily (2002).
16. Orazio Svelto, *Principles of Lasers,* 5th ed. (Springer London, 2010), pp. 150 – 158.
17. Anthony Siegman, *Lasers* (University Science Books, California, 1986), Chapter 17.
18. Paul F. Goldsmith, *Quasioptical Systems: Gaussian Beam Quasioptical Propagation and Applications* (Wiley-IEEE Press, 1997), Chapter 2.
19. Robert K. Tyson, *Principles of Adaptive Optics* (Academic Press, London, 1991), pp. 1- 23.
20. B. D. Guenther, *Modern Optics*, 1st ed. (Oxford University Press, 1990), pp. 356-364.
21. H. Kogelnik and T. Li, "Laser Beam and Resonator", *Appl. Opt.* **5,** 10, (1966), pp.1550-1567.
22. Stamatious V. Kartalopoulos, *Free Space Optical Networks for Ultra-Broad Band Services*, 1st ed. (IEEE, John Wiley & Sons, 2011), Chapter 1.
23. Rudiger Paschotta, *Encyclopedia of Laser Physics and Technology*, volume **1**, (John Wiley & Sons, 2008).
24. H. Weber, "High Average Power Solid State Lasers for Material Processing and Fiber Transmission," in *Laser Applications for Mechanical Industry*, S. Martelluci *et a*l (ed.), Series E: Applied Sciences, **238**, (Springer Science + Business, Dordrecht, 1993), pg. 13.
25. Amnon Yariv, *Quantum Electronics,* 3rd ed. (John Wiley & Sons, New York, 1989), Chapter 3 and 7.
26. L. Allen *et al*, "Orbital Angular momentum of light and the transformation of Laguerre-Gaussian laser modes", *Phys. Rev.* A **45**, 11 (1992).
27. M. Bandres and J. Gutierrez-Vega, "Ince-Gaussian beams," *Opt. Lett.* **29**, 2 (2004), pp. 144-146.
28. E. Karimi *et al*, "Hypergeometric-Gaussian modes", *Opt. Lett*. **32**, 21 (2007), pp. 3053- 3055.
29. J. Durnin, J.J. Miceli and J.H. Eberly, "Comparison of Bessel and Gaussian beams," *Opt. Lett*., **13** (1988), pp. 79-80.
30. G Indebetouw, "Non-diffracting Optical Fields: some remarks on their Analysis and Synthesis," *J. Opt. Soc. Am. A*., **6**, 1 (1989), pp. 150 – 152.
31. Mohamed Mahmoud *et al*, "Propagation of Bessel beam generated using finite-

width Durnin ring," *Appl. Opt.* **52**, 2 (2013), pp. 256-263.

32. S Fujiwara. "Optical properties of conical surfaces. 1. Reflecting cones," *J. Opt. Soc. Am.*, **52** (1962), pp. 287-292.
33. Angela Dudley *et al*, "Unravelling Bessel Beams," *OSA Optics & Photonics News*, **24**, 6 (2013), pp. 22-29.
34. J. Durnin, J.J. Miceli and J.H. Eberly, "Diffraction-Free Beams," *Phys. Rev. Lett*., **58** (1987), pp. 1499-1501.
35. C. A. McQueen, J. Arlt and K. Dholakia, "An experiment to study 'nondiffracting' light beam," *Am. J. Phys*., **67** (1999), pp. 912-915.
36. Islam Abdo *et al*, "Effects of ring width on ring generated Bessel beam," *Proc SPIE*, **8236** (2012).
37. N. Chattrapiban *et al*, "Generation of non-diffracting beams by use of Spatial Light Modulator," *Opt. Lett*., **28** (2003), pp. 2183-2185.
38. J. Turunen, A. Vasara and A. Friberg, "Holographic generation of diffraction-free Beams," *Appl. Opt.* **27**, 19 (1988), pp. 3959 – 3962.
39. A. Vasara, J. Turunen, and A. Friberg, "Realization of general nondiffracting beams with computer-generated holographs," *J. Opt. Soc. Am. A*., **6**, 11 (1989), pp. 1748 – 1754.
40. C. Paterson and R. Smith, "Higher-order Bessel waves produced by Axicon-type Computer-generated holograms," *Optical Communications* **124** (1996), pp. 599-602
41. S. H. Tao, X. C. Yuan and B. Ahluwalia, "The generation of an array of nondiffracting beams by a single composite computer generated hologram," *J. of Optics A: Pure and Applied Optics*, **7** (2005), pp. 40-46.
42. E. M. Epperlein (*ed*.,), "Experimental Investigation of Bessel-Beam Characteristics," *LLE Review*, **46** (January-March 1991), Section 2A.
43. S. Chavez-Cerda *et al*, "Holographic generation and Orbital angular momentum of Higher-order Mathieu beams," *J. Opt. B: Quantum Semiclass. Opt*., **4** (2002), S52-S57.
44. Robert Nowack, "A tale of two beams: An elementary Overview of Gaussian beams and Bessel Beams", *Stud. Geophys. Geod*., **56** (2012), pp. 355 – 372.
45. Jason D. Schmidt, *Numerical Simulation of Optical Wave Propagation, with examples in MATLAB*, SPIE Press Bellingham, Chapter 1.
46. J Jackson, *Classical Electrodynamics*, 3rd ed., John Wiley and Sons Inc., (1998).

47. Andrew Zangwill, *Modern Electrodynamics,* Cambridge University Press (2013), pp. 44-45.
48. J. W. Goodman, *Introduction to Fourier Optics*, 2nd Ed., McGraw-Hill Companies Inc, 1996.
49. R. Bracewell, *Two Dimensional Imaging*, Prentice-Hall, New Jersey (1994).
50. David Voelz, "*Computational Fourier Optics, a Matlab tutorial*," SPIE Press, Bellingham (2011), pp. 1-27.
51. E. Brigham, *The Fast Fourier Transform and its Applications*, Prentice-Hall, New Jersey (1988).
52. David Voelz, "*Computational Fourier Optics, a Matlab tutorial*," SPIE Press, Bellingham (2011), pp. 47-86.
53. A Sommerfeld, *Optics*, vol. IV, of *Lectures on Theoretical Physics*, Academic Press, New York (1954).
54. Francesco Grimaldi, Bologna, Italy: Vittorio Bonati (1665), pp. 1-11. (In Latin).
55. Eugene Hecht, *Optics*, 3rd ed., Addison Wesley Longman Inc. (1998), Chapter 10.
56. Christiaan Huygens, *Treatise on Light*, Dover Publication, New York (1962).
57. Augustin Fresnel, " Memoir on the Diffraction of Light", in *The Wave Theory of Light-Memoirs by Huygens, Young and Fresnel*, American Book Company (1819), pp. 79-145.
58. Gustav Kirchhoff, "Zur Theorie der Lichtstrahlen", *Weidemann Ann*., **2**, 28 (1883), pg. 663.
59. Jason D. Schmidt, *Numerical Simulation of Optical Wave Propagation, with examples in MATLAB*, SPIE Press Bellingham, Chapter 6.
60. W. Coles, J. Filice, R. Frehlich, and M. Yadlowsky, "Simulation of Wave propagation in three-dimensional random media," *Appl. Opt*. **34**, 12 (1995), pp. 2089-2101.
61. N. Delen and B. Hooker, "Verification and comparison of a fast Fourier transform-based full diffraction method for tilted and offset planes," *Appl. Opt*. **40**, 21 (2001), pp. 3525-3531.
62. S. Coy, "Choosing Mesh spacing and mesh dimensions for wave optics simulation," *Proc. SPIE* **5894** (2005).
63. J. Mansell, R. Praus and S. Coy, "Determining Wave-Optics mesh parameters for complex Optical systems," *Proc SPIE* **6675** (2007).

64. L. Onural, “Some mathematical properties of the uniformly sampled Quadratic phase Function and associated issues in Digital Fresnel Diffraction simulations,” *Opt. Eng*. **43**, 11 (2004), pp. 2557-2563.
65. P. Roberts, “A Wave Optics propagation code,” *Tech. Rep. TR-760*, the Optical Sciences Company (1986).
66. G. A. Tyler and D. L. Fried, “A wave optics propagation Algorithm,” *Tech. Rep. TR-451*, the Optical Sciences Company (1982).
67. D. Voelz and M Roggemann, “Digital simulation of Scalar Optical diffraction: revisiting Chirp function Sampling criteria and Consequences,” *Appl. Opt*. **48**, 32 (2009), pp. 6132 – 6142.
68. C. Rydberg and J. Bengtsson, “Efficient Numerical representation of the Optical field for the propagation of partially coherent radiation with a specified spatial and temporal Coherent function,” *J. Opt. Soc. Am. A*. **23**, 7 (2006), pp. 1616-1625."
69. Jason D. Schmidt, *Numerical Simulation of Optical Wave Propagation, with examples in MATLAB*, SPIE Press Bellingham, Chapter 7.
70. David Voelz, “*Computational Fourier Optics, a Matlab tutorial*,” SPIE Press, Bellingham (2011), pp. 191-198.
71. Jason D. Schmidt, *Numerical Simulation of Optical Wave Propagation, with examples in MATLAB*, SPIE Press Bellingham, Chapter 9.
72. Robert K. Tyson, *Principles of Adaptive Optics*, Academic Press Limited San Diego (1991), pp. 25 – 50.
73. A. N. Kolmogorov, “The local structure of turbulence in an incompressible viscous Fluids for very large Reynolds numbers,” *C. R. (Doki) Acad. Sci. U.S.S.R.* **30** (1941), pp.301-305.
74. Javier Jimenez, “The Contributions of A. N. Kolmogorov to the Theory of Turbulence”, *Arbor Magazine CLXXVIII*, **704**, Agosto (2004), pp 589-606.
75. A. D. Wheelon, *Electromagnetic Scintillation: Volume 2, Weak Scattering*, Cambridge University Press (2003).
76. G. K Batchelor, *The Theory of Homogeneous Turbulence*, Cambridge University Press, London (1953).
77. A. Kolmogorov, in *Turbulence; Classic Papers on Statistical Theory*, S. K. Friedlander and L.Topper, eds., Interscience Publishers (1961), pp. 151 -157.
78. Stanley Corrsin, *Journal of Applied Physics*, Volume **22** (1951), pp. 469 – 473.

79. V. I. Tartaskii, *Wave Propagation in a Turbulent Medium*, Translated by R. A. Silverman McGraw Hill, New York (1961).
80. J. W. Strohbehn, ed., *Laser Beam Propagation in the Atmosphere*, Springer-Verlag, New York (1978), pp. 9 - 43.
81. V. I. Tartaskii, *The Effect of the Turbulent Atmosphere on Wave Propagation*, U. S. Dept. of Commerce, National Information Technical Service, Springfield VA (1971).
82. V. Tatarskii, Wave Propagation in a turbulent medium, McGraw Hill, New York (1961).
83. L.C. Andrews and R. L. Philips, *Laser Beam Propagation Through Random Media*, 2nd ed., SPIE Press, Bellingham, WA (2005).
84. Arnold Tunick et al, "Characterisation of optical Turbulence (Cn2) data measured at ARLA_LOT facility," ARL-MR-625, *US Army Research Laboratory*, Adelphi, MD 20783-1145 (2005).
85. E. A. Murphy, E.M. Dewan, and S.M Sheldon, "Daytime comparisons of Cn2 models to measurements in a desert location". *SPIE*, **551**(1985), pp. 156-162.
86. R. R. Beland, "Propagation through atmospheric optical turbulence," in *the Infrared and ElectroOptical Systems Handbook*, F. G. Smith, ed., vol. 2, SPIE Opt. Eng. Press, Bellingham (1993), Chapter 2.
87. A. Belmonte, "Feasibility Study for the simulation of beam propagation: Consideration of coherent Lidar performance," *Appl. Opt*., **39** (2000), pp. 5426-5445.
88. R. E. Hufnagel, "Propagation through Atmospheric Turbulence," *Proc. Topical Mtg. on Optics*, Boulder, CO (1974).
89. G. C. Valley, "Isoplanatic Degradation of tilt correction and short-term Imaging Systems," *Appl. Opt*. **19** (1980), pp. 574-577.
90. P. B. Ulrich. "Hufnagel-Valley Profiles for specified values of the coherence length and Isoplanatic Patch Angle," W. J. Schafer Associates, WJSA/MA/TN-88-013 (1988).
91. D. L. Walters and K. E. Kunkel, "Atmospheric modulation transfer function for desert and mountain locations: the atmospheric effect on r0," *J. Opt. Soc. Am*., **71** (1981), 397- 405.
92. L.C. Andrews, R. Phillips, D. Wayne, T. Leclerc, and P. Sauer, R. Crabbs, and J.

Kiriazes, “Near ground vertical profile of refractive-index fluctuations,” *Proc. SPIE*, **7324** (2009).

93. S. Y. Shao, X. B. Li, Y. J. Li, W. Y. Zhu, D. Y. Kang, C. Y. Fan, and N. Q. Weng, “Daily variation Analysis of Atmospheric Turbulence from Inland to Open sea,” *J. of Phys.:Conf. Series* **679** (2016).
94. Yu P. Soloviev, “ Measurement of the atmospheric turbulence in the coastal zone of the sea during weak wind from a mountainous coast,” *Izvestiya, Atmospheric and oceanic Physics* **49**, 3 (2013), pp. 315-328.
95. Siri Jodha Singh Khalsa, Gary Greenhut, “Atmospheric turbulence structure in the vicinity of an oceanic front,” *J. of Geophysical Research* **94**, C4 (1989), pp. 4913-4922.
96. D. L. Fried, “Statistics of a Geometric Representation of Wavefront Distortion,” *J. Opt. Soc. Am.* **55,** 11 (1965), pp. 1427-1431.
97. S. M. Rytov, *Izvestiya Akad. Nauk SSSR (Ser. Fiz.)* **2**, 223 (1937).
98. L. C. Andrews, R. L. Philips, C. Y. Hopen, *Laser Beam Scintillation with Applications*, SPIE Press, Bellingham (2001), Chapter 2.
99. N. Perlot, “Characterisation of signal fluctuations in optical communication with intensity modulation and direct detection through the turbulent atmospheric channel,” Aachen: Shaker Verlag, 2006.
100. S. F. Clifford, Chapter 2 of Strohbehn, *op. cit.*
101. M. A. Vorontsov, G.W. Carhart, V. Gudimetla, T. Veyrauch, E. Stevenson, S. Lachinova, L. Beresnev, J. Liu, K. Rehder, and J. Riker, “Characterization of atmospheric turbulence effects over 149 km propagation path using multi-wavelength laser beacons,” *AMOS Conf. Proc., Hawaii* (2010), pp. E18.
102. W. Miller, J. Ricklin, and L. C. Andrews, “Effects of refractive index spectral model on irradiance variance of a Gaussian beam,” *J. Opt. Soc. Am. A.*, **12** (1995), pp. 2719-2726.
103. L. C. Andrews, R. L. Philips, and C.Y. Hopen, “Aperture averaging of optical scintillations: power fluctuations and the temporal spectrum,” *Waves in Random Media* **10** (2000), pp.53-70.
104. A Prokes, “Modelling of Atmospheric turbulence effect on terrestrial FSO link,” *Radioengineering*, **18**, 1 (2009), pp. 42-47.
105. R. J. Scaddan, J. C. Dainty, “A simple method of estimating the RMS Phase

Variation due to Atmospheric Turbulence," *Optical Communications* **21**, 1 (1977), pp. 51-54.

106. S. F. Clifford, G. M. B. Bouricius, G. R. Ochs, and M. H. Ackley, "Phase variations in Atmospheric Optical Propagation," *J. Opt Soc. Am*. **61**, 10 (1971), pp. 1279-1284.
107. A. Kon and V. Tatarskii, *Izv. VUZ, Radiofiz*. **8**, 870 (1965).
108. R. F. Lutomirski, H. T. Yura, *Applied Optics*, **10**, pg. 1652, 1971.
109. T. A. Rhoadarmer and R. P. Angel, "Low-cost, broadband static phase plate for generating atmospheric-like turbulence," Appl. Opt. 50, (2001), pp. 2946-2955.
110. S.V. Mantravadi, T. A. Rhoadarmer, and R. S. Glas, "Simple laboratory system for generating well-controlled atmospheric-like turbulence," *Proc. SPIE* **5553** (2004).
111. L. C. Andrews, R. L. Philips, and A. R. Weeks, "Propagation of a Gaussian-beam wave through a random phase screen," *Waves in Random Media* **7** (1997), pp. 229-244.
112. T.-C. Poon and T. Kim, *Engineering Optics with Matlab*, World Scientific Publishing Co. (2006), pp 121-133.
113. V. P. Lukin and B. V. Fortes. *Adaptive Beaming and Imaging in the Turbulent Atmosphere*, SPIE Press, Bellingham, WA (2002).
114. N. Roddier, "Atmospheric wavefront simulation using Zernike polynomials," *Opt. Eng.* **29**, 10 (1990), pp. 1174-1180.
115. K. A. Winick, "Atmospheric Turbulence-induced signal fades on optical heterodyne communication links," *Appl. Opt.* **25**, 11 (1986), pp. 1817-1825.
116. B. L. McGlamery, "Computer Simulation Studies of Compensation of Turbulence Degraded Images," *Proc. SPIE* **74** (1976), pp 225-233.
117. R G Lane, A. Glindemann, and J.C. Dainty, "Simulation of a Kolmogorov phase Screen," *Waves in Random Media* **2** (1992), pp. 209-224.
118. B. J. Herman and L. A. Strugala, "Method for inclusion of low frequency contributions in Numerical Representation of Atmospheric turbulence," *Proc. SPIE* **1221**(1990), pp.183- 192.
119. Rod Frehlich, "Simulation of Laser Propagation in a Turbulent Atmosphere," *Appl. Opt*. **39**, 3 (2000), pp. 393-397.
120. B. M. Welsh, "A Fourier series based atmospheric phase screen generator for simulating anisoplanatic geometries and temporal evolution," *Proc. SPIE* **3125**

(1997) pp. 327-338.

121. F. D. Tappert and R. H. Hardin, *Eight Int. Cong. Acoustics*, London (1974), pg. 452.